UNIVERSITÀ DEGLI STUDI DI TRIESTE

XXXI CICLO DEL DOTTORATO DI RICERCA IN FISICA

GRAPHENE-BASED INTERFACES AS TUNEABLE SUPPORT FOR METAL OXIDE NANOPARTICLES

Settore scientifico-disciplinare: FIS/03

DOTTORANDO
DARIO DE ANGELIS

COORDINATORE
PROF. LIVIO LANCERI

SUPERVISORE DI TESI
PROF. ALESSANDRO BARALDI

ANNO ACCADEMICO 2017/2018

UNIVERSITY OF TRIESTE

Department of Physics

Graduate School in Physics, Cycle XXXI

PhD Thesis

Graphene-based interfaces as tuneable support for metal oxide nanoparticles

Supervisor:
Prof. Alessandro Baraldi

Candidate:
Dario De Angelis

Academic Year 2017-2018

Abstract

In my PhD activity I was involved in the study of graphene-supported metal oxide nanoparticles and the effect of the graphene doping on their electronic and chemical properties. Nanostructured materials are nowadays at the centre of the scientific investigation in the condensed matter field. The fundamental concept that drives this research topic is that the microscopic features of a nano-designed material can affect its macroscopic properties. This is the reason why, often, the experimental results lead to applications in many different contexts as for example in chemistry, quantum optics, in the field of energy storage, biosensing or quantum optics, rapidly paving the way towards the developments of new technologies. Nano-architectured materials are strictly related to low dimensionality materials. The term nano, in fact, refers to a length scale at which quantum confinements begins to be non-negligible and it gives rise to microscopic modifications and phenomena that have consequences on the macroscopic behaviour of the system. The building blocks of these structures are typically 2D, 1D and 0D objects i.e., namely, layered materials, nanowires and nanoclusters. In this PhD work I investigated the interaction between nanoparticles and their solid substrate with the aim to tune the properties of the first ones by controlling the structure of the latter. To do so, we combined 2D and 0D materials to fabricate novel nanostructured interfaces. Metal oxides nanoparticles have been studied, with an attention on their possible application as heterogeneous photocatalysts. The thesis starts describing the methods used to create differently nanostructured supports for the metal oxide nanoparticles. Graphene has been used as the key building block in this context because of its several remarkable properties. From the electronic point of view, its outstanding transport properties promise to be an efficient way to increase the charge separation in photocatalytic reactions. On the other hand, its mechanical strength and its thermal stability are two features that a substrate must have to be reliably exploited. In order to modify the electronic structure of graphene, intercalation procedures have been performed to grow a metal oxide thin layer between graphene and its original substrate, whose effect can be described as an electronic doping of graphene. The focus of the experimental activity is the investigation of the correlation between the doping state of graphene and the electronic and chemical properties of the supported particles. Three different metal oxides have been used as both particle constituents and intercalant agents to collect information about different possible graphene doping levels and particles modifications: iron, cobalt and

titanium oxide. Synchrotron radiation spectroscopy techniques were used as the principal measurement methods for the characterization of the electronic structure of these interfaces. For titanium oxide, photocatalytic measurements were performed in collaboration with the Department of Chemistry at the University of Trieste, demonstrating that the graphene-based substrate can be designed to enhance the activity of the supported particle-photocatalyst by more than one order of magnitude respect to the same material supported by a metal surface. Theoretical calculations have been also performed to better understand the mechanisms behind this enhancement and possibly predict the behaviour of further nanostructures. In parallel to this research activity I worked on the development and commissioning of a mass-selected nanocluster source, designed to produce clusters with a precise number of atoms in order to exploit space-averaging experimental techniques to investigate their properties. During my PhD period the machine was completed and the first functional tests were performed. Once at regime, this cluster source, associated with the capabilities of a synchrotron facility, will be used to conduct experiments that will shed light on now inaccessible aspects of nanoclusters.

Contents

Chapter 1

Introduction

The goal of my research activity was to explore the possibility to create tailored nanostructured interfaces, whose properties derive from the tuneable interaction between metal oxide nanoparticles and their customized graphene-based supports. To this purpose I have investigated materials with different dimensionality, namely 2D graphene (Gr) and ultra-thin oxides, in combination with 3D nanoparticles.

One of the most fascinating aspects of condensed matter at the nanoscale is that some of its properties are often totally different from the ones shown by the macroscopic counterparts. This peculiarity is what boosted the huge development of many areas of research and technology in the last twenty years.

Nanoparticles (NPs) are the prime example of nano-matter. The term is generally related to particles whose size ranges between 1 and 100 nm, even if a formal definition does not exist. NPs can show a variety of different structures and shapes. The common point is that nanoparticles of a specific material show significant differences with respect to the bulk material on some physical and chemical aspects, such as melting point, thermal and electrical conductivity, catalytic activity, magnetic behaviour, light absorption and scattering.

The history of nanoparticles practical application seems to begin with the growth of 5-60 nm gold particles in a glass matrix, forming the gold-ruby glass of the Lycurgus Cup, which dates from Roman times [1]. This unaware employment of nanoparticles is an example of how their formation is not strictly related to the modern laboratory activity, but is a rather spontaneous occurrence. On Earth, carbon-based nanoparticles naturally forms as products of biological decay and combustion phenomena, while silicate nanoparticles are normally present in dust storms and a variety of chemically different NPs are released

during volcanic eruptions [2, 3]. Along with their investigation, the debate on their effect on the human health is nowadays open, trying to apply a distinction between naturally occurring and human synthesized particles, mostly regarding their interaction with the environment [4]. Besides the improvement of the characterization methods, NPs synthesis rapidly developed in a vast range of disciplines, leading to their extensive production and application.

A significant part of practical application of NPs nowadays is related to their enhanced chemical properties [5]. For particles size of few thousands of atoms, a peculiar chemical reactivity arises from the high density of under-coordinated atoms. Edges, corners and steps are known to be the most chemically active sites, and their volume density naturally increases with the decrease of particles size. Atoms in these sites have a different electronic structure respect the ones in the bulk and they generally give rise to dangling bonds, which assume different geometrical configuration depending on the particular position of the atom. This dangling bonds have a major role in the chemical reaction that can take place on NPs, therefore the in-depth characterization of the NPs surface is at the basis of the design of novel nanostructures tailored for specific duties [6].

Along with chemical properties, NPs can exhibit many other peculiar aspects. Magnetic nanoparticles, for example, are of great interest for a wide range of disciplines, as data storage, magnetic fluids and nanomedicine [7, 8]. Fe and Co-based nanoparticles below few nm in size, for example, exhibit superparamagnetic behaviour [9] and they are employed in many of the mentioned fields of application. Optoelectronic properties, to make a further example, in particular the plasmonic features of nanoparticles have gained a lot of importance in the field of chemical and biological sensing, through the Localized Surface Plasmon Resonance Spectroscopy and Surface-Enhanced Raman Scattering [10–12].

A primary issue in working with NPs is certainly their production, since a series of requirements are usually needed, starting from a good control on their size, which is a key parameter that determines their properties. It is then necessary to produce NPs with sufficient thermal and chemical stability, and to avoid coalescence phenomena. Since long time, nanoparticles have been investigated both in solution and in solid state, and various strategies were implemented to achieve these results. In any case, another significant aspect is that even a perfectly homogeneous and stable population of NPs is affected by its environment, due to the interaction with the surrounding chemical species.

For the aim of our investigation, as for the majority of non-biological application, the use of a solid substrate instead of a liquid environment presents several advantages. A solid support can indeed serve as an effective template

for particles growth and generally allows to reach a higher thermal stability. At the same time, the environmental interaction on nanoparticles is defined by the supporting surface, that can be properly chosen and controlled. There are several reports showing that particles can be affected by their substrate and, viceversa, that surfaces can be modified by supported nano-objects.

The interplay between nanoparticles and 2D substrates has been largely explored, bringing to the production of composite materials, whose properties are based on the peculiar phenomena that take place in these nanostructures. The spillover, for example, is among these. It consists in the migration of adatoms from typically metallic particles to their support. It was observed firstly in 1964 [13] and nowadays the interest in spillover is renewed, both in the field of catalysis and hydrogen storage [14–16]. Several examples are indeed present in literature of NPs–2D assembly, about practical applications of this phenomenon [17, 18].

Another effect of the interaction between particles and substrate, that was employed in the construction of tailored materials, is the electric charge transfer. This mechanism involves the valence band states of the materials constituting the nano-assembly, typically modifying the occupation of their electronic states and giving rise to particular electronic, optical or chemical properties. In the latter perspective, NPs–2D assembly were investigated for the development of catalysts, whose efficiency emerges from the electronic structural modification induced in the particles by their supporting surface [19–21].

The effectiveness of this strategy has been extensively proved, opening new paths for the creation of nano-engineered materials, in which particles and surfaces can be seen as interchangeable building blocks. In this perspective, the degrees of freedom related to supporting surfaces were widely explored, with a particular attention to the novel 2D materials introduced over the years which showed unique characteristics which cannot be found in the previously investigated solid surfaces.

Nowadays the number of 2D materials is considerable and continuously growing; bi-dimensional allotrope of carbon, silicon, germanium, phosphorus, boron have been postulated and observed, while, on the other hand, further 2D materials have been derived from layered bulk structures, as for example hexagonal boron nitride and transition metal dichalcogenides [22]. If we just consider the number of known existing layered material and the number of possible combination between transition metals and chalcogens, the number of bi-dimensional materials is still expected to grow in the next years.

In front of this, graphene remains a reference, not only because of the

in-depth knowledge of its properties and the well established methods for its preparation, modification and handling that have been improved until now. Indeed graphene proved to be a low cost material, with electronic and mechanical properties that still remain at the top of what the state of the art 2D-materials can offer. This carbon allotrope has been studied since the beginning of the century as the innovative 2D compound that, for its outstanding properties, would have been the core of new nano-fabricated materials. For these reasons we selected it as a basis for the creation of a tunable substrate for supporting NPs.

From the electronic point of view, graphene is defined as a zero-gap semiconductor, showing an electronic density of states that is equal to zero at the Fermi level[1], but on the other way, its electronic conductivity is exceptionally high, due to the linear energy-momentum dispersion of the π electrons that behave as zero-mass relativistic particles. In addition, the π bonds formed by the sp^2 hybridized orbitals build a particularly stable structure with respect to mechanical and thermal stress.

To fully exploit the properties of graphene in different applications, several strategies were developed to alter it in a controlled manner. Hystorically, one of the most important issues to address about graphene is the absence of a finite energy gap in its electronic structure, which prevents it to be used as a high-conductivity semiconductor. The attempt to modify the graphene valence and conduction bands in order to open a gap and possibly preserve the shape of the Dirac cones were based on different approaches [23]. The chemical functionalization of graphene in solution is a very common technique, but generally presents limitations in the switchover to solid-state applications. Specifically designed solid surfaces can be used as interacting supports, capable to affect the graphene properties; from one hand, solid surfaces are relatively easy to prepare and functionalise, but the direct synthesis of graphene on top of them is not always possible and its transfer is not always efficient. Nevertheless, among the advantages in working directly on a metal surface, as we did, there is the possibility to apply the growth procedures that produce the highest-quality graphene, more specifically, the Chemical Vapour Deposition (CVD, see chapter 3.2). This method is the one we adopted to grow a graphene layer with large flakes and low defect density.

The substrate we used for the CVD graphene growth is Ir (111). On this crystalline surface high-quality graphene can be directly grown, with the par-

[1] We are referring to the properties of graphene in the ideal free-standing condition, that means when it doesn't interact with any solid substrate or solvent.

ticularity that its interaction with the substrate is low enough to leave its electronic structure in a condition not so dissimilar from the free-standing state [24]. For this reason we consider Gr/Ir (111) a good reference system for the investigation of the effects of graphene on the supported nanoparticles. That said, our goal was to make a step further, exploring the possibility to modify the electronic properties of graphene and creating novel tailored substrates for NPs.

To achieve this goal we exploited a method that demonstrated to be effective in the Gr modification, which is the intercalation of atoms between Gr and Ir (111) to obtain an interfacial layer [25, 26]. This preparation scheme allows the preservation of the structural characteristic of epitaxially grown graphene (few defects and large flakes) and provides the possibility to create a novel substrate. The intercalation process was introduced a decade ago as an efficient method to quench the substrate interaction. What we did instead is to use this technique to tune the interaction by modulating the composition of the interface layer.

In particular, we focused on the intercalation of metal oxides. By depositing metal atoms and exposing the Gr/Ir(111) sample to oxygen at high temperature, it is possible to form a thin metal oxide layer between the graphene and the metallic substrate.

In the preparation of the composite substrates described above, High-Resolution Photoelectron Spectroscopy with synchrotron radiation proved to be a very efficient tool, providing a detailed characterization of the nanostructures we prepared from the electronic, structural and chemical point of view.

The prototypical structures we designed to investigate the metal oxide NPs are reported in fig 1.1.

We considered different transition metals as constituents for a series of metal oxide substrates with the aim to identify their graphene tuning capabilities. At the same time, we used them to synthesize metal oxide nanoparticles on graphene for studying their dependence from the substrate. The choice of using the same material both as intercalant and particles constituent is due to our intention to understand the differences in the Gr/substrate and in the NPs/Gr interactions, irrespective of the chemical species.

Our further purpose was to combine the study of the fundamental behaviour of supported nanoparticles with one of the most significant application in the context of heterogeneous catalysis: the production of hydrogen from a photo-

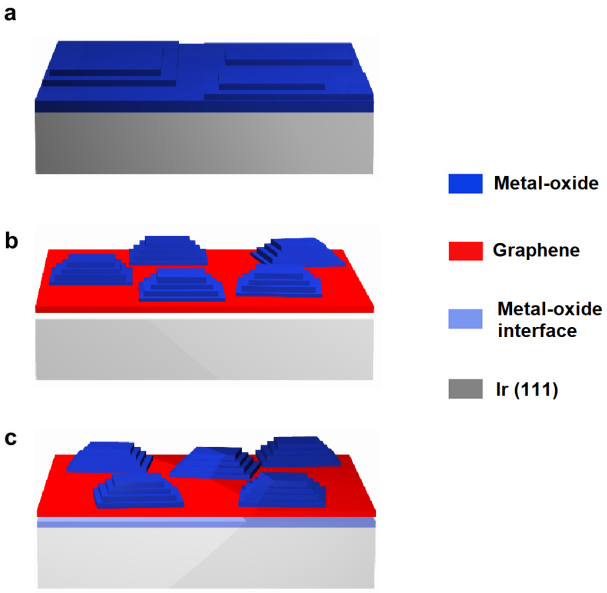

Figure 1.1: Scheme of the structures of the interfaces we prepared for each metal: Ti, Fe and Co. Metal oxide is represented in blue and light blue, graphene in red. As a substrate we used an iridium single crystal, cut along the (111) crystallographic plane.

catalytic water splitting reaction. This reaction has been known for decades to occur on many metal oxides [27], but high-performance cost-effective photocatalysts are yet to be found. The efficiency of a photocatalyst is strictly related to its electronic structure, that determines the dynamics of the fundamental steps of the process, from light absorption to photogenerated electric charge migration and recombination. The design of the nanostructured interfaces described here gives us the possibility to modify the metal oxide characteristics and therefore appears as a promising method for the construction of catalysts with higher efficiency. In this respect, we selected three important elements of the periodic table, namely iron, cobalt and titanium.

Titanium dioxide, also called titania, is well known for its wide range of applications, for example in solar cells, or as an efficient photocatalyst for several oxidation reactions, in particular the electrochemical and photocatalytic water splitting [28, 29]. Titania nanoparticles were introduced in order to improve the photocatalytic activity of the parent bulk material [30] and further improvements were obtained by associating them with carbon materials. A remarkable result obtained through this strategy was the extension of the light absorption range from UV to visible [31], which is one of the main challenges in TiO_2

photocatalysis [32]. On the basis of these successful attempts, generic carbonaceous materials were substituted by graphene, both in solution and on solid surfaces [33, 34]. Graphene-based titania nanocomposites have shown outstanding photocatalytic performances. The reason of this performance enhancement is not fully clear yet, but it is reasonably attributed to the interaction between graphene and particles, as the reduced size of the material alone is not sufficient to account for it [35]. Epitaxial graphene then proved to be a very effective substrate for nanoclusters deposition, allowing the control of their size and to hinder their coalescence [36].

Iron oxide, on the other hand, has been widely explored as a photocatalyst owing to its reduced band gap with respect to other well-known catalysts, the low cost of the material and its chemical stability [37]. Its practical applications are mostly limited by its low carrier mobility, yet remarkable enhancement have been obtained on the iron oxide photocatalytic activity by using it in association with graphene and carbon nanocomposites [38–40].

Cobalt oxide based nanostructures have shown significant activity for the photocatalytic water oxidation reaction [41–43]. Moreover, such cobalt species can also activate wide-band-gap semiconductors towards visible-light water oxidation [44] and they have been used in association with graphite and carbon nanocomposites, achieving remarkable activity as electrocatalysts [45, 46]. The reduced band gap of cobalt oxide with respect to other typical catalysts and its relatively low cost have attracted the attention of the materials science community in the last few years [47, 48].

The NPs-based interfaces we investigated contain size-dispersed particles on the order of tens nanometers. A promising improvement in the characterization of these interfaces could be achieved performing the same measurements on systems formed by identical particles and exploring in detail the dependence of their properties on their size. A further step could be done by decreasing their diameter down to the fractions of a nanometer. Such small particles, frequently named clusters, are indeed aggregates of a small number of atoms that are characterized by a molecular-like electronic structure. In our case, investigating these systems could potentially allow to produce further high-performance photocatalysts. To perform this kind of investigation, the production of clusters all with exactly the same number of atoms is a priority, since the addition or removal of a single atom can produce dramatic modifications. To produce small mono-dispersed atomic clusters, the vapour deposition techniques described before are definitely not effective.

The first introduced synthesis methods to achieve this result were gener-

ally based on two distinct approaches, namely top-down, e.g. electron beam lithography, or bottom-up, e.g. wet chemical processes and vapour deposition on solid surfaces. Nevertheless, the employment of these strategies usually outputs a population of clusters with a narrow size distribution, but no atomic precision in size. For all these techniques the particles are often interacting with the environment since the beginning of their production, and this interaction unavoidably affects the growth mechanism. The alternative way to proceed is to generate free clusters and to deposit them on a solid support afterwards.

Following this concept, dedicated complex experimental facilities have been designed. These were firstly introduced in the '80s of the last century, when nano-objects became a major interest among solid state physicists and chemists, and they were continuously developed until today. A state of the art nanocluster source is installed at the Surface Science Laboratory of Elettra.

The fundamental working principle of this kind of cluster sources is the aggregation of raw material single atoms in free clusters into a vacuum chamber. Diverse methods for the production of monomers have been used during the years; laser ablation is one of the most efficient and the one implemented in our apparatus. In general, after their creation, monomers are driven by a cold carrier gas through an adiabatic expansion during which the cluster formation takes place. At this point, by means of a mass analyser clusters with a precise charge/mass ratio are selected with an accuracy that can reach the single atomic unit.

In the last chapter of this thesis, the details of the working mechanisms of our cluster source will be discussed, along with some improvements and functional test that I have performed. The aim of this mass-selected nanocluster source is to deposit monodispersed clusters on solid surfaces and to characterize them with space-averaging techniques. The final part of the develompent plan for this machine will be its connection to the SuperESCA beamline at the Elettra synchrotron radiation facility. The combination with synchrotron radiation will provide a new way to access the properties of nanoclusters from the electronic and chemical perspective and will be an extremely useful tool for the future design of new nanostructured materials.

References

[1] Wagner, F. E.; Haslbeck, S.; Stievano, L.; Calogero, S.; Pankhurst, Q.; Martinek, K.-P. Before striking gold in gold-ruby glass. *Nature* **407**, 691 (2000).

[2] Jeevanandam, J.; Barhoum, A.; Chan, Y. S.; Dufresne, A.; Danquah, M. K. Review on nanoparticles and nanostructured materials: history, sources, toxicity and regulations. *Beilstein Journal of Nanotechnology* **9**, 1050 (2018).

[3] Hochella Jr, M. F. There's plenty of room at the bottom: Nanoscience in geochemistry. *Geochimica et Cosmochimica Acta* **66**, 735 (2002).

[4] Wagner, S.; Gondikas, A.; Neubauer, E.; Hofmann, T.; von der Kammer, F. Spot the difference: engineered and natural nanoparticles in the environment—release, behavior, and fate. *Angewandte Chemie International Edition* **53**, 12398 (2014).

[5] Burda, C.; Chen, X.; Narayanan, R.; El-Sayed, M. A. Chemistry and properties of nanocrystals of different shapes. *Chemical Reviews* **105**, 1025 (2005).

[6] Boles, M. A.; Ling, D.; Hyeon, T.; Talapin, D. V. The surface science of nanocrystals. *Nature Materials* **15**, 141 (2016).

[7] Lu, A.-H.; Salabas, E. e.; Schüth, F. Magnetic nanoparticles: synthesis, protection, functionalization, and application. *Angewandte Chemie International Edition* **46**, 1222 (2007).

[8] Reiss, G.; Hütten, A. *Handbook of Nanophysics*; CRC press, 2016; pp 28–40.

[9] Bansmann, J. et al. Magnetic and structural properties of isolated and assembled clusters. *Surface Science Reports* **56**, 189 (2005).

[10] Eustis, S.; El-Sayed, M. A. Why gold nanoparticles are more precious than pretty gold: noble metal surface plasmon resonance and its enhancement of the radiative and nonradiative properties of nanocrystals of different shapes. *Chemical Society Reviews* **35**, 209 (2006).

[11] Willets, K. A.; Van Duyne, R. P. Localized surface plasmon resonance spectroscopy and sensing. *Annual Reviews of Physical Chemistry* **58**, 267 (2007).

[12] Anker, J. N.; Hall, W. P.; Lyandres, O.; Shah, N. C.; Zhao, J.; Van Duyne, R. P. *Nanoscience And Technology: A Collection of Reviews from Nature Journals*; World Scientific, 2010; p 308.

[13] Khoobiar, S. Particle to particle migration of hydrogen atoms on platinum—alumina catalysts from particle to neighboring particles. *The Journal of Physical Chemistry* **68**, 411 (1964).

[14] Prins, R. Hydrogen spillover. Facts and fiction. *Chemical Reviews* **112**, 2714 (2012).

[15] Srinivas, S.; Rao, P. K. Direct observation of hydrogen spillover on carbon-supported platinum and its influence on the hydrogenation of benzene. *Journal of Catalysis* **148**, 470 (1994).

[16] Parambhath, V. B.; Nagar, R.; Sethupathi, K.; Ramaprabhu, S. Investigation of spillover mechanism in palladium decorated hydrogen exfoliated functionalized graphene. *The Journal of Physical Chemistry C* **115**, 15679 (2011).

[17] Vayssilov, G. N.; Lykhach, Y.; Migani, A.; Staudt, T.; Petrova, G. P.; Tsud, N.; Skála, T.; Bruix, A.; Illas, F.; Prince, K. C.; Matolin, V.; Neyman, K. M.; Libuda, J. Support nanostructure boosts oxygen transfer to catalytically active platinum nanoparticles. *Nature Materials* **10**, 310 (2011).

[18] Wang, H.; Dai, H. Strongly coupled inorganic–nano-carbon hybrid materials for energy storage. *Chemical Society Reviews* **42**, 3088 (2013).

[19] Corma, A.; Garcia, H. Supported gold nanoparticles as catalysts for organic reactions. *Chemical Society Reviews* **37**, 2096 (2008).

[20] Shi, J. On the synergetic catalytic effect in heterogeneous nanocomposite catalysts. *Chemical Reviews* **113**, 2139 (2012).

[21] Gunasooriya, G. T. K. K.; Saeys, M. *Nanotechnology in Catalysis: Applications in the Chemical Industry, Energy Development, and Environment Protection*; Wiley-VCH, 2017; p 209.

[22] Butler, S. Z.; Hollen, S. M.; Cao, L.; Cui, Y.; Gupta, J. A.; Gutiérrez, H. R.; Heinz, T. F.; Hong, S. S.; Huang, J.; Ismach, A. F.; *et al.*, Progress, challenges, and opportunities in two-dimensional materials beyond graphene. *ACS Nano* **7**, 2898 (2013).

[23] Liu, H.; Liu, Y.; Zhu, D. Chemical doping of graphene. *Journal of Materials Chemistry* **21**, 3335 (2011).

[24] Pletikosić, I.; Kralj, M.; Pervan, P.; Brako, R.; Coraux, J.; N'diaye, A.; Busse, C.; Michely, T. Dirac cones and minigaps for graphene on Ir (111). *Physical Review Letters* **102**, 056808 (2009).

[25] Larciprete, R.; Ulstrup, S.; Lacovig, P.; Dalmiglio, M.; Bianchi, M.; Mazzola, F.; Hornekær, L.; Orlando, F.; Baraldi, A.; Hofmann, P.; Lizzit, S. Oxygen switching of the epitaxial graphene–metal interaction. *ACS Nano* **6**, 9551 (2012).

[26] Presel, F.; Jabeen, N.; Pozzo, M.; Curcio, D.; Omiciuolo, L.; Lacovig, P.; Lizzit, S.; Alfe, D.; Baraldi, A. Unravelling the roles of surface chemical composition and geometry for the graphene–metal interaction through C1s core-level spectroscopy. *Carbon* **93**, 187–198 (2015).

[27] Chen, X.; Shen, S.; Guo, L.; Mao, S. S. Semiconductor-based photocatalytic hydrogen generation. *Chemical Reviews* **110**, 6503 (2010).

[28] Fujishima, A.; Honda, K. Electrochemical photolysis of water at a semiconductor electrode. *Nature* **238**, 37 (1972).

[29] Thompson, T. L.; Yates, J. T. Surface science studies of the photoactivation of TiO_2 new photochemical processes. *Chemical Reviews* **106**, 4428 (2006).

[30] Pelaez, M.; Nolan, N. T.; Pillai, S. C.; Seery, M. K.; Falaras, P.; Kontos, A. G.; Dunlop, P. S.; Hamilton, J. W.; Byrne, J. A.; O'shea, K. A review on the visible light active titanium dioxide photocatalysts for environmental applications. *Applied Catalysis B: Environmental* **125**, 331 (2012).

[31] Sakthivel, S.; Kisch, H. Daylight photocatalysis by carbon-modified titanium dioxide. *Angewandte Chemie International Edition* **42**, 4908 (2003).

[32] Etacheri, V.; Di Valentin, C.; Schneider, J.; Bahnemann, D.; Pillai, S. C. Visible-light activation of TiO_2 photocatalysts: Advances in theory and experiments. *Journal of Photochemistry and Photobiology C: Photochemistry Reviews* **25**, 1 (2015).

[33] Williams, G.; Seger, B.; Kamat, P. V. TiO_2-graphene nanocomposites. UV-assisted photocatalytic reduction of graphene oxide. *ACS Nano* **2**, 1487 (2008).

[34] Ma, Y.; Wang, X.; Jia, Y.; Chen, X.; Han, H.; Li, C. Titanium dioxide-based nanomaterials for photocatalytic fuel generations. *Chemical Reviews* **114**, 9987 (2014).

[35] Zhang, H.; Lv, X.; Li, Y.; Wang, Y.; Li, J. P25-graphene composite as a high performance photocatalyst. *ACS Nano* **4**, 380 (2009).

[36] Gerber, T.; Busse, C.; Mysliveček, J.; Coraux, J.; Michely, T. A versatile fabrication method for cluster superlattices. *New Journal of Physics* **11**, 103045 (2009).

[37] Wu, W.; Jiang, C.; Roy, V. A. Recent progress in magnetic iron oxide–semiconductor composite nanomaterials as promising photocatalysts. *Nanoscale* **7**, 38 (2015).

[38] Lefèvre, M.; Proietti, E.; Jaouen, F.; Dodelet, J.-P. Iron-based catalysts with improved oxygen reduction activity in polymer electrolyte fuel cells. *Science* **324**, 71 (2009).

[39] Wang, Y.; Wang, Q.; Zhan, X.; Wang, F.; Safdar, M.; He, J. Visible light driven type II heterostructures and their enhanced photocatalysis properties: a review. *Nanoscale* **5**, 8326 (2013).

[40] Lin, Y.; Geng, Z.; Cai, H.; Ma, L.; Chen, J.; Zeng, J.; Pan, N.; Wang, X. Ternary graphene–TiO_2–Fe_3O_4 nanocomposite as a recollectable photocatalyst with enhanced durability. *European Journal of Inorganic Chemistry* **2012**, 4439 (2012).

[41] Zhang, M.; De Respinis, M.; Frei, H. Time-resolved observations of water oxidation intermediates on a cobalt oxide nanoparticle catalyst. *Nature Chemistry* **6**, 362 (2014).

[42] Jiao, F.; Frei, H. Nanostructured cobalt oxide clusters in mesoporous silica as efficient oxygen-evolving catalysts. *Angewandte Chemie International Edition* **48**, 1841 (2009).

[43] Jiao, F.; Frei, H. Nanostructured cobalt and manganese oxide clusters as efficient water oxidation catalysts. *Energy & Environmental Science* **3**, 1018 (2010).

[44] Maeda, K.; Ishimaki, K.; Tokunaga, Y.; Lu, D.; Eguchi, M. Modification of Wide-Band-Gap Oxide Semiconductors with Cobalt Hydroxide Nanoclusters for Visible-Light Water Oxidation. *Angewandte Chemie International Edition* **55**, 8309 (2016).

[45] Pereira, G. M.; Cellet, T. S.; Gonçalves, R. H.; Rubira, A. F.; Silva, R. Trapped metallic cobalt nanoparticles in doped porous graphite: An electrocatalyst that gets better over reaction time. *Applied Catalysis B: Environmental* **217**, 144 (2017).

[46] Liang, Y.; Wang, H.; Diao, P.; Chang, W.; Hong, G.; Li, Y.; Gong, M.; Xie, L.; Zhou, J.; Wang, J.; Regier, T. Z.; Wei, F.; Dai, H. Oxygen reduction electrocatalyst based on strongly coupled cobalt oxide nanocrystals and carbon nanotubes. *Journal of the American Chemical Society* **134**, 15849 (2012).

[47] Jaouen, F.; Proietti, E.; Lefèvre, M.; Chenitz, R.; Dodelet, J.-P.; Wu, G.; Chung, H. T.; Johnston, C. M.; Zelenay, P. Recent advances in non-precious metal catalysis for oxygen-reduction reaction in polymer electrolyte fuel cells. *Energy & Environmental Science* **4**, 114 (2011).

[48] Hunter, B. M.; Gray, H. B.; Muller, A. M. Earth-abundant heterogeneous water oxidation catalysts. *Chemical Reviews* **116**, 14120 (2016).

Chapter 2

Experimental techniques

In this chapter, a description will be given of the main experimental techniques used in my research activity. The principles of each technique will be discussed along with the corresponding data analysis methods. The discussion will be focused on the features that are related to the study of solid surfaces and to the experiments described in this thesis.

Particular attention will be paid to the surface sensitivity of the experimental techniques and on the methods applied for the preparation of our samples. In this respect, vacuum condition are paramount to perform surface science experiments.

The first reason for the use of vacuum equipment is the need to minimize the environmental contamination of the sample. A thick layer of adsorbed impurities is typically formed on surfaces at atmospheric pressure and the formation of an oxide layer hampers the investigation of several metal surfaces. The level of vacuum required for a surface science experiment can be calculated on the basis of the time duration of the experiment, considering the rate at which atoms and molecules in the environment deposit on the sample. It can be calculated, from the Hertz-Knudsen relation, that in order to preserve the cleanliness of a surface for a time interval of the order of several hours, a pressure of about 10^{-10} mbar is needed [1].

Vacuum condition are also exploited for the implementation of a series of measuring equipment. In fact, many surface science experimental techniques use free electrons as probe. Electron-based techniques have important advantages in the study of solid surfaces compared to photon, ions and atoms, also used in the study of condensed matter: (i) the mean free path of low energy electrons in a solid is only few Å, therefore they can be used as surface sensitive probes;

(ii) electrons are easily focused and tuned in energy; (iii) they are easy to detect and count; (iv) both their kinetic energy and momentum can be analysed by a relatively simple and flexible electrostatic optical setup [2]. A pressure below 10^{-6} mbar is needed for working with 10 to 100 eV kinetic energy electrons. Their mean free path has indeed to be larger than the size of the experimental apparatus, which is typically of the order of 1 m. The first technique discussed in this section is an example of electron spectroscopy.

2.1 X-Ray Photoelectron Spectroscopy

X-ray Photoelectron Spectroscopy (XPS) is one of the most powerful quantitative spectroscopic methods to retrieve chemical information from solid surfaces. The measurement of the kinetic energy of electrons emitted by photoelectric effect is at the basis of this spectroscopic technique. It was fully developed by K. Siegbahn in 1957 [3] with the aim of collecting chemical information from "*atoms, molecules, and condensed matter*" [4]. For this reason it was also referred to as Electron Spectroscopy for Chemical Analysis (ESCA)

2.1.1 Principles and setup

From the theoretical point of view, a simplified but effective way to describe the photoemission process is the so called three-step model [2]. In this framework the photoemission process from a solid is schematized as: (i) photon-induced excitation of an electron to an excited state; (ii) migration of the excited electron through the material to the surface; (iii) electron escape from the surface to the vacuum level.

Energy conservation implies a relation between the binding energy of the electron in atoms and its kinetic energy in vacuum. Therefore, it is possible to retrieve information about the electronic structure of the investigated material through the interpretation of the energy distribution curve of the photoelectrons (see figure 2.1a).

The experimental setup is ideally constituted by a monochromatic photon source which is used to induce the photoemission process and an electron energy analyser used to measure the kinetic energy of the photoemitted electrons.

Let's consider a photoemission process induced by monochromatic radiation with $h\nu$ photon energy. The kinetic energy of the emitted electron in vacuum will be $\mathrm{E}'_K = h\nu - \mathrm{E}_B - \Phi_S$, where Φ_S is the sample's work function (figure 2.1b). Taking into account that the electron energy analyser has also a proper

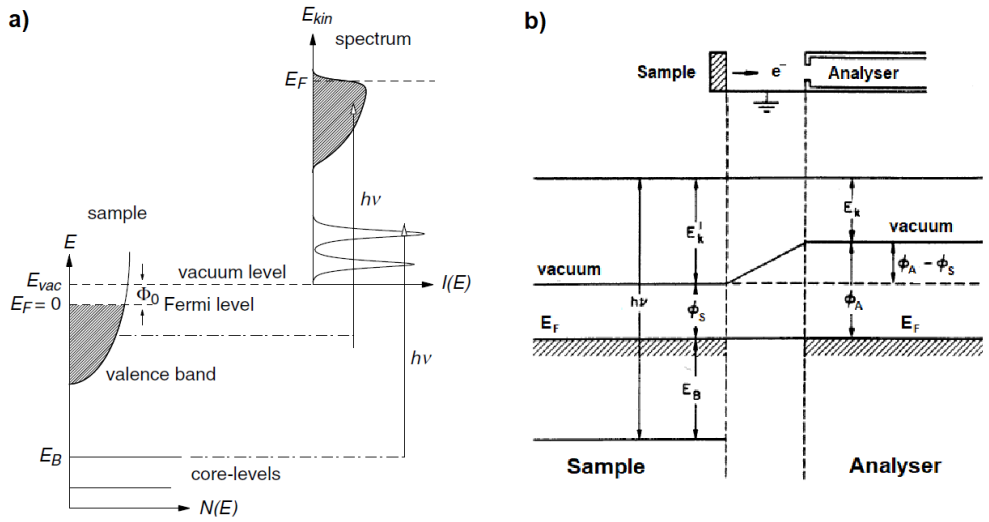

Figure 2.1: a) Energy diagram for the photoemission process: on the left side is represented the density of states of the sample, on the right the corresponding photoemission signal obtained using $h\nu$ photon energy monochromatic radiation; b) energy diagram for the photoemission process considering the analyser as part of the physical system.

work function Φ_A, if the sample and the analyser are in electric contact and their Fermi levels are aligned, the following relation is valid

$$h\nu - \mathrm{E}_B = \mathrm{E}_K + \Phi_S + (\Phi_A - \Phi_S)$$

where E_K is the measured kinetic energy. As a result we obtain a simple expression for E_B that does not depend on the work function of the sample, but is related to the one of the analyser.

The quantity Φ_A depends from the specific configuration of the analyser, therefore, to measure E_B with high accuracy, a calibration of the instrument is needed. The calibration can be done on the basis of known binding energy values of some reference spectral features. Alternatively, the binding energy values can be corrected in order to obtain that the the binding energy E_B^F of electrons at the Fermi level is zero. This requires the sample to be metallic and the kinetic energy E_K^F of the electrons at $\mathrm{E_F}$ to be measured. In this way we would have

$$0 = E_B^F = h\nu - E_K^F - \Phi_A$$

from which

$$E_B = -E_K + E_K^F$$

It has to be noticed that binding energies measured by photoemission spectroscopy tends to overestimate the real values, since the relaxation of the atom after the photoemission process is neglected, within the so called Koopmans' approximation.

Concerning the experimental setup, few consideration has to be done on the photon source. The binding energy range that can be investigated by photoelectron spectroscopy is determined by the photon energy. Soft X-ray sources are needed to perform photoemission measurements on the atomic core levels. In order to obtain good energy resolution spectra, particular attention has to be paid to the energy resolution of the source. In surface science laboratories fluorescent sources emitting Mg-Kα and Al-Kα radiation ($h\nu = 1253.6$ eV and 1486.6 eV, respectively) are typically used. These kind of sources are sometimes associated to a monochromator.

Synchrotron radiation can alternatively be used to excite photoelectron, with a series of outstanding advantages with respect conventional sources, such as (i) high brightness (number of photon per second per unit source size and divergence in a given bandwidth), (ii) higher photon energy resolution and (iii) photon energy tunability. The high brightness reduces the measurement acquisition time and allows to acquire photoemission spectra in time-resolved mode during experiments. The photon energy resolution achievable with synchrotron radiation allows a deeper analysis of photoemission spectra, while the tunability of the photon allows to select the kinetic energy of the photoelectrons in order to maximize the surface sensitivity and can be exploited to enhance the photoemission signal by selecting hν values at which the photoemission cross section is maximized.

On the other hand, the electron kinetic energy analysis has to be performed with comparable efficiency with respect to the photon source, in terms of kinetic energy resolution and electron counts per second. To this aim, the concentric hemispherical analyzer (CHA) is typically used. In figure 2.2a, a representation of this instrument is shown. An analogous instrument has been used for all the XPS measurements described in this thesis. It is constituted by a set of electrostatic lenses that collects photoemitted electrons and delivers them between two concentric hemispherical static electrodes. The trajectories of the photoelectrons passing through the entrance slit of the CHA are dispersed in angle depending on their kinetic energy. On the other side of the CHA electrons with a defined kinetic energy are collected by the detector.

The photoemission spectrum is acquired by counting the number of electrons emitted at a given kinetic energy and by scanning the kinetic energy

values. The apparatus is design to operate by keeping the kinetic energy of the electrons passing through the CHA constant and to perform the energy scan by means of the electrostatic lenses placed before the CHA. This operational mode is implemented to keep constant the energy resolution of the instrument, that can be calculated on the basis of few parameters as described by the following relation

$$\Delta E = E_0 \left(\frac{w}{2R_0} + \frac{\alpha^2}{4} \right)$$

where E_0 is the pass energy, w is the width of the slit at the entrance of the CHA, R_0 is the radius of the electron trajectory and α is the angular acceptance of the of the analyser, expressed in radians.

The symmetry of the CHA causes the dispersion in the radial direction of electrons having different kinetic energies and, at the same time, the focusing of electrons entering the CHA with same energy but different angle (see figure 2.2b). By implementing an electron detector with multiple channels distributed in the radial direction it is possible to acquire a small portion of the photoemission spectrum keeping the potentials of the analyser lenses fixed. With this configuration it is possible to reduce the acquisition time preserving the energy resolution or, alternatively, provided a sufficient number of detector channels and a sufficient photon flux (typically provided by synchrotron radiation) it is possible to acquire spectra in real-time.

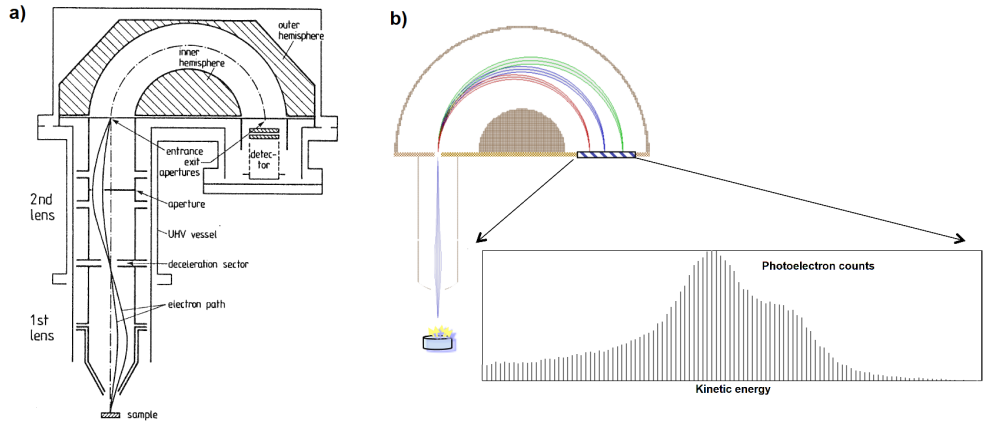

Figure 2.2: a) Section of a Concentric Hemispherical Analyser (CHA), image from [9]. b) Representation of the trajectories of electrons entering the CHA with three different values of kinetic energy and a finite angular dispersion. Red trajectories are followed by the less energetic electrons.

2.1.2 Data analysis

As mentioned, chemical investigation is the main purpose of X-ray photoelectron spectroscopy. Photoemission spectra can be used as fingerprints for the identification of the chemical species present in the sample. To that end, the measurements of the core electrons binding energies is the most effective way.

Atomic core levels are indeed determined by the chemical species of the atoms under investigation and are easily distinguishable among the features of a typical photoemission spectrum. Furthermore, the binding energy of the core electrons can be affected by the chemical environment of the atom, described in terms of chemical interaction with the surrounding atoms, number and kind of atomic bonds, geometrical configuration. This binding energy variation of the core levels is usually referred to as chemical shift and it is one of the most important aspects in photoemission data analysis. It can provide in fact detailed information about the chemical and structural properties of the sample.

A single core level XPS spectrum consists of a peak in the photoemission signal whose line shape depends on a series of factors. The natural width of the atomic energy level is responsible for a Lorentzian distribution. To this intrinsic broadening of the photoemission signal, a Gaussian contribution is convoluted to describe the finite experimental resolution and the inhomogeneous broadening generated by inelastic scattering events involving photoelectrons inside the sample. The distribution of the geometrical and chemical inequivalent atomic configurations is responsible for a further Gaussian broadening.

In addition, for the case of metallic samples, electron-hole pairs can be excited near the Fermi energy within a continuum energy spectrum. The kinetic energy loss of the photoelectron due to this effect is responsible for an asymmetric broadening of the photoemission component towards lower kinetic (higher binding) energies.

The analytic function that can be used to describe a photoemission peak from a core level of a metallic element was given by Doniach and Šunjić [5]

$$DS_{\gamma,\alpha}(\epsilon) = \frac{\Gamma(1-\alpha)}{(\epsilon^2+\gamma^2)^{(1-\alpha)/2}} \cdot \cos\left(\frac{\pi\alpha}{2} + (1-\alpha)\arctan\left(\frac{\epsilon}{\gamma}\right)\right) \tag{2.1}$$

where $\Gamma(x)$ is the Euler gamma function.

The asymmetry of a Doniach-Šunjić line profile depends on the parameter α. For $\alpha = 0$ the DS function reverts to a Lorentzian distribution. The convolution of the DS with a Gaussian function can be finally used to describe an experimental core level spectrum.

The photoemission data analysis reported in this thesis primarily consisted

of retrieving the line shape parameters of the investigated photoemission components: Lorentzian and Gaussian width, asymmetry parameter, intensity and binding energy. To do it, we executed numerical fitting procedures on the experimental data using the *DS* function convoluted with a Gaussian. A linear or Shirley background was also introduced in the fitting function to properly reproduce the spectral shape.

Quantitative analysis Photoelectron spectroscopy is a quantitative technique. The intensity of the measured photoemission signal depends in fact on the density of atoms in the portion of the sample where the radiation impinges.

In the case of heterogeneous samples, it can be useful to quantify the amount of each chemical species. The estimation of this quantity can be obtained by different strategies.

In principle, the absolute value of the atomic density can be directly measured on the basis of the photoemission intensity. To obtain this value, it would be necessary to know the photon flux Φ of the incident radiation, the cross section α of the photoemission process and the transmission function T of the hemispherical analyser. Assuming that the atomic species of interest is present only in the first atomic layer of the sample, we could estimate the atomic density d as

$$d = \frac{I}{\Phi \cdot t \cdot S \cdot \alpha \cdot T \cdot n} \tag{2.2}$$

where I is the photoemission intensity, t is the integration time, S is the areal section of the photon beam and n is the multiplicity of the electronic state. Although both photon flux and analyser transmission can be measured, a deep characterization would be needed in order to take into account their variation depending on the experimental parameters like photon energy and pass energy. If several layer were present it would be necessary to separately correct the signal intensity from each one to take into account the attenuation due to the short electron mean free path and, in case of ordered crystals, photoelectron diffraction effects could affect the intensity measurement. As a matter of fact, this calculation would be hard and affected by sensible experimental errors.

The relative comparison between the photoemission intensity generated by different chemical species is instead more reliable. It requires, in principle, to take into account only the cross section of the specific photoemission process, which is well known and tabulated. If synchrotron radiation is used, it is also necessary to take into account the variation of the radiation beam intensity as a function of the photon energy. For this reason, all the synchrotron radi-

ation photoemission spectra reported in this thesis were normalized by the photon flux. The latter was assessed by measuring the photoemission current from the refocusing mirror, i.e. the last optical element, of the beamline. The transmission efficiency of the analyser should also be considered, since it varies as a function of the kinetic energy of the photoelectrons. Nevertheless, the tuneability of the photon energy allows to select the photoelectrons kinetic energy which, in our case, ranges between 100 and 150 eV in all spectra. In such a restricted range we can reasonably approximate the analyser transmission function to a constant value.

An example of the application of the quantitative methods used in photoemission spectroscopy is given in section 2.5.2.

Work function measurements Photoemission spectroscopy can be exploited to measure the work function of a material. Work function is defined, for a metal , as the difference between the vacuum energy and the Fermi energy. The maximum kinetic energy of a photoelectron is measured for electrons emitted from the Fermi level, and it is related to the photon energy through the simple relation $E'_K \max = h\nu - \Phi_A$ (see image 2.1b). As mentioned before, we can not measure E'_K directly, due to the fact that the electron analyser has its own work function. Nevertheless this value is equal to the difference between the maximum and minimum photoelectron kinetic energies, being the latter identically equal to zero. In order practically detect electrons having kinetic energy $E'_K = 0$ it is necessary to apply a negative potential to the sample. In this way the entire photoemission spectrum can be collected and the energy of the slowest photoelectron can be measured.

To calculate the work function value is therefore necessary to determine the position of the Fermi edge in the kinetic energy scale and the onset of the photoemission signal generated by the low energy electrons (also called secondary electrons). While the first value can be retrieved with an accuracy of few tens of meV, the onset of the secondary electron energy distribution is affected by a larger error, which, in our case is of the order of hundreds of meV, depending on the sample. The accurate knowledge of the photon energy is finally needed. The error associated the this quantity for the synchrotron radiation we used in our experiment was of the order of few tens of meV. The error on the work function values we measured is therefore dominated by the one on the secondary electron energy.

2.2 Near Edge X-ray Absorption Fine Structure

By means of monochromatic and tuneable X-ray sources it is possible to perform X-ray Absorption Spectroscopy (XAS) measurements to collect electronic and structural information with chemical sensitivity which is complementary to that provided by XPS.

The physical quantity measured by XAS is the absorption coefficient μ of the sample as a function of the radiation wavelength ν.

Diverse methods have been developed to measure this quantity. The most direct one is to compare the intensity of the impinging radiation I_0 to the intensity I of the radiation passing through the sample of thickness z in transmission configuration. The value of the absorption coefficient in that case can be calculated through the simple relation

$$I = I_0 e^{-\mu z}$$

This method, though, does not provide the surface sensitivity we need to characterise our interfaces. Photoelectron detection is instead an effective way to probe the absorption coefficient providing a good degree of surface sensitivity. The number of all electrons emitted by the sample is proportional to the absorption coefficient and can be measured in the so called total electron yield configuration. Specific technical requirements have to be fulfilled to detect electron which escape the material with a wide range of kinetic energies. An alternative to the total yield is to collect only the Auger electrons emitted as a consequence of atomic relaxation after X-ray absorption. This method, called Auger yield, provide a XAS signal with high surface sensitivity, due to the low energy of the Auger electrons. Moreover, the surface sensitivity in this case does not depend on the photon energy, since the kinetic energy of Auger electrons, and therefore their mean free path inside the sample, is constant. In addition, Auger yield XAS can be performed using the same experimental setup of XPS.

In the quantum mechanics framework, the single photon absorption process is characterized by a cross section that depends, through the Fermi golden rule, on the initial and final electronic states involved in the absorption process. The XAS signal, i.e. $\mu(h\nu)$ is determined by the sum of the cross sections of all the allowed electronic transitions from an occupied to an unoccupied state. The variation of the photon energy causes a variation on the allowed transition and therefore on the XAS signal.

Significant variation of μ are detected when the photon energy overcomes

the minimum energy needed to excite an electron from a bound state to the continuum. In such a case, a step-like increase in the absorption coefficient is measured. This spectral feature, called edge, is at the center of the XAS investigation. In particular, what is inspected in XAS analysis is the oscillating behaviour of μ close to the absorption edges.

These oscillations are due to interference phenomena involving photoemitted electrons. Since the absorber atom is not isolated, the photoemitted electron has a probability to be scattered by a nearby atom. The wavefunction of the photoelectron is therefore a superposition of the outgoing and scattered wavefunctions. The absorption oscillations are determined by the phase relationship between the outgoing and scattered waves, which depend on the distance between absorber and scatterer atoms. From the analysis of the μ variation above the absorption edge is therefore possible to obtain information about the local geometric structure surrounding a given atomic species. This kind of investigation, that takes into account a wide spectral region after the edge, is named Extended X-ray Absorption Fine Structure.

Near Edge X-ray Absorption Fine Structure (NEXAFS), instead, is focused on the analysis of the spectral features within a restricted photon energy range around the absorption edge. Electron excited by photon energies that are close to the edge value have low kinetic energies and undergo multiple scattering events. The spectroscopic features in the NEXAFS region arise from these events, and carry information about the local structure and ligand symmetry around the atoms involved in the photoabsorption process. Weak changes in valence state and coordination chemistry can be assessed giving the possibility to use the NEXAFS features as fingerprints to identify chemical species inside a composite material.

The detailed interpretation and the first principle simulation of NEXAFS spectra are particularly difficult due to the complexity of the photon absorption and electron scattering phenomena. Nevertheless, it it possible to consider the NEXAFS fingerprint features to distinguish, for example, atoms having different crystal field. In this way it is possible, through a qualitative interpretation of the data, to identify the local crystal structure for specific chemical species. This is exactly what we have done to investigate the structural characteristics of our metal oxide nanoparticles.

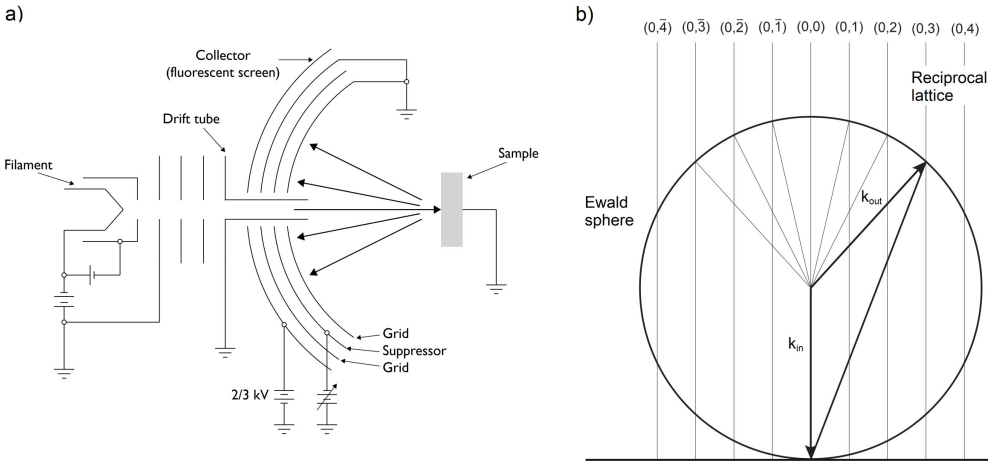

Figure 2.3: a) Schematic representation of a typical LEED apparatus; b) Side wiew of the Ewald construction.

2.3 Low Energy Electron Diffraction

Low Energy Electron Diffraction (LEED) is one of the first experimental methods introduced to study long range ordered crystalline surfaces. It was serendipitously discovered by Davisson and Germer in 1927 [6] performing experiments in vacuum on a nickel crystal. For a series of technical requirements, LEED became a common experimental tool only some decades after. Nowadays, for the simplicity of the apparatus and for the straightforward interpretation of data, LEED is one of the most widespread instruments in surface science laboratories.

LEED is an electron-in/electron-out probe technique, based on the diffraction effect experienced by a monochromatic electron beam directly shined on a crystalline surface. It is renowned for being a surface sensitive technique. For a peculiar coincidence, in fact, electrons with a de Broglie wavelength comparable with the interatomic distances in solids have an inelastic mean free path of few Å.

LEED is therefore operated in reflection configuration by means of an apparatus similar to the one shown in figure 2.3a. Free electrons are produced by thermionic emission from a filament and delivered to the sample by a set of electrostatic lenses that accelerate and focus them. After surface interaction, a series of grids suppresses the inelastically scattered electrons and accelerates the residual ones towards a phosphor screen. A CCD camera is often used to acquire digital images that can be subsequently analysed.

In the single scattering approximation electrons can be described as plane

waves that impinge on the surface with wave vector $\boldsymbol{k}_{in}$ and are scattered along preferential directions defined by wave vectors $\boldsymbol{k}_{out}$ that satisfy the Laue condition

$$\boldsymbol{k}_{in} - \boldsymbol{k}_{out} = \Delta\boldsymbol{K} \in G$$

where $\Delta\boldsymbol{K}$ is the scattering vector and G is the reciprocal lattice. It is possible to visualize this condition for a 2D crystal through the Ewald geometric construction (figure 2.3b). The reciprocal lattice of an ideal 2D crystal consists of parallel lines, shown vertically in figure. The so called Ewald sphere is defined by the modulus of the incoming wave vector, which is equal to the modulus of the outgoing one, in case of elastic scattering. In this picture, the directions of the scattered electrons are defined by the intersection between the reciprocal lattice and the Ewald sphere.

On the phosphor screen the diffraction image consists of bright spots with a definite intensity distribution centred on the directions defined by the Ewald construction. The shape of the diffraction spot can be described by the convolution between a Lorentzian and a Gaussian distribution. The first contribution comes from the surface domain size. The Lorentzian Full Width Half Maximum (L_{FWHM}) of a diffraction spot is indeed determined by the number of in-phase scatterers, and therefore to the average domain size D through an inverse proportion relation: $L_{\mathrm{FWHM}} = 2\pi/D$.

The finite resolution of the instrument is instead responsible for a Gaussian broadening of the diffraction spots. The k-space resolution of a LEED apparatus depends on the energy dispersion and on the angular divergence of the electron beam, that determines the instrumental transfer width (TW). This quantity corresponds to the maximum domain size that can be detected on a surface at a given energy value. Usually this value is of the order of 100 Å.

2.4 Scanning Tunneling Microscopy

Scanning Tunneling Microscopy (STM) is an experimental technique capable of providing direct real space images of a surface with atomic resolution. It belongs to the class of scanning probe microscopies and it is based on the space mapping of the electron tunneling current which is established between the surface atoms and the scanning metal tip. It was developed by Binning and Rohrer at the beginning of the 1980's [7] and it earned them the Nobel Prize already in 1986.

STM is a brilliant example of exploitation of a quantum mechanical effect for measurement purposes. In the STM setup, electrons penetrate the vacuum

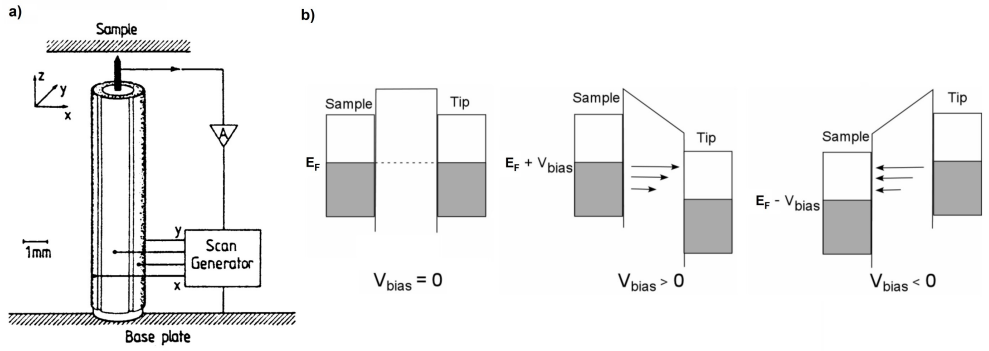

Figure 2.4: a) Diagram of a piezoelectric actuator element equipped with tip and electronic connection for scanning operation; b) electronic band scheme of metallic sample and tip for zero, positive and negative bias voltage. Images from [9].

potential barrier and tunnel from the sample to the tip (or vice-versa) with a probability that depends exponentially on the surface–tip distance.

In a simple one-dimensional approximation, the electronic transmission probability, i.e. the tunneling current, can be described by the following relation [8]

$$I \propto e^{-2\kappa d}$$

where d is the surface–tip distance, and κ is a parameter obtained from the Schrödinger's equation of a particle moving through a rectangular barrier in one dimension

$$\kappa^2 = \frac{2m}{\hbar^2}(U_B - E)$$

where U_B is the barrier potential and E is the energy of the state from which the tunneling occurs. A bias potential is applied in order to define a preferential direction for the electron tunneling. Once the tunneling current is established, since κ is on the order of $1\,\text{Å}^{-1}$, a variation of d on the order of the Å can produce a variation of one order of magnitude in the tunneling current.

There are two main operational mode for a scanning tunneling microscope. One is performed scanning the surface at constant d and measure I, which is technically easy, but requires a perfectly flat surface to avoid the tip colliding on the sample; the other one consist in scanning the sample and simultaneously adjust d in order to always measure a fixed value for I. This latter operational mode, which is the most widespread due to its flexibility, requires a specific electronic feedback system to adjust the position of the tip with a precision of 0.05–0.1 Å. The movements of the tip, both the vertical and the horizontal

ones, are typically actuated by piezoelectric motors in a configuration similar to the one reported in figure 2.4a.

In the analysis of STM measurements, one has to take into account that the tunneling current depend on the sample–tip distance through the convolution of the electronic density of states of the two objects, in particular the convolution of the occupied states on one side and unoccupied states on the other. Therefore, changing the sign of the bias voltage applied on the sample means probing the empty or the occupied states of the sample, as represented in figure 2.4b. In other words, STM does not image atoms, it images electronic states. As a consequence, while on the horizontal plane the atomic positions can be measured with remarkable accuracy, measured d values can be misleading in the description of the surface morphology, in particular when different chemical species are present on the surface [10].

In our experiments STM was used to acquire images of the metal oxide clusters grown on graphene and to investigate statistically, also using specific image processing software, their morphological characteristics.

2.5 Sample preparation methods

The methods we applied for the growth of nanostructured interfaces are subject to specific requirements concerning the experimental setup. The preparation of our samples has to be performed in ultra-high vacuum, to reduce as far as possible the presence of contaminants and to control at best the chemical composition of our nanoarchitectures. The cleanliness of the substrate as well as the purity of the materials used for the nanofabrication are of fundamental importance for the success of the experimental investigation.

On the other hand, a central aspect regarding the sample preparation is the reproducibility, which is based on the accurate control on each stage of the preparation. In our case the quantification of the material employed in the growth of the nanoarchitectures is extremely important.

These two aspects, cleanliness and quantitative control in the sample preparation, will be discussed in the next sections.

2.5.1 Crystalline surfaces cleaning

All our interfaces are grown on the surface of a single crystal of iridium, cut along the (111) crystallographic direction. Therefore, the first step of our sample preparation always consisted in cleaning the substrate.

One of the most versatile cleaning methods in UHV for metal surfaces is the ion bombardment and subsequent annealing. During the ion bombardment, usually performed with noble gas ions, the contaminants and the first layers of the surface are sputtered away. The purpose of the following annealing is to remove possible embedded and adsorbed noble gas atoms, to reduce the roughness induced by bombardment and to recover the surface cristallography. Ion bombardment and annealing usually have to be repeated to achieve best results.

The energy of the sputtering ions depend on the specific surface. For Ir (111) we applied an accelerating potential of 1.5 kV to argon ions. For softer metal, such as silver, for example, lower potentials has to be used (1 or 0.7 kV) to preserve the crystal structure. To reduce the probability of ion embedding inside the crystal, sputtering is usually performed at room temperature.

To clean a 1 cm^2 sample, as our Ir (111), typical values for the sputtering current are about 5 μA and the time needed for a sputtering treatment is 10 to 30 minutes.

The sputtering efficiency, namely the number of sputtered atoms per unit of ion current, is strongly dependent on the material. For this reason, this cleaning method is not the most suitable for inhomogeneous samples such as oxides or alloys. The ion bombardment in fact tends to change the stoichiometry of the first layers of the compound material, which can not be always recovered with a simple annealing.

As mentioned before, sputtering increases the surface roughness and induces a high degree of disorder in crystalline surfaces. The annealing temperature, as a consequence, has to be high enough to provide the atoms the necessary mobility to reform the crystal lattice. Temperature, as well as the heating rate and the annealing time is strictly related to the specific surface. For Ir (111) we performed flash annealing at 1400 K.

A peculiarity of Ir (111) is that the annealing at high temperature induces the segregation of carbon impurities from the bulk to the surface. This requires a further cleaning step, by a different methods. After sputtering and annealing carbon is almost the only contaminant present on the surface and can be removed by oxidation. Exposure of the C-covered surface to O_2 and concurrent annealing at 1000 K is employed to synthesize CO and CO_2 on the crystalline surface and to make the products of the reaction desorb. At the end of the oxygen treatment, residual oxygen atoms chemisorbed on the surface can be removed by exposing the sample to hydrogen at 350 K to form and let desorb water molecules. Residual hydrogen is then removed by a flash anneal to 500 K.

Due to carbon segregation, the cleaning cycles for Ir (111) include sputtering, annealing and oxygen treatment. Oxygen is easily sputtered off, therefore the hydrogen treatment is performed just at the end of the cleaning cycles, immediately before the beginning of the experiment.

2.5.2 Metal deposition and coverage calibration

For the growth of our nanostructured interfaces we performed metal depositions by evaporation and condensation. In particular, metallic vapours were produced by sublimation from a pure metal filament. The sample was exposed to the vapours by placing it in front of the metal evaporator, at few centimetres from the filament. This method, despite being efficient and reliable, does not allow to directly control neither the amount of material deposited on the sample, nor the evaporation rate, that have to be measured afterwards. A characterization of the evaporator is therefore necessary.

The deposition rate, i.e. the number of atoms deposited on the sample per unit of time, depends on the sample–evaporator distance and on the evaporation rate from the filament, which is in turn determined by the current flowing through the filament. These two parameters, distance and current, are determined by the specifics of the filament and those of the experimental chamber, so they can be hardly varied. The fine control on the amount of deposited material can be done more easily through the exposure time.

We will express the amount of adatoms on a surface in terms of monolayer (ML), where 1 ML is defined as the number of atoms in an atomically thin film having the same surface density of the substrate. In this thesis we will always consider Ir (111) as the reference surface.

The calibration of the deposition rate was performed by depositing fractions of a monolayer of metal on the clean substrate and subsequently measuring the coverage. To this purpose we exploited a feature of the Ir (111) photoemission spectrum, which is appreciable using a synchrotron light facility: the Surface Core Level Shift (SCLS). In figure 2.5a, the Ir $4f_{7/2}$ spectrum acquired on clean Ir (111) is shown. As mentioned before, the atomic chemical environment affect the core electrons binding energy. The reduced coordination of the atoms on the surface causes a shift of the core levels with respect to the atoms in the bulk, the so called SCLS. This gives the possibility to distinguish the photoemission signal from the surface atoms from that of the bulk, simplifying the quantitative analysis.

The presence of adatoms on the surface modifies the chemical environment

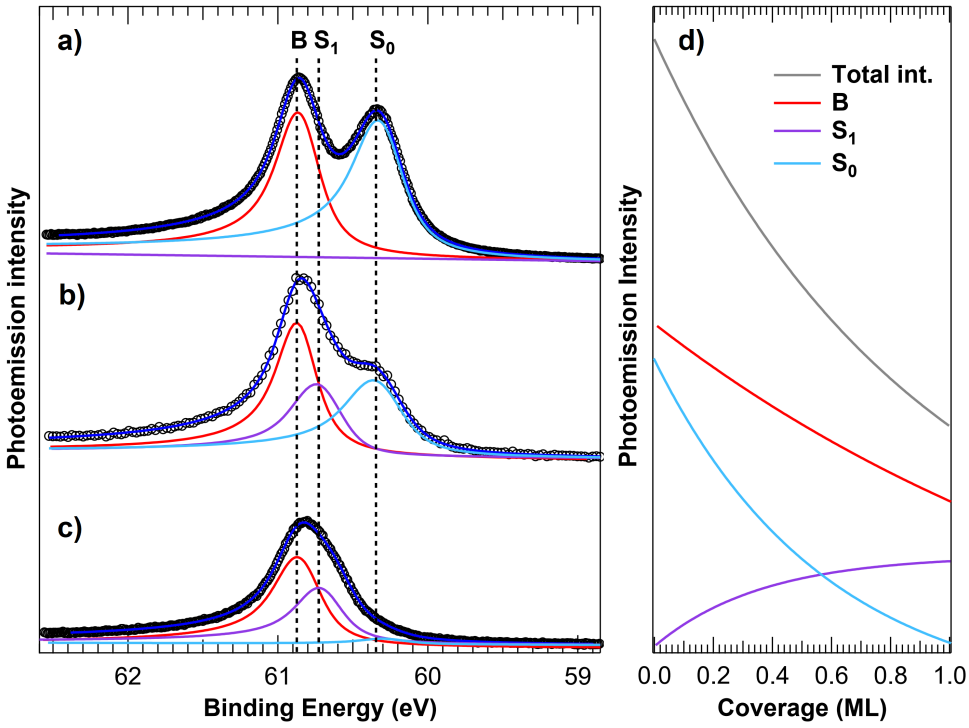

Figure 2.5: Example of XPS data acquired for the determination of the coverage. a) Ir $4f_{7/2}$ spectrum acquired at 200 eV photon energy on clean Ir (111); b) Ir $4f_{7/2}$ acquired during deposition and c) after the complete suppression of the S_0 component. d) Calculated intensity of each spectroscopic component as a function of the coverage.

of the Ir surface atoms and, in the case of Ti, Fe and Co on Ir (111) gives rise to a second surface component (S_1 in figure 2.5b) generated by Ir atoms bounded with the adatoms.

Observing through high resolution XPS the evolution of the photoemission Ir $4f_{7/2}$ spectrum is therefore possible to retrieve the deposition rate.

For small amount of deposited material we can assume the presence of isolated adatoms on the surface. In this case the S_0 signal I would decrease linearly with the coverage Θ with the following relation

$$\frac{I_{S_0}(\Theta)}{I_{S_0}(0)} = n\Theta$$

where $I_{S_0}(0)$ is the initial intensity of S_0 and n is the number of atoms of the substrate interacting with a single adatom. In case of epitaxial growth, depending on the adsorption site, it is possible that the complete suppression of the S_0 is achieved by depositing a fraction of a monolayer. To obtain the missing part of information is then possible to proceed in different ways. It

is possible to directly compare the photoemission signal from the adatoms to the initial value of S_0 and retrieve the surface density of adatoms from eq.2.2. Alternatively, the screening effect on the total photoemission intensity I from the substrate can be considered, within the relation

$$I(\Theta) = I_0 \cdot e^{-z/\lambda} \tag{2.3}$$

where z is the thickness of the adlayer and λ the inelastic mean free path of the photoelectrons in the deposited material.

These considerations, particularly the latter, are valid assuming a layer-by-layer growth, so the discussed calculation are reliable only once the growth mechanisms are known. Moreover, photoelectron diffraction effects could affect the intensity measurement. Therefore, a reliable coverage evaluation can be obtained by calculating the same quantity by different methods in a redundant way.

2.6 Experimental facilities

Experiments were mainly performed at the Elettra-Sincrotrone Trieste, at the Surface Science Laboratory (SSL) and at the SuperESCA beamline of Elettra. Experimental measurements on the cobalt nanoarchitectures (Chapter 6) were performed at the Materials Science beamline of Elettra, while all Scanning Tunneling Microscopy measurements shown in this thesis were performed at the CoSMoS end station of SuperESCA. In the following I will focus on the first two experimental facilities.

2.6.1 Surface Science Laboratory

In the SSL laboratory was performed the largest part of the preliminary experiments on the nanoarchitectures described in this thesis. The SSL experimental chamber consists of a UHV system having a base pressure of the order of 1×10^{-10} mbar. A fast transfer system is implemented in order to easily transfer samples without breaking the vacuum. The vacuum chamber is cylindrically shaped, vertically oriented, covered by a rotating flange. Instruments are mounted on the side wall of the chamber. A motorized manipulator with five degrees of freedom is used to support the sample and it is installed eccentrically on the top rotating flange. This configuration allows to move the sample in front of the instruments. Metallic samples are spot-welded on a tantalum rod which provide electric and thermal contact. The cooling of the sample is possible through a liquid nitrogen system implemented on the manipulator, while

sample heating is performed by irradiation or electron bombardment by means of tungsten filaments mounted behind the sample. The sample temperature is measured by a thermocouple directly spot-welded on its back side.

For sample preparation, an ion sputter gun is installed on the chamber. Gas treatments can be performed by delivering pure gasses inside the chamber from a separated gas line equipped with a series of leak-valves. A quadrupole residual gas analyser can be used to investigate the composition of the gas inside the UHV chamber. Different kinds of evaporators can be mounted in the experimental chamber through dedicated flanges. UHV gate-valves allow to install and remove evaporators without venting the chamber.

X-ray photoelectron spectroscopy can be performed using a Mg K_α or a monochromatised Al K_α X-ray source and a CHA equipped with five independent channeltrons. A LEED system is installed along with a Spot Profile Analysis - LEED; both of them are controlled by a LabVIEW software that allows the acquisition of high quality diffraction images. Dedicated LabWIEW software was also implemented for XPS acquisition, manipulator and rotating flange control, chamber pressure and sample temperature monitoring.

In the SSL laboratory, in addition to the UHV chamber for surface science experiments, is also installed the size selected nanocluster source described in chapter 7.

2.6.2 SuperESCA beamline

SuperESCA was the first beamline operating at Elettra, the third-generation synchrotron radiation facility [11]. Elettra is optimized for the production of VUV and soft X-ray radiation. The SuperESCA is designed to achieve high performance in core level spectroscopy in terms of energy resolution and signal to noise ratio.

Radiation is produced by 2.0 or 2.4 GeV electrons accumulated in the storage ring passing through an undulator. The radiation produced has a spectrum consisting of several harmonics of a fundamental wavelength that depends on the magnetic field inside the undulator. The full width half maximum of the fundamental harmonic is few eV. A grating monochromator is used to further narrow the spectral distribution. A maximum resolving power of 1000 can be achieved for photon energy of few hundreds eV, which is the typical energy employed for core level XPS. The photon flux is of the order of 10^{12} photons/s and allows fast XPS measurements.

The beamline end station consists of two experimental chambers, one ded-

icated to sample preparation, equipped with a sputter gun and connected to a gas line, the other to synchrotron light measurements. The same manipulator, similar to the one in use at SSL, is employed for the sample handling in both UHV chambers. On the measurement chamber a LEED system is installed along with a PHOIBOS hemispherical electron energy analyser from SPECS GmbH. The 150 mm CHA is implemented with a 2D microchannel plate/delay-line detector capable of 500000 counts/s which can be used to acquire single shot photoemission spectra or to perform high resolution energy scan. The overall maximum energy resolution of the SuperESCA XPS system is better than 50 meV.

High energy resolution and time resolved XPS make SuperESCA particularly suitable for the real-time investigation of chemical reactions on surfaces and the epitaxial growth of thin films and 2D materials.

2.7 Density Functional Theory calculations

To improve the knowledge on some of the nanoarchitectures we have grown, the experimental data were complemented by Density Functional Theory (DFT) calculations performed by the collaborating group headed by Prof. Dario Alfè from University College London. DFT calculation were performed with the aim of simulating some of the graphene-based interfaces and calculating their electronic Partial Density Of States (PDOS).

The density functional theory has been proposed back in 1965 like an "approximation method for treating an inhomogeneous system of interacting electron" [12] and nowadays is one of the most powerful tools in computational matter physics. The DFT calculations on our interfaces were performed using the Vienna Ab-initio Simulation Package (VASP) [13] which allows to use post-DFT corrections such as hybrid functionals.

The initial atomic supercells presented in this thesis were designed on the basis of the information obtained in the experiments. In the first stage of the calculation the atomic position were retrieved for the minimum energy configuration of the system. To this end, the structural parameters were relaxed using the rev-vdw-DF2 functional until the residual force was less than a threshold value of the order of 1×10^{-2} eV/Å. Plane-wave basis set was used including all plane waves up to a kinetic energy of 400 eV, and the core electrons were treated with the Projector Augmented Wave method [14]. PDOS were subsequently calculated on the the basis of the calculated structural parameters. Although the geometry of the systems could be accurately described by the rev-vdw-DF2

functional, their electronic structures required the use of a hybrid functional. PDOS was therefore calculated by using the HSE06 hybrid functional with a 3×3 k-point grid or considering only the Γ point depending on the number of atoms in the supercells, which was equal to 1397 for the largest one.

References

[1] Woodruff, D. *Modern Techniques of Surface Science*; Cambridge University Press, 2016.

[2] Hüfner, S. *Photoelectron spectroscopy: principles and applications*; Springer Science & Business Media, 2013.

[3] Nordling, C.; Sokolowski, E.; Siegbahn, K. Precision method for obtaining absolute values of atomic binding energies. *Physical Review* **105**, 1676 (1957).

[4] Siegbahn, K. Electron spectroscopy for atoms, molecules, and condensed matter. *Science* **217**, 111 (1982).

[5] Doniach, S.; Šunjić, M. Many-electron singularity in X-ray photoemission and X-ray line spectra from metals. *Journal of Physics C: Solid State Physics* **3**, 285 (1970).

[6] Davisson, C.; Germer, L. H. Diffraction of electrons by a crystal of nickel. *Physical review* **30**, 705 (1927).

[7] Binnig, G.; Rohrer, H.; Gerber, C.; Weibel, E. Tunneling through a controllable vacuum gap. *Applied Physics Letters* **40**, 178 (1982).

[8] Stroscio, J. A.; Kaiser, W. J. *Scanning tunneling microscopy*; Academic Press, 1993; Vol. 27.

[9] Lüth, H. *Solid surfaces, interfaces and thin films*; Springer, 2001; Vol. 4.

[10] Mercer, J.; Finetti, P.; Leibsle, F.; McGrath, R.; Dhanak, V.; Baraldi, A.; Prince, K.; Rosei, R. STM and SPA-LEED studies of O-induced structures on Rh (100) surfaces. *Surface Science* **352**, 173 (1996).

[11] Abrami, A. et al. Super ESCA: First beamline operating at ELETTRA. *Review of Scientific Instruments* **66**, 1618 (1995).

[12] Kohn, W.; Sham, L. J. Self-consistent equations including exchange and correlation effects. *Physical Review* **140**, A1133 (1965).

[13] Kresse, G.; Furthmüller, J. Efficient iterative schemes for ab initio total-energy calculations using a plane-wave basis set. *Physical Review B* **54**, 11169 (1996).

[14] Blöchl, P. E. Projector augmented-wave method. *Physical Review B* **50**, 17953 (1994).

Chapter 3

Graphene-based substrates

Graphene is the material on which all the interfaces we grew, characterized and tested are based on. In this chapter I will give a brief description of its fundamental properties and of the experimental procedures used for its growth, along with a description of the intercalation methods we used for the preparation of our nanoarchitectures.

3.1 General properties

Graphene can be defined as a one-atom thick layer of sp^2-hybridised carbon atoms, arranged in a honeycomb crystal lattice, with two atoms per unit cell. Each atom is bonded to its nearest neighbours in a threefold geometry; for this reason the whole honeycomb lattice can be interpreted as two interpenetrating triangular lattices rotated by 30° (A and B in figure 3.1a).

Three σ bonds are formed at each atom by the sp^2-hybrid orbitals on the graphene plane. The unique mechanical properties of graphene derive from the energy of these σ bonds: to date, graphene is the strongest known material per unit of weight [1, 2].

The non-hybridized p orbital, perpendicular to the bond plane, is responsible for the formation of the π and π^* bands and gives rise to the peculiar graphene electronic structure [3–5] (figure 3.1b).

Regarding its electronic properties, graphene is famous for being a material in which charge carriers move as relativistic massless particles, i.e. with a linear energy-momentum dispersion relation. This feature was firstly calculated by Wallace in 1947 by applying the tight binding approach for the description of the graphite band structure [7]. He defined graphite as "*a semi-conductor*

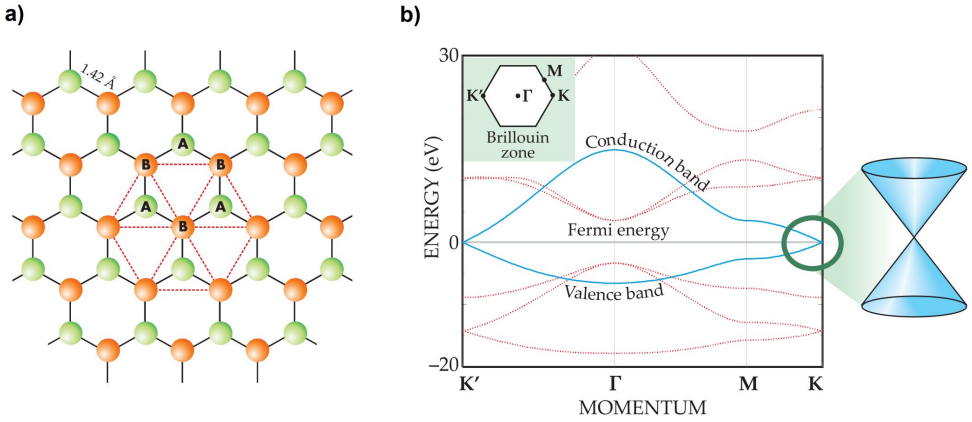

Figure 3.1: a) The honeycomb lattice of graphene, formed by two interpenetrating triangular sublattices of C atoms (A and B), shown in red and green. b) Electronic band structure of graphene. The π and π^* bands (blue curves in the plot) form conical valleys that touch at two of the high-symmetry points, conventionally labeled K and K', in the Brillouin zone. Near these points the energy varies linearly with the magnitude of momentum measured from the Brillouin-zone corners. Image from [6].

with zero activation energy", after having calculated that the cosine-like energy bands, arising from the two triangular sublattices, intersect at energy $E = E_F$ at the corner of the first Brillouin zone. These intersections give rise to the conical shaped band features, called *Dirac cones*, placed at the **K** and -**K** points of the Brillouin zone, consequently named Dirac points.

Charge carriers with energies differing from E_F by less than 1 eV have zero effective mass and mimic relativistic particles with an effective speed of light $v_F \simeq 10^6$ m/s. Although there are no proper relativistic significant effects regarding electrons and holes moving around carbon atoms, the honeycomb periodic potential gives rise to quasiparticles that are more easily and directly described by means of the Dirac equation rather than the Schrödinger equation. Within this theoretical framework quasiparticles are indexed on the basis of the two triangular sublattices A and B from which they arise. Due to the similarities with the Dirac formalism, this index was named pseudospin.

The quantum electro-dynamical approach for the description of Gr electronic properties allowed to predict and interpret a series of effects related to the pseudospin of the charge carriers. Among the most striking observations there are, for example, the quantum hall effect and the presence of a non-zero Berry's phase in the electron wave function [8], the high-probability tunnelling phenomenon described by the so called Klein's paradox [9], the finite value for the electrical conductivity in the limit of zero temperature and zero charge

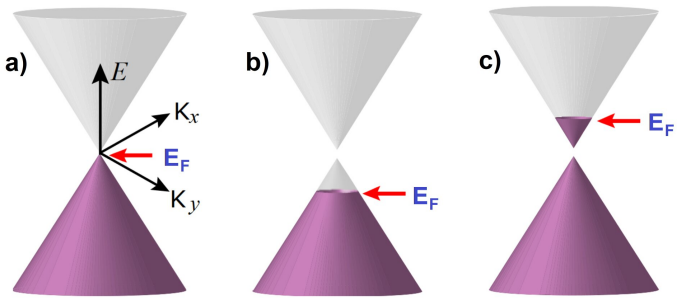

Figure 3.2: Dirac cones of the graphene electronic structure as a function of the doping state. a) Ideal free-standing condition; b) p-doping; c) n-doping.

carrier density [10], the sub Poissonian shot noise generated in electric current flowing at zero temperature through defect-free graphene [11].

In order to experimentally observe this variety of unique phenomena, it is necessary to synthesize what is called a free-standing graphene, i.e. an isolated graphene layer, ideally not interacting with any other material. Fundamental studies were performed in similar condition, mostly at the beginning of the graphene era, to investigate the stability of the Gr 2D structure [12, 13]. On the other hand, the investigation of the practically exploitable electronic properties and the exploration of the technical possibility offered by supported graphene rapidly gained importance, opening an area of research dedicated to the modification of the Gr electronic structure.

The electronic doping of graphene represents one of the most studied phenomena related to the weak interaction of Gr with other materials (e.g. adatoms or solid supports) [14–18].

The term "doping" in graphene refers to the condition where the electronic band structure rigidly shifts respect to the Fermi level and the Dirac point is displaced either above (p-doping) or below E_F (n-doping). For the case of low-interacting supported graphene[1], this condition is substantially unavoidable and it is the consequence of a charge transfer between the two materials. In turn, this charge transfer can be naively attributed to the difference in work function between Gr and its support, but it is also strongly affected by the interface dipole arising from the direct short-range substrate-graphene interaction. DFT calculations proved to be an efficient

[1]The low interaction requirement is related to the fact that highly interacting substrates can generate major modifications in the electronic structure, as observed for example in the case of hexagonal boron nitride-supported graphene, where a gap opens at the Dirac point [19].

tool to predict quantitatively the doping state of graphene on specific surfaces [20, 21]. In this thesis, doping will have an important role in the discussion of our nanostructured interfaces.

3.2 Growth techniques

Along with the fundamental interest for this unique material, the attention about the possible technological applications kept growing until now. In this perspective, the extensive production of high-quality graphene is of paramount importance and the development of efficient and scalable method still represents a crucial research topic.

Since the first isolation of graphene, performed by mechanical exfoliation [22], several production strategies have been introduced. Many of them are based on a top-down approach starting from high purity graphite samples that undergo chemical, electrochemical or mechanical exfoliation [23–26]. The results obtained with these techniques, despite being generally efficient and often scalable, do not provide the high degree of reproducibility offered by some bottom-up synthetic methods and often lead to the presence of impurities and defects in graphene.

Among the bottom-up approaches, the direct graphene growth on solid surfaces is one of the most effective strategies. During the years, several methods have been developed to guarantee good structural and chemical properties, on many different substrates [28]. An important aspect to consider is that the growth methods are strictly related to the specific substrate.
Bottom-up graphene growth generally consists in the deposition of a layer of carbon atoms on the selected surface and the promotion of the C–C bond formation through the sp^2 hybrid orbitals, usually obtained by heating the substrate. There are different ways to deliver carbon to the substrate surface: (i) by depositing carbon atoms or small carbon aggregates (dimers, trimers) obtained from sublimation of high purity graphite, (ii) by segregation of bulk-dissolved carbon to the surface, (ii) by surface decomposition of carbon-containing molecules.

Furthermore, the particular case in which carbon is already part of the substrate has to be considered, with the SiC case being particularly significant. Hystorically, for electronic applications, the growth of graphene on semiconducting or insulating materials have been largely explored and the direct growth of graphene on SiC became a reference. The method consists in heating a SiC

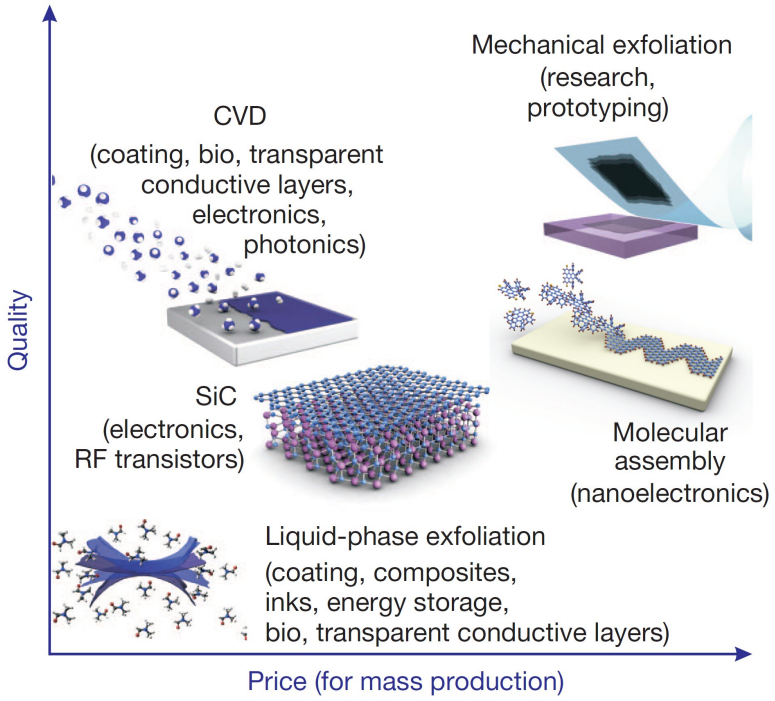

Figure 3.3: A pictorial overview of the variety of Gr growth methods associated with their application fields, reported by Novoselov *et al.* [27].

wafer to let the silicon atoms sublimate. During a specific thermal treatment the carbon atoms on the surface bind together forming the graphene lattice above a reconstructed interfacial carbon layer. The quality of the so produced graphene is very high in terms of point defects, but the possibility of multiple layer formation is a considerable disadvantage, along with the fact that bulk SiC substrates present limitations relatively to costs, sizes, and preparation issues. Moreover, graphene on SiC results to be n-doped due to its interaction with the interfacial carbon layer [29].

In this respect, Gr growth on metal substrates is generally easier, less expensive and more versatile. Graphene layers on metal surfaces can be prepared both by segregation of C from the bulk and by surface decomposition [30]. While the first method is often characterized by the possibility to obtain multilayer graphene, the second one is generally more easily controllable from this point of view. Anyway, the applicability of one method or the other is strictly connected the morphology of the specific surfaces and their interaction with carbon atoms [21].

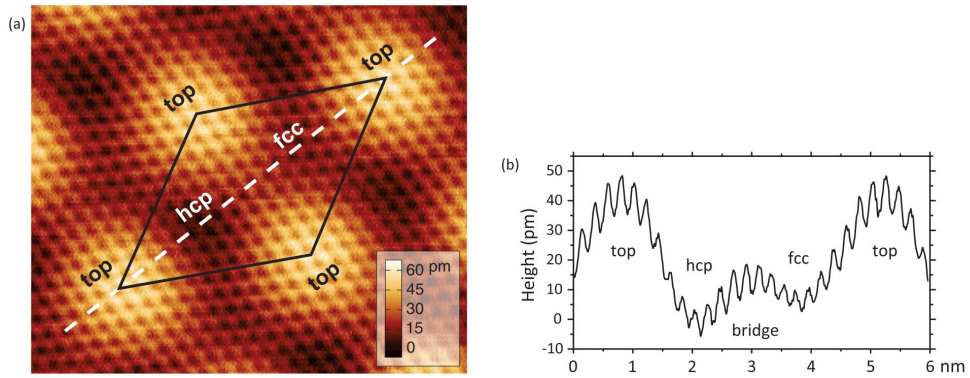

Figure 3.4: a) STM image with atomic resolution of Gr/Ir (111); b) line profile along the major diagonal of the moiré cell. The dependence of the Gr height on the adsorption site is appreciable. Image reported from [32].

Graphene on Ir (111). Due to the interaction with the substrate, graphene can undergo considerable modification of its properties. In this respect, Gr/Ir (111) is considered as the prime example of graphene weakly interacting with the substrate. Graphene grown on this particular surface has structural, electronic and chemical properties that are remarkably close to the ones of free-standing graphene. For this reason we adopted this interface as foundation of our nanoarchitectures.

The technique we used to grow graphene is a common bottom-up method: the Chemical Vapour Deposition (CVD) of ethylene. A well established procedure performed in UHV conditions consists in the exposure of the clean metallic surface to ethylene combined with a thermal treatment [31]. Ir (111) is efficiently covered with C_2H_4 by exposing it to the gas at a partial pressure of $5{\cdot}10^{-8}$ mbar for 2 minutes while keeping the sample at 500 K. An annealing up to 1400 K is performed on the ethylene-covered crystal to dehydrogenate C_2H_4 molecules and brake-up the C=C bonds. The aggregation of the carbon monomers on Ir (111) takes place at high temperature and during the cooling, producing the graphene honeycomb lattice.

To obtain a complete graphene layer the procedure has to be repeated, since the high temperature annealing causes a partial desorption of molecular fragments of ethylene and the formation of isolated graphene flakes. The ethylene deposited at room temperature on already formed graphene completely desorbs during the annealing and does not participate to the formation of any second graphene layer. The growth process in this case is therefore considered to be self-limiting.

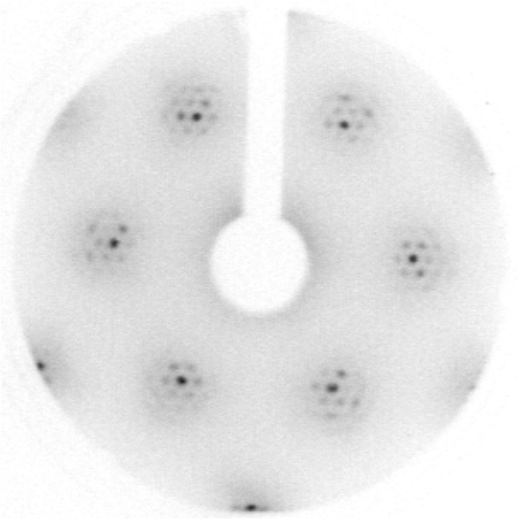

Figure 3.5: Low Energy Electron Diffraction image we acquired on Gr/Ir (111) using 145 eV electron energy.

The structure of Gr/Ir (111) has been widely investigated [33]. From the morphological point of view, the most important characteristic is the presence of a moiré superlattice. The origin of this superlattice is related to the mismatch between the Gr lattice parameter (2.46 Å) and the substrate's one (2.74 Å for Ir(111)). With a strain of less than 1%, a 10×10 graphene supercell superimposes on a 9×9 Ir (111) supercell forming the characteristic moiré pattern.

The moiré superlattice causes the C atomic positions to coincide with different crystal sites of the substrate (top, hcp, fcc regions) and therefore to interact differently with the Ir atoms. A consequence of this periodically modulated interaction is a periodic variation of the Gr–substrate distance, which creates a small corrugation of the graphene layer with the same periodicity of the moiré lattice. In figure 3.4 an STM image of the moiré superstructure on Ir (111) is reported.

To inspect the quality of graphene regarding the long-range order, we perform low energy electron diffraction measurements after each preparation. In figure 3.5 a LEED image is reported. The presence of large Gr domains is paramount to the majority of our experiments and it can be assessed by analysing the intensity line profiles of the diffraction images. It is known indeed that Gr can grow on Ir (111) along several different orientations with respect to the main crystallographic directions of the substrate [34]. Rotational domains cause a stretch of the diffraction spots along the circumference centred in the

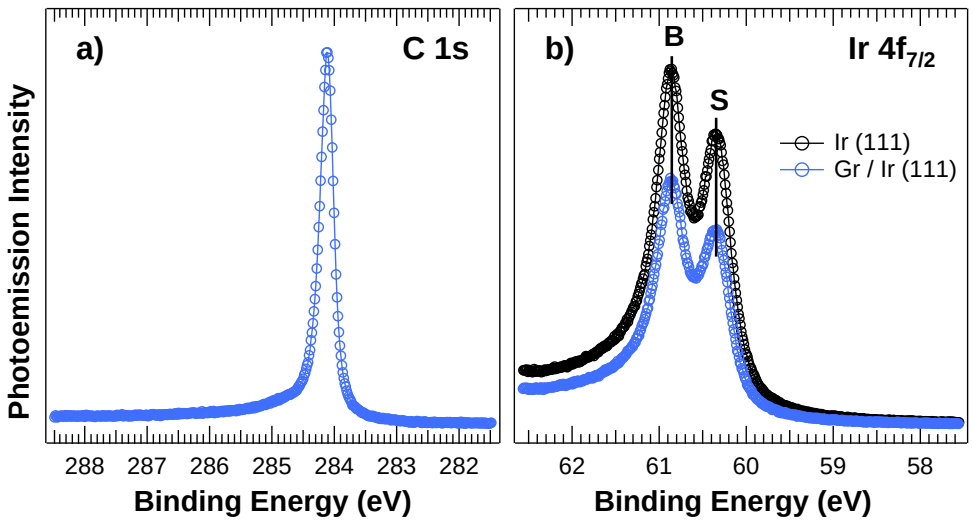

Figure 3.6: High resolution photoemission spectra of a) C $1s$, acquired at 400 eV photon energy and b) Ir $4f_{7/2}$, acquired at 200 eV photon energy, before and after the Gr growth. Labels B and S are referred to the bulk and surface Ir $4f_{7/2}$ components at 60.89 and 60.34 eV respectively.

zero diffraction order. The round shape of the Gr spots we observed can be therefore interpreted as the presence of rotational domains larger than the instrumental transfer width (in our LEED is about 100 Å).

On the other hand, the chemical features of graphene and Ir are investigated through HR-XPS, performed on the C $1s$ and Ir $4f_{7/2}$; an example of the spectra we acquired after a graphene preparation is reported in figure 3.6.

In the C $1s$ spectrum, a single sharp photoemission component is found at a binding energy of 284.11 eV. The FWHM of this photoemission component provides information about the quality of the graphene layer. A value below 300 meV for this quantity suggests that graphene is characterized by a low degree of inhomogeneities and a low density of defects [35].

Important information can be obtained also from the Ir $4f_{7/2}$ spectrum. The presence of graphene reduces the total photoemission intensity of about 30%, but leaves almost unchanged the Ir $4f_{7/2}$ line shape, the surface core level shift and the relative spectral weights of the bulk and surface component. This effect is due to the particularly weak interaction between Ir (111) and Gr, which leaves the chemical environment of the Ir surface atoms almost unchanged.

3.3 Intercalation processes

Just few years after the first graphene isolation, Novoselov predicted the possibility of engineering the band-structure of graphene by supporting it on different substrates [36]. This goal was indeed pursued over the years, in parallel with the development of Gr growth techniques. In this perspective, intercalation was introduced as a way to bypass the impossibility to directly grow or transfer high quality graphene on particular substrates.

This procedure is based on the exposure of the graphene-covered surface to a flux of metal atoms or gas molecules, generally at a few hundreds K above room temperature, with the aim of growing a new layer below graphene and preserving the integrity of the honeycomb lattice.

This strategy was early introduced as a method to obtain a graphene with quasi free-standing properties. Indeed, the intercalation of Au atoms was exploited, for example, to restore the linear dispersion of the π bands at the Dirac point for graphene grown by CVD on Ni (111) [37]: Au atoms quench the chemical interaction between Gr and Ni (111) restoring the system towards the condition of free-standing graphene. A similar result was obtained through the intercalation of hydrogen atoms at the Gr/SiC interface, where H atoms at the interface are involved in covalent bonds with the substrate and supress the chemical interaction with graphene [38].

In a different perspective the intercalation was also employed in graphene functionalization for technological application. A p-doped graphene can be obtained for example on Ir (111) by intercalation of oxygen [39]. The tuning of the doping level of graphene is of great interest in the field of electronic devices and it was successfully achieved through the creation of an ultra-thin silicon oxide layer at the Gr/Ir (111) interface [40].

Nobel- [41], alkali- [42] and transition-metals [43] as well as metal oxides [44, 45] has been employed to investigate the consequences on graphene of a modified substrate. Intercalation of light atoms and molecules, then, revealed the possibility to perform chemical reaction below graphene with a particularly high reactivity and selectivity. These enhancement effects are referred to as "catalysis under cover".

Reactive processes involving O_2 and NO_2 were observed, for example, by Sutter *et al.* [46]; their work suggests that graphene can be used to selectively confine small molecules at the interface with the support and that it may control the orientation of the intercalated molecules. These effects were observed to be strictly dependent on the specific interface and chemical reaction. A

computational study by Ferrighi *et al.* [47] for example, showed that at the Gr/anatase-TiO_2 interface the O_2 dissociation is boosted, while a similar effect is not appreciated for H_2O. Moreover, the presence of a specific dopant in graphene is capable of producing major modification in the chemical reaction mechanisms. Such results suggest that the theoretical and experimental exploration of a variety of interfaces is a promising way to find high performance catalysts, whose properties are not intuitively predictable.

Going back to the general atomic intercalation process, a brief discussion is needed about its detailed mechanism. Intercalation has been investigated in detail since the beginning of its application, but it is not fully explained yet, although it is known that the specific mechanism depends on the intercalating species.

It is also known that the intercalation of atoms below graphene starts from the graphene defects [21]. The intercalation across the defect-free graphene through a distortion of the hexagons is indeed energetically prohibited, at least for metal atoms, so the presence of a defect appears to be necessary. The diffusion through the edges of the graphene flakes are one of the most accepted intercalation mechanisms [48–50], along with the penetration through the domain boundaries and the cracks formed on Gr wrinkles [42, 51, 52]. Point defects were also took into consideration for being active sites [53, 54]. Moreover, the possibility of a reactive passage by defect formation by the same intercalating species has been postulated [55, 56].

In these processes the temperature of the substrate plays an important role, since the higher is the thermal diffusion of atoms above graphene, the higher is the probability for them to reach a suitable site for intercalation and to overcome the energy barrier to penetrate at the interface. Moreover, some mechanisms, as the reactive defect formation, are characterized also by energy barriers that have to be overcome.

Despite the incomplete theoretical interpretation of the process, effective procedures have been established empirically for a large variety of intercalating compound and substrates.

Methods for metal oxide intercalation. In our experiments we intercalated iron-, cobalt- and titanium-oxide. The process was always composed of two steps, performing the metal intercalation first, and then the oxidation.

For the case of titanium and cobalt, the procedure we used for the metal intercalation was the same: the metal was evaporated from a high purity filament by resistive heating while the sample was kept at 670 K. This temperature

was found to be few tens of degrees higher than the minimum temperature under which, using the same deposition rate, the intercalation was not complete. We used the lowest possible value for intercalation temperature to reduce the probability of alloy formation with the substrate and to reduce possible graphene damages due to the presence of reactive residual gasses inside the UHV chamber.

To intercalate iron we had to adopt a different strategy, proved to be efficient for Gr/Ir (111) [57] and also for Gr/Ni(111) [58], consisting in the Fe deposition at room temperature above graphene followed by annealing at 570 K to intercalate it. The discrepancy between the intercalation methods we used for Fe with respect to Ti and Co has to be attributed to the different interaction of the adatoms with graphene, that determines their surface diffusion above and below graphene as well as the intercalation mechanism itself which, unfortunately, remains unclear at the moment.

The amount of intercalated metal was selected to obtain the minimum coverage sufficient for the creation of a complete oxide layer below graphene and the complete substitution of the Gr/Ir (111) interface.

To monitor the intercalation process we performed time-resolved XPS measurements. During TR-XPS the photon energy cannot be varied, so it is necessary to make a selection regarding the core levels to observe. Since our focus is on graphene, and a modification of the C 1*s* spectrum is expected after intercalation, we measured this spectral component at 400 eV photon energy. In a second set of measurements, we exploited the same photon energy to acquire Ir $4f_{7/2}$ spectra, to observe the evolution of both Gr and Ir (111) at the same time. In agreement with results reported in literature, during the interaction of all the three metals we observed the appearance of a C 1*s* component at higher binding energies with respect to Gr/Ir (111) and the contemporary depletion of the component at BE = 284.11 eV. We exploited this photoemission observation to control the amount of the intercalated material. The complete vanishing of the Gr/Ir (111) C 1*s* component was intended as the completion of the intercalated metallic layer. On the basis of the HR-XPS measurements the effective coverage was then calculated.

The evolution of the Ir $4f_{7/2}$ spectrum was monitored to have a confirmation of the effective intercalation. The intensity of the surface photoemission component (BE = 60.34 eV) is reduced with respect to the bulk one (BE = 60.89 eV) by the interaction of the surface Ir atoms with the intercalated metal. The strong variation of the intensity ratio between the two components suggests therefore the presence of an intercalated species.

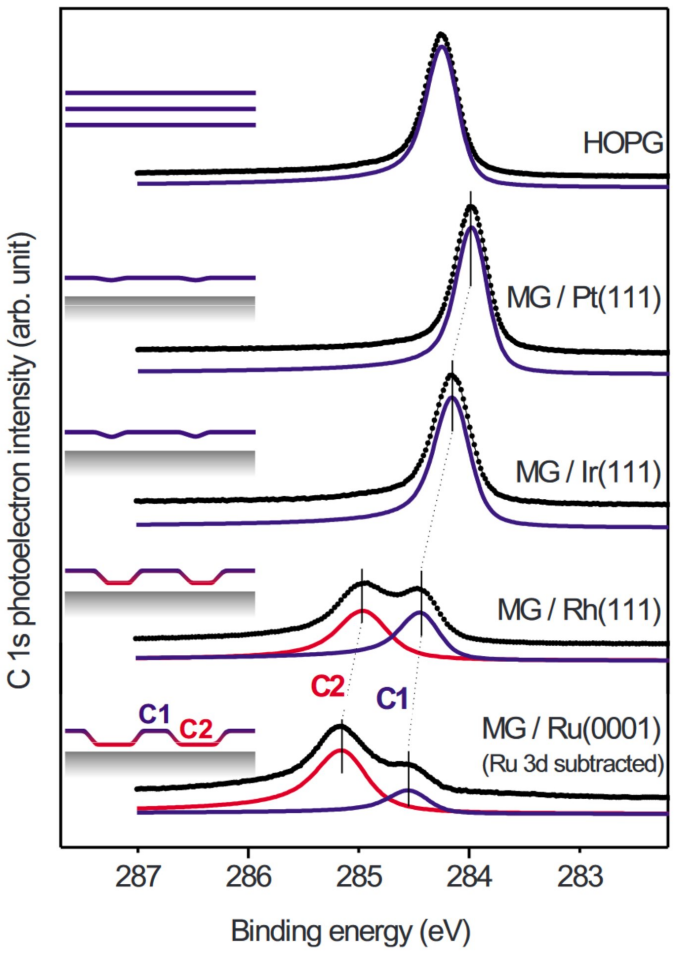

Figure 3.7: C 1*s* photoemission spectra of graphene on representative solid surfaces, compared with the spectrum acquired on highly oriented pyrolytic graphite (HOPG). For the case of highly interacting substrates the components C1 and C2, related to the corrugation, can be distinguished. Image from [59].

A series of electronic and structural modification can be further assessed by HR-XPS, in particular by the analysis of the most important C 1*s* spectral features. The doping state of graphene can be qualitatively evaluated measuring the C 1*s* binding energy. The shift in binding energy of the Dirac cones relatively to E_F is accompained by a shift of the core levels, with a different absolute value, but in the same direction. The reference for this shift is the C 1*s* binding energy measured for graphite. An example of different doping states of graphene measured by XPS is reported in figure 3.7 [59]. Highly oriented pyrolytic graphite is reported as a reference system; Gr/Ir (111) results to be slightly p-doped, while Gr/Pt (111), another example of low interacting

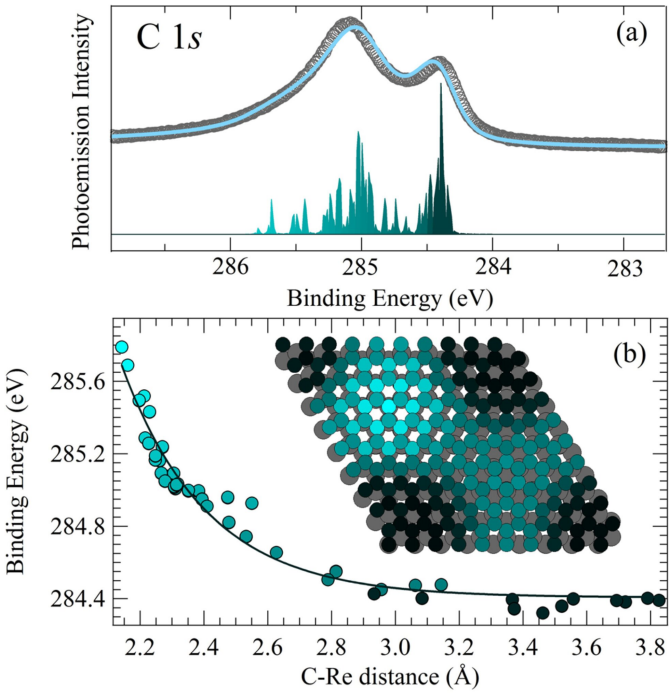

Figure 3.8: a) Esperimental C 1*s* spectrum measured for Gr/Re (0001) (empty circles) together with the simulated spectrum (solid line) and the calculated spectral distribution originated by the 200 C atoms of the moiré supercell; b) Binding energies of non-equivalent C atoms on the C-Re distance. The color scale in the model reflects the binding energies of the different C 1*s* components. Image from [60].

interface, is characterized by a more intense p-doping. In the same picture are reported other interesting highly interacting systems as Gr/Rh (111) and Gr/Ru (0001). Both these surfaces are characterized by the presence of a moiré superlattice; from the strong interaction of these two metals with graphene, the presence of different C species arises, related to the adsorption sites on the metal surface, namely top, hcp and fcc. The distance of the C atoms from the metal surface is determined by these adsorption configurations and in the case of strongly interacting surfaces the differences in this distance are enhanced, i.e. the moiré corrugation is enhanced, with respect to the one observed on a weakly interacting surface. For both Gr/Rh (111) and Gr/Ru (0001) the C atoms on the hills (top sites) and valleys (fcc and hcp sites) of the corrugation generate two different photoemission components C1 and C2, respectively. Moreover, from their spectral weights it is possible to determine the degree of interaction, which is higher in the case of a more intense component at high binding energy. It has to be remarked that in such condition the rigorous definition of doping

state is no longer fully applicable, due to a chemical interaction between the p orbitals of C atoms and the d orbitals of the transition metal atoms that affect significantly the electronic structure of graphene. In addition, C1 and C2 have to be considered not as two photoemission components, but as an energy distribution generated by all the C atoms in the moiré supercell. A clear example for this distribution was reported by Miniussi *et al.* [60] for to the C $1s$ spectrum of Gr/Re (0001). In figure 3.8a the experimental C $1s$ spectrum is shown in comparison with the calculated spectral distribution. Analogous calculation reposted by Presel *et al.* show that the same relation between C $1s$ spectral distribution and moiré corrugation can be exploited in the characterization of a series of interfaces obtained by metal intercalation [43]. Within this thesis, we will discuss the experimental results we obtained for Ti, Fe and Co intercalated at the Gr/Ir (111) interface, which represents the first step for the preparation of our nanoarchitectures.

References

[1] Akinwande, D.; Brennan, C. J.; Bunch, J. S.; Egberts, P.; Felts, J. R.; Gao, H.; Huang, R.; Kim, J.-S.; Li, T.; Li, Y. A review on mechanics and mechanical properties of 2D materials—Graphene and beyond. *Extreme Mechanics Letters* **13**, 42 (2017).

[2] Lee, C.; Wei, X.; Kysar, J. W.; Hone, J. Measurement of the elastic properties and intrinsic strength of monolayer graphene. *Science* **321**, 385 (2008).

[3] Geim, A. K.; Novoselov, K. S. The rise of graphene. *Nature Materials* **6**, 720 (2007).

[4] Neto, A. C.; Guinea, F.; Peres, N. M.; Novoselov, K. S.; Geim, A. K. The electronic properties of graphene. *Reviews of Modern Physics* **81**, 109 (2009).

[5] Sarma, S. D.; Adam, S.; Hwang, E.; Rossi, E. Electronic transport in two–dimensional graphene. *Reviews of Modern Physics* **83**, 407 (2011).

[6] Geim, A. K.; MacDonald, A. H. Graphene: exploring carbon flatland. *Physics Today* **60**, (2007).

[7] Wallace, P. R. The band theory of graphite. *Physical Review* **71**, 622 (1947).

[8] Zhang, Y.; Tan, Y.-W.; Stormer, H. L.; Kim, P. Experimental observation of the quantum Hall effect and Berry's phase in graphene. *Nature* **438**, 201 (2005).

[9] Katsnelson, M.; Novoselov, K.; Geim, A. Chiral tunnelling and the Klein paradox in graphene. *Nature Physics* **2**, 620 (2006).

[10] Katsnelson, M. Zitterbewegung, chirality, and minimal conductivity in graphene. *The European Physical Journal B-Condensed Matter and Complex Systems* **51**, 157 (2006).

[11] Tworzydło, J.; Trauzettel, B.; Titov, M.; Rycerz, A.; Beenakker, C. W. Sub-Poissonian shot noise in graphene. *Physical Review Letters* **96**, 246802 (2006).

[12] Meyer, J. C.; Geim, A. K.; Katsnelson, M. I.; Novoselov, K. S.; Booth, T. J.; Roth, S. The structure of suspended graphene sheets. *Nature* **446**, 60 (2007).

[13] Novoselov, K.; Jiang, D.; Schedin, F.; Booth, T.; Khotkevich, V.; Morozov, S.; Geim, A. Two-dimensional atomic crystals. *Proceedings of the National Academy of Sciences* **102**, 10451 (2005).

[14] Dahal, A.; Addou, R.; Coy-Diaz, H.; Lallo, J.; Batzill, M. Charge doping of graphene in metal/graphene/dielectric sandwich structures evaluated by C-1s core level photoemission spectroscopy. *APL Materials* **1**, 042107 (2013).

[15] Marchini, S.; Günther, S.; Wintterlin, J. Scanning tunneling microscopy of graphene on Ru (0001). *Physical Review B* **76**, 075429 (2007).

[16] Giovannetti, G.; Khomyakov, P.; Brocks, G.; Karpan, V. v.; Van den Brink, J.; Kelly, P. J. Doping graphene with metal contacts. *Physical Review Letters* **101**, 026803 (2008).

[17] Bertoni, G.; Calmels, L.; Altibelli, A.; Serin, V. First-principles calculation of the electronic structure and EELS spectra at the graphene/Ni (111) interface. *Physical Review B* **71**, 075402 (2005).

[18] Uchoa, B.; Lin, C.-Y.; Neto, A. C. Tailoring graphene with metals on top. *Physical Review B* **77**, 035420 (2008).

[19] Giovannetti, G.; Khomyakov, P. A.; Brocks, G.; Kelly, P. J.; Van Den Brink, J. Substrate-induced band gap in graphene on hexagonal boron nitride: Ab initio density functional calculations. *Physical Review B* **76**, 073103 (2007).

[20] Khomyakov, P.; Giovannetti, G.; Rusu, P.; Brocks, G. v.; Van den Brink, J.; Kelly, P. J. First-principles study of the interaction and charge transfer between graphene and metals. *Physical Review B* **79**, 195425 (2009).

[21] Batzill, M. The surface science of graphene: Metal interfaces, CVD synthesis, nanoribbons, chemical modifications, and defects. *Surface Science Reports* **67**, 83 (2012).

[22] Novoselov, K. S.; Geim, A. K.; Morozov, S. V.; Jiang, D.; Zhang, Y.; Dubonos, S. V.; Grigorieva, I. V.; Firsov, A. A. Electric field effect in atomically thin carbon films. *Science* **306**, 666–669 (2004).

[23] Eigler, S.; Enzelberger-Heim, M.; Grimm, S.; Hofmann, P.; Kroener, W.; Geworski, A.; Dotzer, C.; Röckert, M.; Xiao, J.; Papp, C.; *et al.*, Wet chemical synthesis of graphene. *Advanced Materials* **25**, 3583 (2013).

[24] Yang, S.; Lohe, M. R.; Müllen, K.; Feng, X. New-Generation Graphene from Electrochemical Approaches: Production and Applications. *Advanced Materials* **28**, 6213 (2016).

[25] Hernandez, Y.; Nicolosi, V.; Lotya, M.; Blighe, F. M.; Sun, Z.; De, S.; McGovern, I.; Holland, B.; Byrne, M.; Gun'Ko, Y. K.; *et al.*, High-yield production of graphene by liquid-phase exfoliation of graphite. *Nature Nanotechnology* **3**, 563 (2008).

[26] Paton, K. R.; Varrla, E.; Backes, C.; Smith, R. J.; Khan, U.; O'Neill, A.; Boland, C.; Lotya, M.; Istrate, O. M.; King, P.; *et al.*, Scalable production of large quantities of defect-free few-layer graphene by shear exfoliation in liquids. *Nature Materials* **13**, 624 (2014).

[27] Novoselov, K. S.; Fal, V.; Colombo, L.; Gellert, P.; Schwab, M.; Kim, K. A roadmap for graphene. *Nature* **490**, 192 (2012).

[28] Tetlow, H.; de Boer, J. P.; Ford, I.; Vvedensky, D.; Coraux, J.; Kantorovich, L. Growth of epitaxial graphene: Theory and experiment. *Physics Reports* **542**, 195 (2014).

[29] Mishra, N.; Boeckl, J.; Motta, N.; Iacopi, F. Graphene growth on silicon carbide: A review. *Physica Status Solidi (A)* **213**, 2277 (2016).

[30] Wintterlin, J.; Bocquet, M.-L. Graphene on metal surfaces. *Surface Science* **603**, 1841 (2009).

[31] Lizzit, S.; Baraldi, A. High-resolution fast X-ray photoelectron spectroscopy study of ethylene interaction with Ir (111): From chemisorption to dissociation and graphene formation. *Catalysis Today* **154**, 68 (2010).

[32] Hämäläinen, S. K.; Boneschanscher, M. P.; Jacobse, P. H.; Swart, I.; Pussi, K.; Moritz, W.; Lahtinen, J.; Liljeroth, P.; Sainio, J. Structure and local variations of the graphene moiré on Ir (111). *Physical Review B* **88**, 201406 (2013).

[33] Coraux, J.; Plasa, T. N.; Busse, C.; Michely, T. Structure of epitaxial graphene on Ir (111). *New Journal of Physics* **10**, 043033 (2008).

[34] Hattab, H.; N'Diaye, A.; Wall, D.; Jnawali, G.; Coraux, J.; Busse, C.; van Gastel, R.; Poelsema, B.; Michely, T.; Meyer zu Heringdorf, F.-J.; *et al.*, Growth temperature dependent graphene alignment on Ir (111). *Applied Physics Letters* **98**, 141903 (2011).

[35] Lacovig, P.; Pozzo, M.; Alfé, D.; Vilmercati, P.; Baraldi, A.; Lizzit, S. Growth of dome-shaped carbon nanoislands on Ir (111): the intermediate between carbidic clusters and quasi-free-standing graphene. *Physical Review Letters* **103**, 166101 (2009).

[36] Novoselov, K. Graphene: Mind the gap. *Nature Materials* **6**, 720 (2007).

[37] Varykhalov, A.; Sánchez-Barriga, J.; Shikin, A.; Biswas, C.; Vescovo, E.; Rybkin, A.; Marchenko, D.; Rader, O. Electronic and magnetic properties of quasifreestanding graphene on Ni. *Physical Review Letters* **101**, 157601 (2008).

[38] Riedl, C.; Coletti, C.; Iwasaki, T.; Zakharov, A.; Starke, U. Quasi-free-standing epitaxial graphene on SiC obtained by hydrogen intercalation. *Physical Review Letters* **103**, 246804 (2009).

[39] Larciprete, R.; Ulstrup, S.; Lacovig, P.; Dalmiglio, M.; Bianchi, M.; Mazzola, F.; Hornekær, L.; Orlando, F.; Baraldi, A.; Hofmann, P.; Lizzi, S. Oxygen switching of the epitaxial graphene–metal interaction. *ACS Nano* **6**, 9551 (2012).

[40] Larciprete, R.; Lacovig, P.; Orlando, F.; Dalmiglio, M.; Omiciuolo, L.; Baraldi, A.; Lizzit, S. Chemical gating of epitaxial graphene through ultrathin oxide layers. *Nanoscale* **7**, 12650 (2015).

[41] Enderlein, C.; Kim, Y.; Bostwick, A.; Rotenberg, E.; Horn, K. The formation of an energy gap in graphene on ruthenium by controlling the interface. *New Journal of Physics* **12**, 033014 (2010).

[42] Petrović, M.; Rakić, I. Š.; Runte, S.; Busse, C.; Sadowski, J.; Lazić, P.; Pletikosić, I.; Pan, Z.-H.; Milun, M.; Pervan, P. The mechanism of caesium intercalation of graphene. *Nature Communications* **4**, 2772 (2013).

[43] Presel, F.; Jabeen, N.; Pozzo, M.; Curcio, D.; Omiciuolo, L.; Lacovig, P.; Lizzit, S.; Alfe, D.; Baraldi, A. Unravelling the roles of surface chemical

composition and geometry for the graphene–metal interaction through C1s core-level spectroscopy. *Carbon* **93**, 187 (2015).

[44] Lizzit, S.; Larciprete, R.; Lacovig, P.; Dalmiglio, M.; Orlando, F.; Baraldi, A.; Gammelgaard, L.; Barreto, L.; Bianchi, M.; Perkins, E.; Hofmann, P. Transfer-free electrical insulation of epitaxial graphene from its metal substrate. *Nano Letters* **12**, 4503 (2012).

[45] Omiciuolo, L.; Hernández, E. R.; Miniussi, E.; Orlando, F.; Lacovig, P.; Lizzit, S.; Menteş, T. O.; Locatelli, A.; Larciprete, R.; Bianchi, M.; Ulstrup, S.; Hofmann, P.; Alfè, D.; Baraldi, A. Bottom-up approach for the low-cost synthesis of graphene-alumina nanosheet interfaces using bimetallic alloys. *Nature Communications* **5**, 5062 (2014).

[46] Sutter, P.; Sadowski, J. T.; Sutter, E. A. Chemistry under cover: tuning metal–graphene interaction by reactive intercalation. *Journal of the American Chemical Society* **132**, 8175 (2010).

[47] Ferrighi, L.; Datteo, M.; Fazio, G.; Di Valentin, C. Catalysis under cover: Enhanced reactivity at the interface between (doped) graphene and anatase TiO_2. *Journal of the American Chemical Society* **138**, 7365 (2016).

[48] Granas, E.; Knudsen, J.; Schröder, U. A.; Gerber, T.; Busse, C.; Arman, M. A.; Schulte, K.; Andersen, J. N.; Michely, T. Oxygen intercalation under graphene on Ir (111): energetics, kinetics, and the role of graphene edges. *ACS Nano* **6**, 9951 (2012).

[49] Bignardi, L.; Lacovig, P.; Dalmiglio, M. M.; Orlando, F.; Ghafari, A.; Petaccia, L.; Baraldi, A.; Larciprete, R.; Lizzit, S. Key role of rotated domains in oxygen intercalation at graphene on Ni (111). *2D Materials* **4**, 025106 (2017).

[50] Sutter, P.; Albrecht, P.; Tong, X.; Sutter, E. Mechanical decoupling of graphene from Ru (0001) by interfacial reaction with oxygen. *The Journal of Physical Chemistry C* **117**, 6320 (2013).

[51] Vlaic, S.; Kimouche, A.; Coraux, J.; Santos, B.; Locatelli, A.; Rougemaille, N. Cobalt intercalation at the graphene/iridium (111) interface: Influence of rotational domains, wrinkles, and atomic steps. *Applied Physics Letters* **104**, 101602 (2014).

[52] Sicot, M.; Leicht, P.; Zusan, A.; Bouvron, S.; Zander, O.; Weser, M.; Dedkov, Y. S.; Horn, K.; Fonin, M. Size-selected epitaxial nanoislands underneath graphene moiré on Rh (111). *ACS Nano* **6**, 151 (2012).

[53] O'Hern, S. C.; Boutilier, M. S.; Idrobo, J.-C.; Song, Y.; Kong, J.; Laoui, T.; Atieh, M.; Karnik, R. Selective ionic transport through tunable sub-nanometer pores in single-layer graphene membranes. *Nano Letters* **14**, 1234 (2014).

[54] Romero-Muñiz, C.; Martín-Recio, A.; Pou, P.; Gómez-Rodríguez, J. M.; Pérez, R. Unveiling the atomistic mechanisms for oxygen intercalation in a strongly interacting graphene–metal interface. *Physical Chemistry Chemical Physics* **20**, 13370 (2018).

[55] Schumacher, S.; Huttmann, F.; Petrović, M.; Witt, C.; Förster, D. F.; Vo-Van, C.; Coraux, J.; Martinez-Galera, A. J.; Sessi, V.; Vergara, I. Europium underneath graphene on Ir (111): intercalation mechanism, magnetism, and band structure. *Physical Review B* **90**, 235437 (2014).

[56] Li, G.; Zhou, H.; Pan, L.; Zhang, Y.; Huang, L.; Xu, W.; Du, S.; Ouyang, M.; Ferrari, A. C.; Gao, H.-J. Role of cooperative interactions in the intercalation of heteroatoms between graphene and a metal substrate. *Journal of the American Chemical Society* **137**, 7099 (2015).

[57] Ma, Y.; Travaglia, E.; Bana, H.; Bignardi, L.; Lacovig, P.; Lizzit, S.; Batzill, M. Periodic Modulation of Graphene by a 2D-FeO/Ir (111) Moiré Interlayer. *The Journal of Physical Chemistry C* **121**, 2762 (2017).

[58] Dedkov, Y. S.; Fonin, M.; Rüdiger, U.; Laubschat, C. Graphene-protected iron layer on Ni (111). *Applied Physics Letters* **93**, 022509 (2008).

[59] Preobrajenski, A.; Ng, M. L.; Vinogradov, A.; Mårtensson, N. Controlling graphene corrugation on lattice-mismatched substrates. *Physical Review B* **78**, 073401 (2008).

[60] Miniussi, E.; Pozzo, M.; Baraldi, A.; Vesselli, E.; Zhan, R.; Comelli, G.; Menteş, T.; Niño, M.; Locatelli, A.; Lizzit, S.; Alfè, D. Thermal stability of corrugated epitaxial graphene grown on Re (0001). *Physical Review Letters* **106**, 216101 (2011).

Chapter 4

Titania interfaces for photocatalysis

Titanium dioxide (TiO_2), also called titania, is a natural occurring oxide of titanium, which has been largely employed for a broad range of applications. TiO_2 is used as a white pigment in paintings and food colourings and it is one of the basic components of sunscreens, due to its high UV absorption efficiency [1]. It is employed in plastics for its capablility to provide UV resistance; in ceramic industry it is used as opacifier and crystallization seed, while in optics titanium dioxide is used in thin film coatings as a high refraction index material for visible light applications. More recently, it has been employed in form of nanoparticles as semiconductor in dye-sensitized solar cells [2, 3].

Among the features that make titania useful, there is one that is very appealing for industrially-oriented applications: its photocatalytic activity. Evidences of the photochemical power of TiO_2 have been reported back in 1929 as observation on paints flaking and fabric degradation under solar light irradiation. It is not clear when and who started using titania as an active photocatalyst for chemical reactions [4], but from 1956 a series of investigations by Kato *et al.* [5] reported the photoactivated "auto-oxidation" processes of organic solvents in which titania powder was dispersed, concluding also that the photocatalytic activity of titanium dioxide is higher in its anatase allotropic form, compared to rutile. In 1969, Fujishima e Honda demonstrated for the first time the effectiveness of titanium dioxide in the electrochemical photolysis of water and their results were then reported in Nature in 1972 [6], opening a new promising branch of research.

Nowadays, despite the remarkable progress made in this field, a clean and efficient mass production of hydrogen relying on photocatalytic water splitting remains a target to be achieved. There is no doubt in the effectiveness of

titanium dioxide as a water dissociation photocatalyst when compared with a series of other metal oxide semiconductors, but a solution to address its non-competitive efficiency with respect to conventional H_2 production methods is still missing.

The aim of the experimental work discussed in this chapter is to address this issue by nano-fabrication. Photocatalytic processes are in fact determined by the electronic structure of the catalyst and one of the most important possibilities offered by nano-engineering is the modification of the electronic structure of matter. This has been the focus of our investigation. Before starting describing the nanoarchitectures we designed and produced, it seems appropriate to introduce the basic concepts of photocatalysis, which drove our experiments.

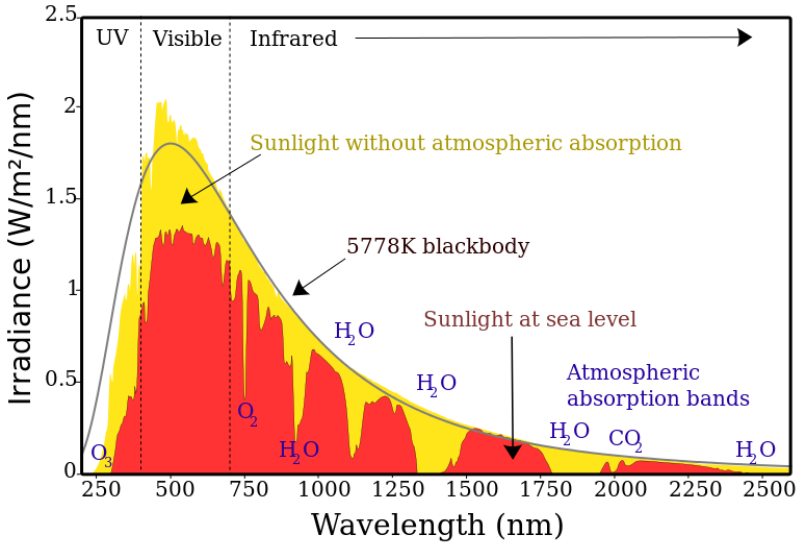

Figure 4.1: Spectrum of the solar radiation at the Earth surface in comparison with the extraterrestrial solar spectrum. About 40% of the total power impinging the ground is delivered by visible radiation, while UV power is about 3% of the total. It is evident how achieving efficient light harvesting in the visible range appears as one of the challenges in the development of solar technologies. Data from American Society for Testing and Materials (ASTM) Terrestrial Reference Spectra for Photovoltaic Performance Evaluation.

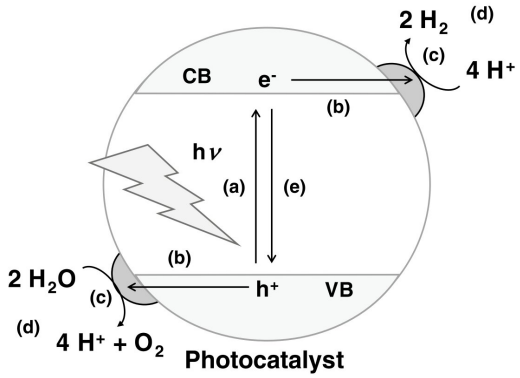

Figure 4.2: Photocatalytic water-splitting reactions on a semiconductor particle. (a) Light absorption; (b) charge transfer; (c) redox reactions; (d) adsorption, desorption, and mass diffusion of chemical species; and (e) charge recombination. Reprinted from [7].

4.1 Water splitting reaction in semiconductor photocatalysts

In a Photo-Electro-Chemical (PEC) reaction the energy necessary for the reaction to occur is provided by an external photon and transfered to the reactants by excited electric charges. The starting point of a semiconductor photocatalytic process is the absorption of a photon and the creation of an electron e^- in the conduction band (CB) of the material and a hole h^+ in the valence band (VB). The first important requirement of a material to be an efficient photocatalyst is therefore its photon absorption efficiency. The charges, in order to participate to the reaction, have to separate from each other and migrate to the surface of the photocatalyst. Here emerges another important characteristic for a photocatalyst, i.e. the charge transport properties. At this point of the process, we have to consider separately the oxidation and reduction parts of the reaction: the oxidation involves the hole, while the reduction regards the excited electron. The condition for the photocatalytic reaction to occur is that the conduction and valence band potentials where e^- and h^+ have been excited, must be larger than the potentials of the reduction and oxidation reactions, respectively. Usually, these potentials are expressed as a difference with respect to the so called Standard Hydrogen Electrode (SHE), which corresponds to the potential of a particular ideal half galvanic cell to be used as a reference for any other electrode.

SHE is defined as the potential of a platinum electrode immersed in a 1

molar strong acid solution, in equilibrium with a flux of hydrogen bubbling at 1 bar inside the solution; the equilibrium condition referring to the reaction

$$2\,\mathrm{H^+}_{(\mathrm{aq})} + 2\,\mathrm{e^-} \longrightarrow \mathrm{H}_{2(\mathrm{g})}.$$

In general, the potential of a half galvanic cell is temperature dependent, and so it is also for a half cell built with the SHE characteristics; for this reason, in order to always have a reference potential, the value of SHE is declared to be zero at all temperatures.

Considering the specific case of water splitting, we have that the total reaction is [7]

$$\mathrm{H_2O} \longrightarrow \mathrm{H_2} + \frac{1}{2}\,\mathrm{O_2} \qquad \Delta G^0 = +237\,\mathrm{kJ/mol} \tag{4.1}$$

where the Gibbs free energy ΔG^0 is provided by photon absorption and is equivalent to 2.46 eV per molecule[1]. The oxidation of water leads to the formation of molecular oxygen and protons, while the excess electrons fill the excited hole in the semiconductor.

$$\mathrm{H_2O} \longrightarrow \frac{1}{2}\,\mathrm{O_2} + 2\,\mathrm{H^+} + 2\,\mathrm{e^-} \qquad E^0 = 1.23\,\mathrm{V} \tag{4.2}$$

Relatively to the SHE, the potential E^0 of this reaction is 1.23 V. On the other hand, the proton reaction, involving the excited electron in the CB of the semiconductor, has a potential equal to the SHE.

$$2\,\mathrm{H^+} + 2\,\mathrm{e^-} \longrightarrow \mathrm{H_2} \qquad E^0 = 0\,\mathrm{V} \tag{4.3}$$

If we represent on a graph the value of the redox potentials and the titanium bands potentials, we obtain the scheme shown in fig. 4.3. We can observe that the requirement on the position of CB and VB respect to the redox potentials are fulfilled by titanium dioxide. Nevertheless, the energy gap of $\mathrm{TiO_2}$ is 3.2 eV. This means that to excite an electron in CB, the energy of the photon must be more than two times the electron energy required by the reaction (1.23 eV). This condition limits the photocatalytic application of titania to the UV light, while in principle the reaction is possible with the whole visible range. One of the major challenges in photocatalytic hydrogen production is to address this issue by finding new semiconductor materials with the optimal energy gap and the required chemical stability.

[1] The photocatalytic water splitting reaction includes a net energy absorption so, according to the traditional definition, it is not a proper catalytic process, even if this terminology has been widespread since a long time.

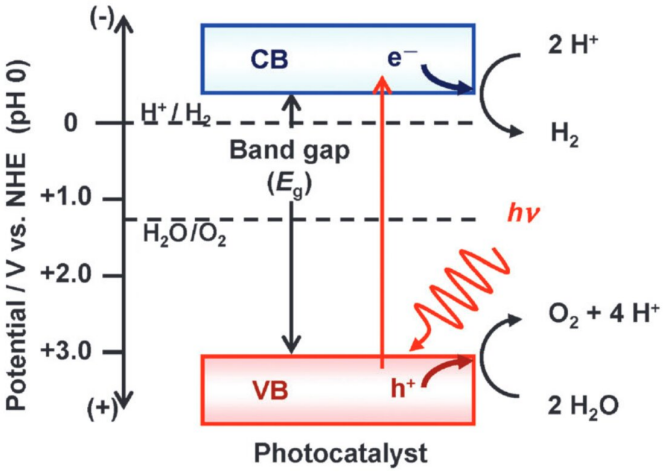

Figure 4.3: Energy diagram for photocatalytic water splitting in titanium dioxide. NHE stands for Normal Hydrogen Electrode, which is the real counterpart of the ideal SHE. It corresponds to the potential of a platinum half cell with a pH=0 acid solution (correspondent to a 1 molar solution of a perfect strong acid) and hydrogen bubbling at 1 atm. Image reprinted from [8].

In last decades several metal oxide semiconductors have been investigated, both singularly and coupled among each other to build composite photocatalysts in which the redox reactions occur on different sites [9]. The possibility to dope the semiconductors with metallic and non-metallic elements in order to add electronic states inside the TiO_2 energy gap have been widely investigated, still bringing to not fully satisfactory results [10, 11]. An important step towards the optimization of titanium dioxide for photocatalysis was considering it in form of nanoparticles and investigating the dependence of its activity on the particles size [12–14]. Since the beginning it seemed clear that the increasing of the surface to bulk ratio going from bulk to particles was not enough to explain the increasing in the PEC activity.

The reduction of the size of the TiO_2 particles to the order of tens of nm, originates a series of structural and electronic modification that have been investigated in a huge amount of scientific works. As an example, the crystalline structure of titania, already known to affect the photoelectrochemical activity, has been demonstrated to be dependent on the particle size. Indeed, it has been experimentally observed and theoretically calculated that anatase is thermodynamically most stable for NPs with diameter less than 11 nm, brookite is most stable for crystal sizes between 11 and 35 nm, and rutile is most stable at sizes exceeding 35 nm [15–17]. Particles within this size range have been

revealed to possess a high density of oxygen vacancies, whose presence strongly enhances the titania activity [18–20]. This phenomenon has been experimentally confirmed but not fully understood; hypothesis have been made regarding the role of defects as active sites for the dissociation of water molecules [21] and in determining the band gap of the material [22].

In summary, the most important factors that affect the photoelectrochemical activity of titanium dioxide are: (i) the band gap, determining the light absorption range; (ii) the position of conduction and valence bands, that have to fulfill the potential requirements; (iii) the charge carrier mobility, i.e. the efficiency of the charge migration to the surface of the catalyst; (iv) the density of oxygen defects; (v) the electron and hole lifetime, which is related to the charge carrier mobility and determines the rate of the e^- - h^+ recombination, a process competing with the photocatalytic reaction.

In this context the combination of TiO_2, mostly in clusterized form, with carbon-based material brought considerable results, starting with the employment of graphite and activated carbon and expanding after the introduction of graphene [23, 24]. Significant advances have been made associating titanium dioxide nanocrystals with reduced graphene oxide in solution [24–26], enhancing the charge carriers mobility and extending the activity of TiO_2 to visible light. This light absorption extension has been described as the consequence of two new absorption pathways. When graphene is in contact with titania, electrons can be excited from the valence band of graphene either directly to the TiO_2 conduction band or to the conduction band of graphene itself, with a subsequent transition from graphene to titania conduction band. At the same time, the charge transport efficiency of graphene has been identified as the cause of a more efficient charge separation that leads to a longer electron-hole lifetime [27, 28]. It is worth noting that to make full use of the electronic properties of graphene, its quality in terms of domain extension and defect density has to be high. This aspect was investigated extensively, to the point of declaring, for TiO_2-carbon composite in liquid phase for photocatalytic application, that "*TiO_2/GR is in essence the same as other TiO_2/carbon (carbon nanotubes, fullerenes, and activated carbon) composite materials on enhancement of photocatalytic activity of TiO_2*" [29]. Despite this, many graphene-TiO_2 efficient compounds obtained in solution have been presented as promising technologies for sun-powered hydrogen production. Nevertheless, the liquid phase and the insufficient chemical stability of these compounds prevent them from a direct practical application. In industry, solid catalysts are indeed preferred respect to liquid ones for several reasons; they are in general easier to separate from the

products of the reaction, easier and safer to handle and in many cases more environmentally friendly than their liquid counterpart, more stable and easier to regenerate. In the specific case of Gr-TiO_2 nanocomposites, the majority of the liquid-phase synthetic approaches for their production lead to a non-uniform distribution of titania nanoparticles, that can undergo coalescence phenomena reducing their active surface area. Furthermore, they are often characterized by the presence of functional groups that potentially act as recombination sites for photo-excited charges.

In these respects, advantages in the employment of a solid support for this kind of composite photocatalysts are evident. Very high quality grahene can be grown on a series of crystalline metal surfaces by chemical vapour deposition. At the same time, graphene itself can be used as a substrate for the deposition of titania NPs, ensuring an optimal contact between the two materials without the employment of functional groups, in total absence of solvent agents. Moreover, the interaction of the nanoparticles with the solid support increases their stability with respect to coalescence phonomena. These considerations are at the basis of the design of our graphene-based TiO_2 nanostructured interfaces.

4.2 Sandwiched titania/graphene architectures

We designed and characterized three different TiO_2 nanostructured architectures, as illustrated in figure 4.4, with the aim of comparing their photocatalytic activity. Titania was growth in a similar way on the three substrate represented in figure 4.4a, b and c. Graphene supported nanoparticles (TGM, in fig. 4.4e) were compared with nanoparticles supported by Gr/$TiO_{1.5}$ (TGTM, fig. 4.4f) and with a thin layer of titanium dioxide directly grown on Ir (111) (TM, fig. 4.4d). The goal of the investigation illustrated in this section was to comprehensively characterize the TM, TGM and TGTM architectures, in order to point out the diversities in the structural, chemical and electronic features of TiO_2, leading to remarkable differences in their photocatalytic activity.

The description of the three systems will include some relevant details about their preparation, especially for the case of TGTM. The titanium oxide thin-layer intercalated below graphene will be firstly compared with an analogous titanium oxide thin-layer grown on pristine Ir (111) in section 4.2.1. The effects of the intercalated oxide on graphene will be shown and titanium doses employed for the interfaces preparation will be discussed, before moving the attention to the final TM, TGM and TGTM structures, in section 4.2.2.

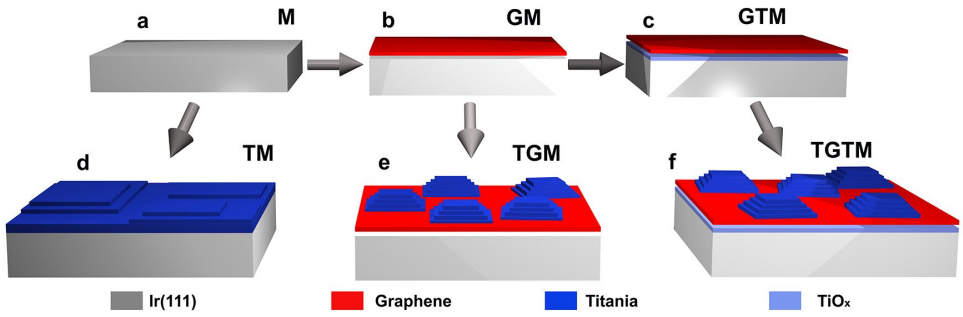

Figure 4.4: Schematic representation of the experimental preparation of the titania interfaces. a) Clean Ir (111) surface (M); b) Graphene on Ir (111) (GM); c) Graphene on titanium oxide thin layer obtained by intercalation method (GTM); d) TiO_2 layer directly grown on Ir (111), (TM); e) TiO_2 nanoparticles grown on graphene (TGM); f) TiO_2 nanoparticles on graphene supported by TiO_2 thin layer (TGTM).

4.2.1 Interfacial titanium oxide

The first part of the experimental activity related to titanium oxide-based architectures was dedicated to the design of the Gr/Ti-oxide/Ir (111) structure (GTM). Our goal was to obtain a substrate formed by a graphene layer supported by a thin layer of intercalated titanium oxide. The ideal requirements we imposed for this preparation were the integrity of the graphene layer after the oxide intercalation and the creation of an intercalated layer that could cover completely the Ir (111) surface. These requirements regarded the qualitative and quantitative aspects of the intercalation method.

The titanium oxide present in our architectures was obtained in all cases as result of a two step procedure consisting of the deposition of metallic titanium and its subsequent oxidation. Ti was deposited on the surface by sublimation in UHV from a high purity filament. The titanium evaporator was equipped with a quartz microbalance that we used to control the coverage. To ensure a reliable calibration for the microbalance, we performed the quantitative calibration procedure, based on HR-XPS, described in section 2.5.2. To intercalate Ti below graphene we kept the Gr/Ir (111) sample at 670 K during the exposure to the Ti vapours. This temperature value was found to be the lowest allowing an efficient intercalation process and was chosen in order to reduce the possibility of defect formation on graphene.

The experimental setup of the SuperESCA beamline allowed to perform time resolved XPS measurements during the intercalation, acquiring the C $1s$ spectrum in order to follow the changes in graphene and, in parallel, Ir $4f_{7/2}$ to

verify the ongoing intercalation. Ti $2p$ evolution was not monitored during the process. This choice was justified by two main reasons: first, we did not expect any appreciable change in the Ti $2p$ spectral features as a function of coverage, as we did, instead, for both C $1s$ and Ir $4f_{7/2}$; second, for a given small amount of titanium (a fraction of monolayer), the acquisition time for a single spectrum should be longer respect to C $1s$ and Ir $4f_{7/2}$ because of the low intensity of the Ti $2p$ signal, increasing the acquisition time of our measurement.

In figure 4.5 the time evolution of the Ir $4f_{7/2}$ and C $1s$ spectra is reported. Each spectrum was fitted using Doniach-Šunjić profiles convoluted with a Gaussian in order to deconvolve the single spectral components and plot the relative intensities as a function of time. The initial spectra are relative to Gr/Ir (111): C $1s$ is characterized by a narrow photoemission component (A) at 284.11 eV, while Ir $4f_{7/2}$ shows the surface (S_0) and bulk (B) components with the same features described in section 3.3: if compared to that Ir $4f_{7/2}$ spectrum, the initial spectrum of this time-resolved series is characterized by a less pronounced signal minimum between B and S. The reason for this is due to the high temperature at which the latter is acquired, introducing a Gaussian broadening on the photoemission components and to the reduced surface sensitivity obtained with 400 eV photon energy.

During the intercalation, the S_0 component decreases in time and finally vanishes, while a new surface component S_1 appears. On the other hand, the C $1s$ A component decreases in intensity while two new components at higher binding energy appear at 284.54 eV (I_1) and 284.88 eV (I_2). A shift towards higher binding energies is observed for the A component at the beginning of the intercalation. This is usually observed when the intercalated material randomly and homogeneously diffuses at the interface between Gr and Ir (111). After about 1000 s, the A component vanished while I_1 and I_2 got stabilized; the sum of the final intensities of I_1 and I_2 is equal to the (90 ± 5) % of the initial intensity of A. From these observations we can conclude that the most conceivably interpretation for the consistent conversion of S_0 into S_1 and the barely appreciable decrease of the total C $1s$ signal is the presence of a new chemical species in contact with Ir (111) and below the graphene layer, i.e. the intercalated titanium. Moreover, since at the end of the intercalation we did not detect any XPS signal from C atoms in the Gr/Ir (111) configuration, we considered the deposited Ti sufficient for the construction of our interface layer. Intercalation was confirmed by an oxygen exposure at 10^{-7} mbar which did not resulted in any Ti-oxide formation, according to Ti $2p$ measurements. Quartz microbalance measurements and XPS quantitative calculations are in

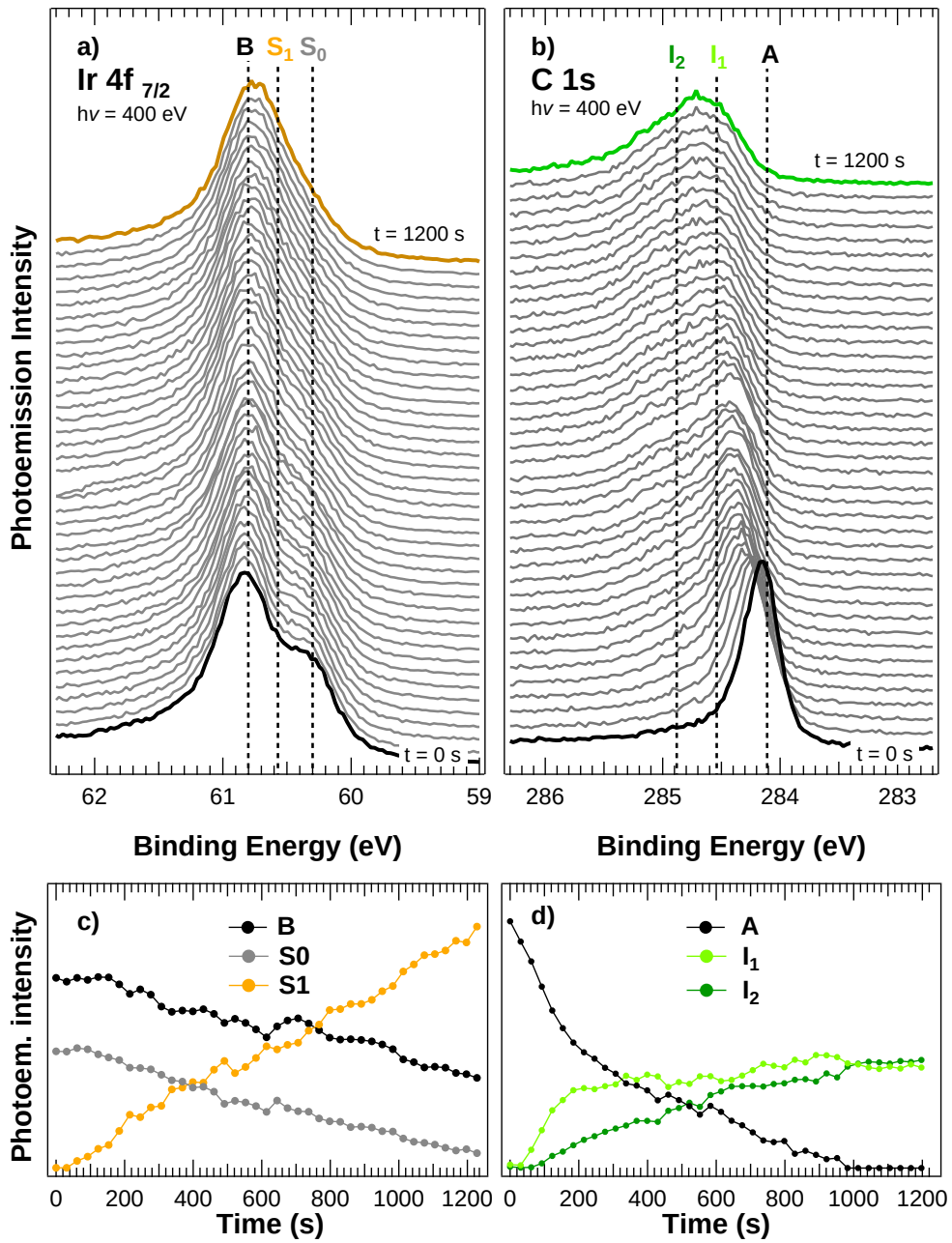

Figure 4.5: Time resolved XPS measurements acquired during the Ti intercalation at 400 eV photon energy. a) Time evolution of the Ir $4f_{7/2}$ spectrum; b) time evolution of the C $1s$ spectrum; c) intensity plot of the time evolution of Ir $4f_{7/2}$ components calculated by fitting procedure; d) intensity plot of the time evolution of C $1s$ photoemission components calculated by fitting procedure.

agreement with the coverage value which is 0.50±0.05 ML.

Further considerations can be done on the HR-XPS results, about the graphene/substrate interaction. High resolution photoemission spectra for C 1*s* are reported in figure 4.6. The overall C 1*s* core level shift to higher binding energies indicates an increase of this interaction. At the same time, the presence of two distinct spectral components can be attributed to an enhancement of the moiré corrugation, as reported for other high interacting substrates such as Fe, Ru, Rh and Co [30–32]. In analogy with these systems, the two photoemission components I_1 and I_2 can be related respectively to strongly- and weakly-interacting carbon species inside the moiré supercell. Regarding the line shape of these spectral features, we observe that while the Lorentzian width (0.13 eV) and the asymmetry parameter (0.12) of both I_1 and I_2 are unchanged respect to A, the Gaussian contribution is larger and equal to 0.39 eV for I_1 and 0.69 eV for I_2. This suggests that the number of different possible local configuration for C atoms is increased, even if the periodicity of the moiré structure is preserved.

Once we confirmed the successful metallic titanium intercalation, we performed the oxidation of the Ti interface layer. The procedure we applied is similar to the one reported for the oxygen intercalation below Gr/Ir (111) [33] and Gr/Ni_3Al (111) [34].

The sample was kept at 570 K and exposed for 1 h to a flux of oxygen. The oxygen exposure was performed by means of a gas doser. The purpose of a doser, which is a tube with an inner diameter equal to the diameter of the Ir sample placed at a distance of 1 mm from it, is to carry the gas directly on the sample surface, producing an enhancement of the local pressure by a factor 50 for the case of our setup. With this configuration, the oxygen pressure measured in the experimental chamber was 1×10^{-4} mbar, that means 5×10^{-3} mbar on the sample and a total exposure of 1.8×10^{7} Langmuir.

HR-XPS measurements were performed after the oxidation process; the C 1*s* spectrum is shown in figure 4.6 (GTM). One single component is observed at BE = 283.81 eV. Lorentzian width and asymmetry parameter maintain the value of Gr/Ir (111) and Gr/Ti/Ir (111), while the Gaussian width (0.37 eV) decreased with respect to the I_1 and I_2 components of the Gr/Ti/Ir (111). Important information can be retrieved from these observations. First of all, the suppression of the moiré corrugation and the absence of a clear distinction between strongly- and weakly-interacting regions in graphene. Nevertheless, the Gaussian broadening of the C 1*s* respect to Gr/Ir (111) suggests the presence of a variety of different chemical environments for C atoms. The second important consideration derives from the comparison of the binding energies of the C 1*s* core levels before and after the creation of a titanium oxide layer below graphene.

The GTM system is characterized by the presence of high quality and slightly p-doped graphene.

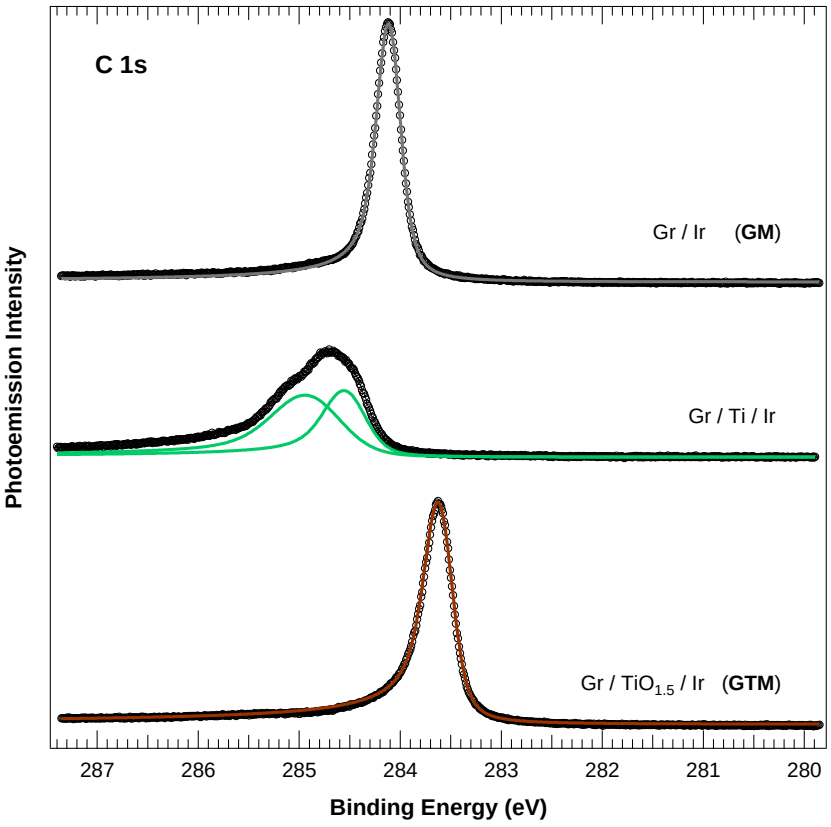

Figure 4.6: C 1*s* high resolution photoemission spectra acquired at 400 eV photon energy for clean graphene (GM), after titanium intercalation and after the intercalated titanium oxidation (GTM).

Moving the focus of this characterization to the titanium oxide layer, we performed a comparison between the intercalated oxide layer and an equivalent 0.5 ML titanium oxide directly grown on Ir (111).

Before growing the nano-architectures, more precise information were needed about the growth of Ti on Ir (111), which was achieved by dosing Ti at room temperature with the same evaporation parameters of GTM. Ti oxidation was then achieved exposing the surface to 5×10^{-6} mbar of oxygen for 600 s at room temperature.

In figure 4.7 the Ti 2*p* spectra for titanium oxide on pristine Ir (111) and under graphene are reported. Because of the large chemical shifts, comparable with the spin-orbit splitting, we analysed both $2p_{3/2}$ and $2p_{1/2}$ components. The oxidation states components are easy to identify, referring to the chemical

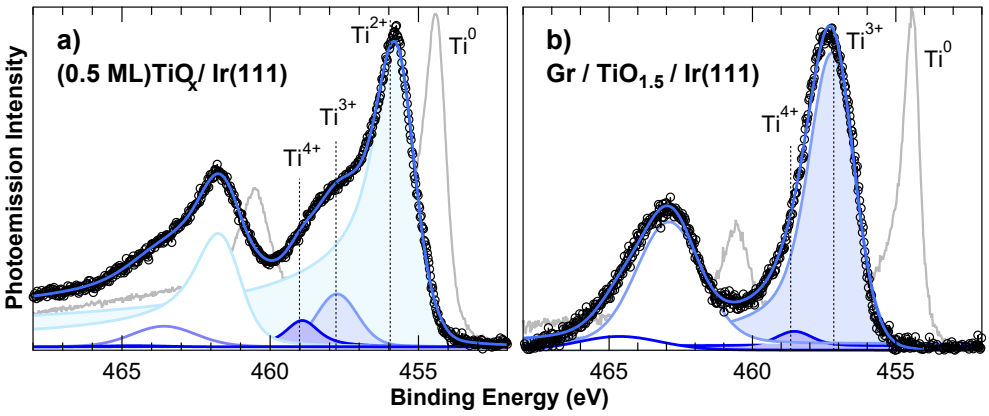

Figure 4.7: Ti $2p$ photoemission spectra acquired at 550 eV. a) 0.5 ML Ti-oxide layer grown at room temperature on Ir (111); the spectrum acquired after Ti deposition, before the oxidation is shown on the background. b) 0.5 ML Ti-oxide intercalated at the Gr/Ir (111) interface; the spectrum acquired before the oxidation is shown for comparison.

shifts reported in literature for the oxidation states of titanium [35]. In the case of titanium oxide thin film deposited on Ir (111), Ti^{2+} at 456 eV appears as the main spectroscopic component, (80±5)% of the total spectral weight. This trend is in agreement with that of titanium oxide on Pt (111) [36], in which the strong interaction between titanium and metallic substrate hinders the titanium oxidation at room temperature. The lineshape of the Ti^{2+} is significantly asymmetric, meaning that the thin oxide layer preserves a metallic character.

By contrast, the intercalated oxide layer is characterised by the exclusive presence of the Ti^{3+} and Ti^{4+} components (458 and 459 eV respectively) where the Ti^{3+} accounts for more than 90% of the total spectral weight.

From the average oxidation state and from the quantitative XPS measurements of the O $1s$ spectrum, we can calculate the average stoichiometry of the oxides, which results to be $TiO_{1.1}$ on Ir (111) and $TiO_{1.5}$ in the GTM interface. It is noticeable that the oxidation number of titanium below graphene is, in average, larger than that of oxidized Ti on Ir (111). The reason for this can be in the high temperature and pressure values used for the oxidation of the intercalated layer with respect to the ones used for Ti/Ir (111).

Regarding the structure of the two oxides, we acquired LEED images to investigate the long range order within each layer of the two oxides. For $TiO_{1.1}$/Ir (111) grown at room temperature we do not observe any ordered structure, while after Ti intercalation for GTM we observe a 2×2 superstruc-

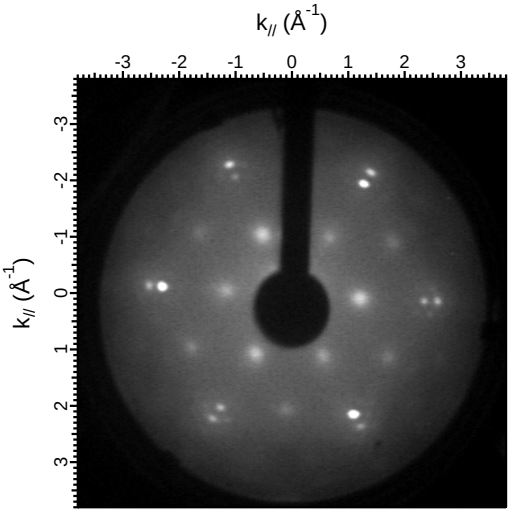

Figure 4.8: Low Energy Electron Diffraction image acquired on the Gr/Ti/Ir (111) system at 114 eV electron energy.

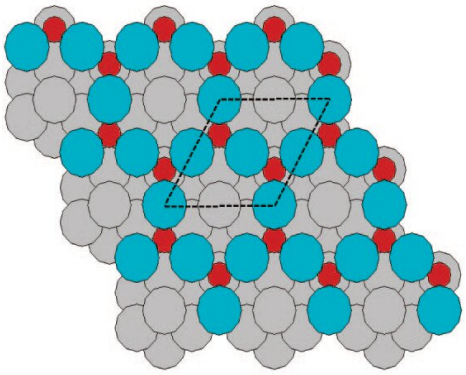

Figure 4.9: Structural model of the ordered oxide layer grown on Pt (111) by deposition of 0.5 ML of titanium and exposure to oxygen at 673 K. Image from [36].

ture respect to the Ir (111) cell, generated by the intercalated Ti atoms (figure 4.8). No oxygen was indeed observed by HR-XPS after the Ti intercalation, suggesting that the 2×2 superstructure was actually generated by the intercalated metal and it was not a spurious consequence of any oxygen contamination. From this observation, along with the the surface density of titanium (0.5 ML) and the oxide stoichiometry obtained after the oxidation process ($TiO_{1.5}$), we can reasonably assume that the structure obtained under graphene resembles the one obtained by Barcaro *et al.* [36] on Pt (111) at the same growth temperature (figure 4.9).

In the frame of the comprehensive characterization of the titanium nanostructured interface for photocatalytic application, we performed theoretical calculations in order to better describe the morphology of the interface. The calculation have been performed by the collaborating group headed by Prof. Alfè at University College London. Density functional theory calculations were performed to simulate the geometric structure and calculate the partial density of states of the GM and GTM architectures.

We described the composite material using four layers of a 10×10 iridium hexagonal supercell. On top of them we added the titanium oxide layer with the same structure described by Barcaro *et al.* [36] for the $TiO_{1.5}$/Pt (111), at 2.5 Å from the last iridium layer. Last, a 11×11 graphene supercell was added at 3.5 Å from the oxide layer, which is close to the average distance of graphene from the substrate when it is supported on Ir (111).

In parallel, we performed the same structural analysis on the Gr/Ir to have a reference system. From the simulation we obtained the sets of atomic spatial coordinates that simulate the interfaces. The first remarkable result regards the configuration of the oxide layer. The initially coplanar titanium and oxygen atoms are actually more energetically stable in a configuration where oxygen atoms are lifted while titanium atoms are closer to the Ir (111) surface. The second observation regards the position of graphene. The average distance of the carbon atoms from the oxygen atoms in the titanium oxide layer is 3.08 Å, which is slightly smaller with respect to the value of distance between graphene and iridium in the reference system. Moreover, we observed a change in the corrugation of graphene (see fig. 4.10). While Gr on Ir (111) presents differences in the vertical coordinates of carbon atoms up to 0.35 Å, following the typical moiré pattern, Gr on titanium oxide presents a corrugation which is less than 0.07 Å and does not preserve the moiré configuration. The periodic corrugation is indeed due to the interaction of graphene with the metallic substrate; the intercalated oxide reduces this interaction, as observed also in the C 1*s* spectrum, and causes the flattening of the graphene layer.

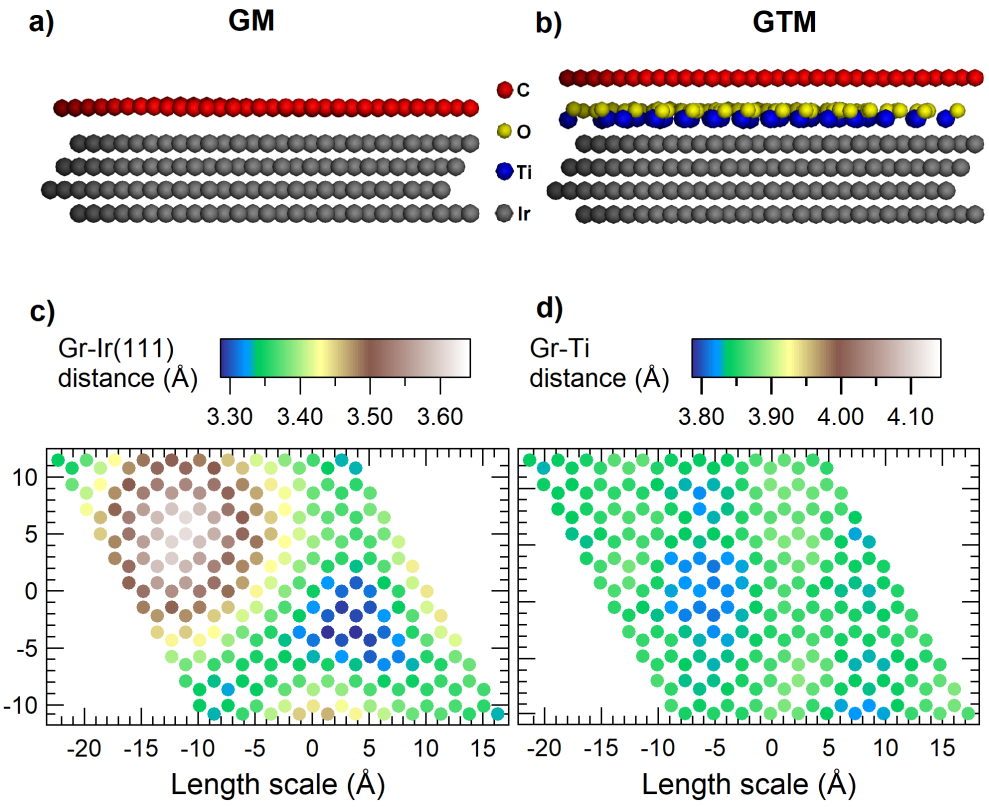

Figure 4.10: DFT simulated structure for a) Gr/Ir (111) (GM) and b) Gr/$TiO_{1.5}$/Ir (111) (GTM); c) top view of the graphene atomic spatial coordinates obtained as a result of the DFT structural calculation for graphene on Ir (111) and for graphene on the $TiO_{1.5}$ interface layer d)

4.2.2 Titania nanoparticles and thin film growth

The TiO_2 NPs growth on graphene has been performed in two steps, growing metallic particles first and oxidizing them afterwards. To synthesize metallic nanoparticles on graphene, we exposed the graphene-covered Ir (111) sample to Ti vapours, keeping it at room temperature and in UHV condition (base pressure $\sim 5\times10^{-10}$ mbar). An equivalent amount of Ti (about 2.5 ML) was deposited, in the same condition, on Ir (111). Photoemission spectra were acquired on the metallic particles to check the presence of contaminants before proceeding with the oxidation. The spectra obtained for Ti $2p$, reported in figure 4.13, show the presence of titanium in the metallic state, without any significant amount of oxidized species, neither for the particles on Gr, nor for the thin layer on Ir (111).

To obtain titania, metal particles were exposed to 5×10^{-6} mbar partial

pressure of oxygen at room temperature for 600 s. Pressure and time values for the oxygen exposure were defined through a time resolved XPS measurement performed during trial preparations. The goal of the oxidation process was to minimize the amount of metallic titanium and maximise the amount of oxygen. From time resolved measurements we observed that a further exposure of clusters to oxygen did not produce any significant change in their chemical composition. The same conclusion was obtained also for titanium deposited directly on Ir (111).

The first important result of the morphology investigation we performed on the three interfaces concerns the form of titanium dioxide on Ir (111) (TM architecture). From spectroscopic investigations emerged that the Ti growth takes place in layer-by-layer mode and the layered structure is preserved also after the oxidation. Ti growth on Ir was performed in steps with sub-monolayer depositions followed by oxidation. From the quantitative measurements on the oxidation states of titanium we deduced that the structure of the first titanium oxide is similar to the one of the thin layer intercalated under graphene, whose characteristics resemble those of titanium oxide on Pt (111). On the basis of this consideration, the amount of titanium deposited on Ir (111) for the TM system was defined to be equal to the total amount of titanium employed in the growth of the TGTM, so to have the same amount of TiO_2 in all the three interfaces.

Scanning tunneling microscopy images were acquired to statistically investigate the NPs population on TGM and TGTM. No significant differences were observed between the two systems. Images shown in figure 4.13 refer to TGTM; the titanium dioxide coverage is equivalent to 2.4 ML. The size distribution of particles so obtained was calculated through the "watershed" algorithm from the Gwyddion software library [37]. The resulting histogram is reported in figure 4.11c. Particles size distribution, which ranges from 3 to 30 nm, is peaked at 9 nm. A homogeneous distribution of particles on graphene is observed on images acquired on a length scale of $2000 \times 2000\,\mathrm{nm}^2$ on the sample. From the analysis of the scan line profiles, the average surface corrugation is about 10 Å, as illustrated in figure 4.11b.

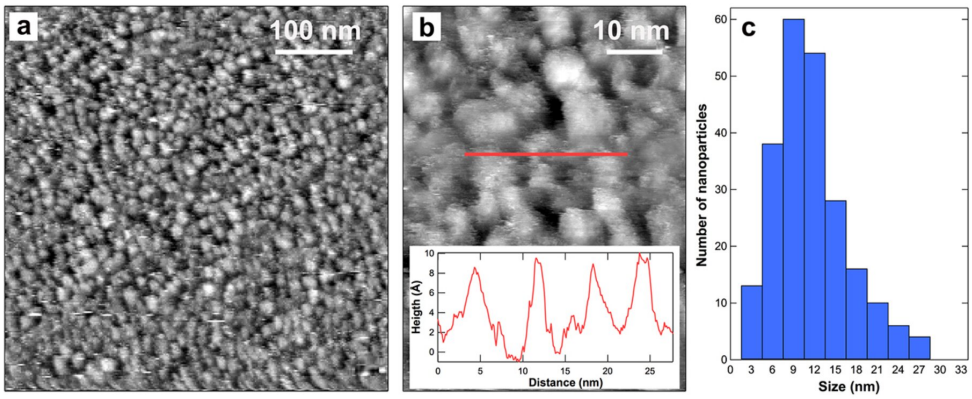

Figure 4.11: Structural characterisation of selected systems. a) and b) STM images of TGTM (a: 500×500 nm^2, b: 100×50 nm^2. Bias=2.1 V, Current=0.42 nA). The inset shows the height profile measured along the red line; c) Size distribution of the titania nanoparticles obtained from image a.

It has been already mentioned in the paragraph above that the photocatalytic activity of titania depends on its crystalline structure, being anatase the most active allotrope among the most common three (rutile, anatase and brookite). In order to account for differences in the activity of our interfaces, that could be due to different cristalline structures, we investigated the three interfaces from this perspective, using Near Edge X-ray Absorption Fine Structure technique (NEXAFS). We acquired absorption spectra from each sample, measuring the X-ray absorption coefficient around the L_3 and L_2 absorption edges of titanium as a function of the photon energy. The absorption value has been evaluated as the intensity of the Ti LMM Auger photoelectron component with 418 eV kinetic energy. Data are reported in figure 4.12. Region 1 (455-461 eV) and 2 (461-468 eV) refer to L_3 and L_2 edges, respectively. Both regions show an intense and structured pre-edge feature. The fine structure is due to the splitting of the Ti d^* bands due to the crystal symmetry. The energy value of the maxima is a fingerprint of the various existing TiO_2 crystal structures, thus allowing for example to distinguish the rutile and the anatase phases in titania [38]. More specifically, in our case the L_3 maxima are found at 458.0 eV (A) and 459.8 eV (B), which indicates that the local crystal structure in our TiO_2 nanoparticles and thin layer is anatase. Anatase has indeed been proved to be the most common phase of TiO_2 for nanocrystals [39, 40].

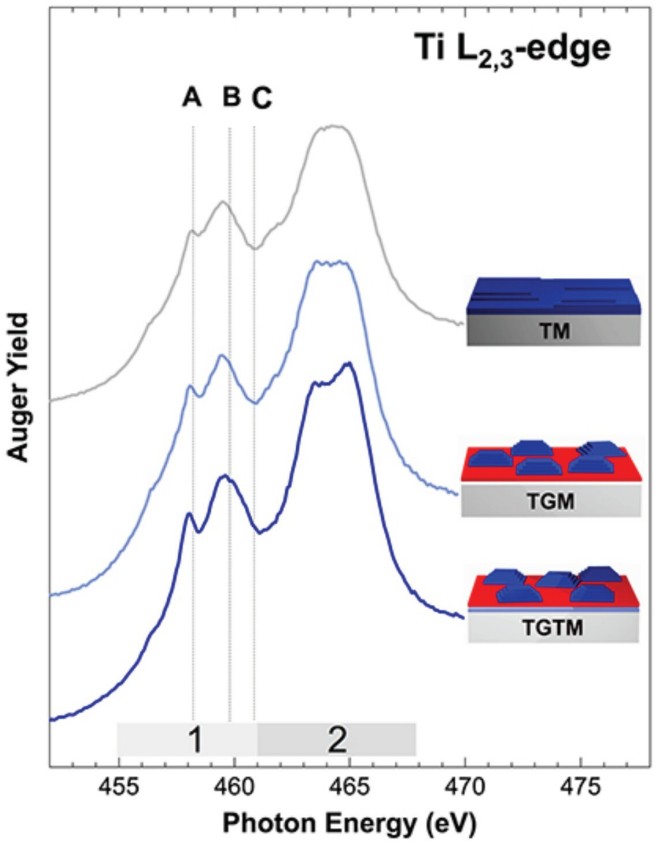

Figure 4.12: NEXAFS spectra measured at the Ti L_3 (region 1: 455-461 eV) and L_2 (region 2: 461-468 eV) absorption edges for the TM, TGM and TGTM nanoarchitectures. The energies at which the most prominent features A, B and C are usually found in the spectra of bulk titania samples are indicated with dotted lines.

The characterization of the interface composition was performed by high resolution photoelectron spectroscopy. In the Ti $2p$ spectra it is possible to discriminate the components generated by titanium atoms with different oxidation state, as already described in the previous section. By fitting each of them with a Doniach-Šunjić line profile convoluted with a Gaussian it is possible to quantitatively measure the relative amount of titanium species. Adding to this information the measurement of the O $1s$ spectral intensity allowed us to calculate the stoichiometry of the titanium oxide clusters and thin layer. The conclusion is also in this case identical for the three nanostructures. The main component of each spectrum at 459 eV is attributed to Ti^{4+} [41]. Titanium atoms are in the +4 oxidation state for a percentage that varies from 75 to 82% ($\pm$ 3%) of the total titanium amount. The titanium dioxide stoichiometry is

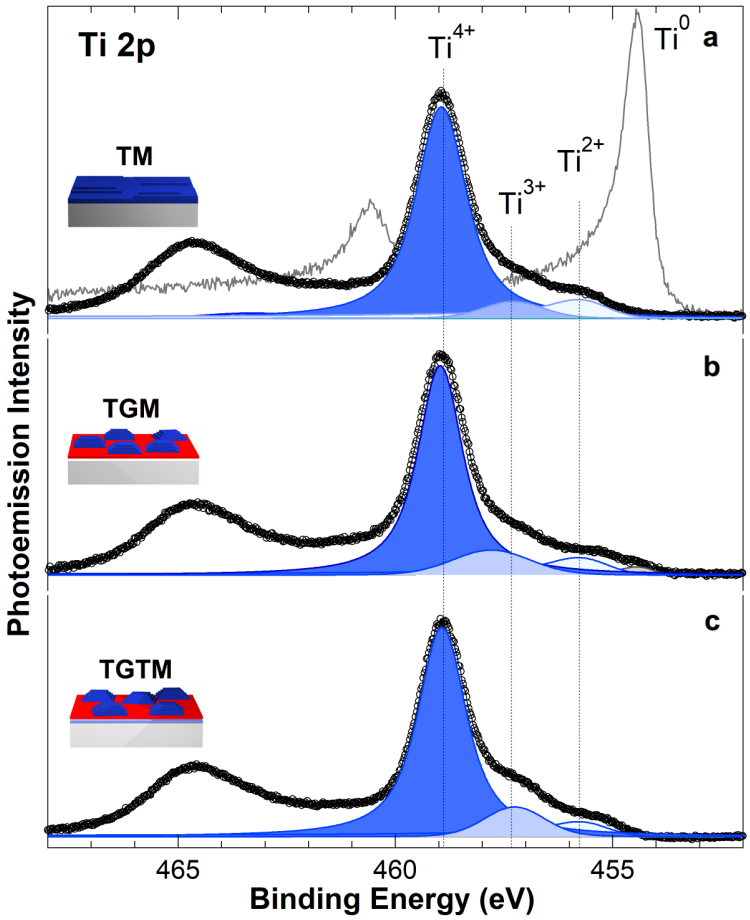

Figure 4.13: X-ray photoemission spectra of the Ti $2p$ for the three interfaces. The binding energies corresponding to 2+, 3+and 4+ components of the Ti $2p_{3/2}$ are 455.5, 457.7 and 459.0 eV respectively, while the Ti^0 component is found at 454.35 eV.

therefore confirmed, even if an amount of sub-oxide exists, as suggested by the presence of tiny amounts of atoms in Ti^{2+} and Ti^{3+} configuration. Titanium atoms with low oxidation state are expected to be present on the surface of both clusters and thin layer and their density is associated to the density of oxygen vacancies. Again, for the sake of a rigorous comparison among the three photocatalysts we measured with a more sensitive method the amount of these active sites. The measurements we performed, despite not being absolutely quantitative, allow a more accurate comparative quantification with respect to the standard core level XPS performed on Ti $2p$ or O $1s$ states.

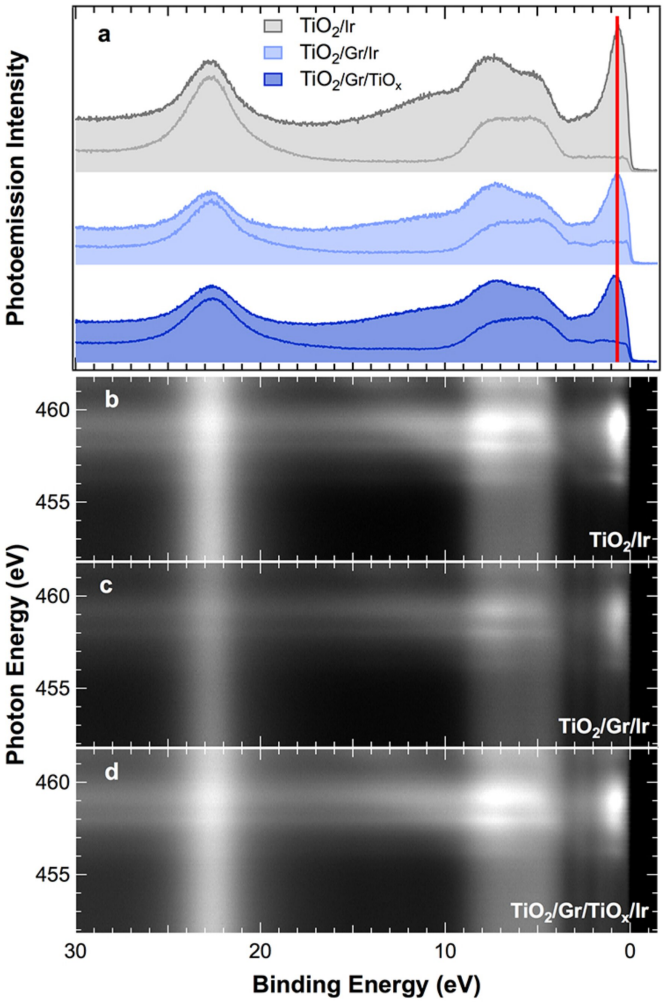

Figure 4.14: Valence band and resonant photoemission spectra on TM, TGM and TGTM systems. a) Valence band spectra acquired on and off resonance (458.8 eV and 451 eV photon energy respectively) at the Ti L_3-edge. Resonant photoemission spectroscopy data for a) TM, b) TGM, and c) TGTM, measured across Ti L_3-edge. The photoemission intensity is plotted in grayscale, dark representing lower photoemission intensity.

It is known that oxygen vacancies in TiO_2 can be investigated by resonant photoelectron spectroscopy in the valence band region [42]. Titanium atoms adjacent to oxygen vacancies, and therefore in a low oxidation state, have been recognized as the cause of a self-doping of titania that introduces defect states into the band gap of the material [20, 43]. These states are involved in a resonant photoemission process with electrons in the valence energy region. In presence of oxygen vacancies, for photon energies between 458 and 460 eV, a resonant enhancement is observed in the valence band for O $2s$ and O $2p$-Ti$3d$ hybridized states and for a narrow component at BE = 1.1 eV, whose intensity is directly proportional to the density of defects. We therefore compared the relative intensity of this feature in resonant condition with respect to the intensity of the hybridized states out of resonance. With an accuracy of 1%, no differences are appreciable among our interfaces, suggesting that the density of oxygen defects is the same for the clusters grown on the two substrate as well as for the titania layer.

The focus of the experimental characterization was therefore moved from titanium dioxide to graphene, with the aim of describing the differences between TGM and TGTM from the electronic point of view. C $1s$ core level photoemission spectra have been acquired and analysed to retrieve information about the graphene modification induced by clusters deposition. In figure 4.15 is reported a summary of the spectroscopic investigation. The spectrum relative to graphene on clean Ir (111) is reported as a reference; the single spectroscopic component at 284.12 eV is typical of the slightly p-doped graphene [44]. A shift of the C $1s$ component to higher binding energies is observed after the deposition of metallic titanium particles on Gr/Ir, along with a broadening of the photoemission component. A similar behaviour for the C $1s$ was observed by Palacios *et al.* [45] after the deposition of metallic titanium on SiC-supported graphene. This shift was interpreted as a consequence of a chemical hybridization between carbon and titanium. The oxidation of the supported particles reduces this shift, but the C $1s$ binding energy of TGM remains higher than that of Gr/Ir (284.27 eV), suggesting that a negative doping effect is induced on graphene by the titania particles.

For GTM, we have already shown that the intercalation of titanium oxide affects the graphene structure. After Ti oxide intercalation the C $1s$ photoemission peak appears shifted to low binding energies. The presence of metallic particles on GTM induces a shift of the C $1s$ peak from BE = 283.60 to 283.95 eV, while the cluster oxidation recovers partially this shift moving the binding energy to 283.81 eV. A major difference between the two architecture

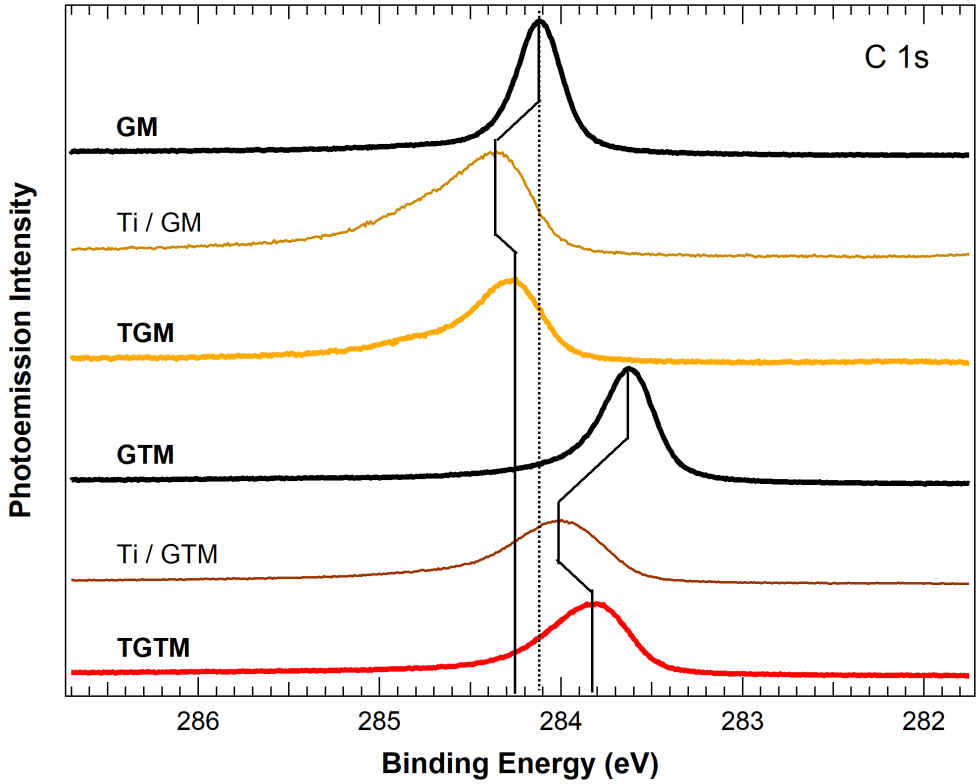

Figure 4.15: C 1*s* core level photoemission spectra acquires at 400 eV photon energy. The evolution of the C 1*s* component during the particles growth on the two substrates is marked by the black lines.

is therefore the doping condition of graphene, which is negative for TGM and positive for TGTM. The Lorentian width of the C 1*s* spectral component remains unchanged before and after the titanium deposition and oxidation, with a value of 0.18 eV, both for TGM and TGTM, while the asymmetry parameter increases from 0.14 to 0.19 eV after the Ti cluster growth and decreases back to the initial value after the oxidation. This means that the metallicity of graphene is significantly affected by the interaction with the supported clusters. In any case, the C 1*s* spectra can be fitted with one single component, suggesting the homogeneity of graphene electronic structure and therefore of the clusters distribution.

The graphene doping modifications described earlier are expected to change the electronic level of occupation of the supported clusters, modifying consequently their work function (WF). By photoelectron spectroscopy, we measured the value of this quantity for the interfaces we prepared (figure 4.16). The value reported for bulk anatase is 5.1 eV. While for titania on Ir (111) we measured

5.1 eV, for TGM we observe that this value is lower and stands between those of anatase and Gr/Ir, being the latter equal to 4.8 eV. A similar consideration can be done for the TGTM, where WF is higher than 5.1 eV and closer to the value of the GTM structure (5.2 eV). It is evident that the presence of a different supporting substrate affects the clusters work function, through a mechanism that reasonably involves a charge transfer between clusters and substrate, which is set by the doping state of graphene.

Large modifications in the electronic structure of titania for the different architectures have been confirmed at this point, although their effects on the photocatalytic activity are not easily predictable. Therefore, experimental measurements of the photocatalytic activity of different architectures have been performed at the Chemistry Department of the University of Trieste, in collaboration with Prof. Fornasiero.

Samples were transferred in air from SuperESCA to the Chemistry Department. The structural stability of the nanoparticles in ambient conditions were checked by STM, while the environmental contamination, substantially constituted by oxygen and water was not evaluated, since the subsequent photocatalytic measurements were performed in water solution.

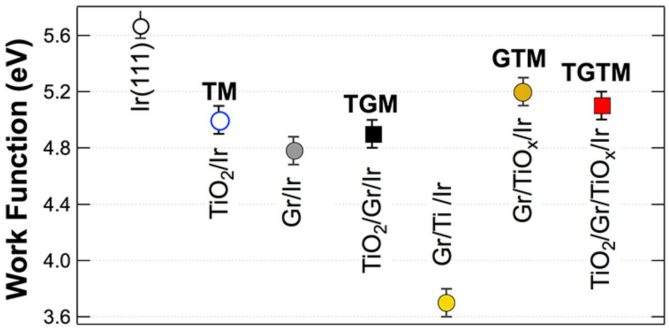

Figure 4.16: Summary of the work function values for the examined interfaces.

TM, TGM and TGTM systems were tested in a 1:1 water-methanol solution exposing them to simulated solar light and measuring the amount of hydrogen produced.

In order to measure the activity of TiO_2 for the hydrogen reduction (eq. 4.3), methanol was introduced as a sacrificial agent, since it can indeed be more easily oxidized by the photogenerated holes with respect to water and it prevents the partial back recombination of H_2 and O_2 that occurs in pure water splitting.

To simulate the solar irradiation a xenon lamp was employed, with an

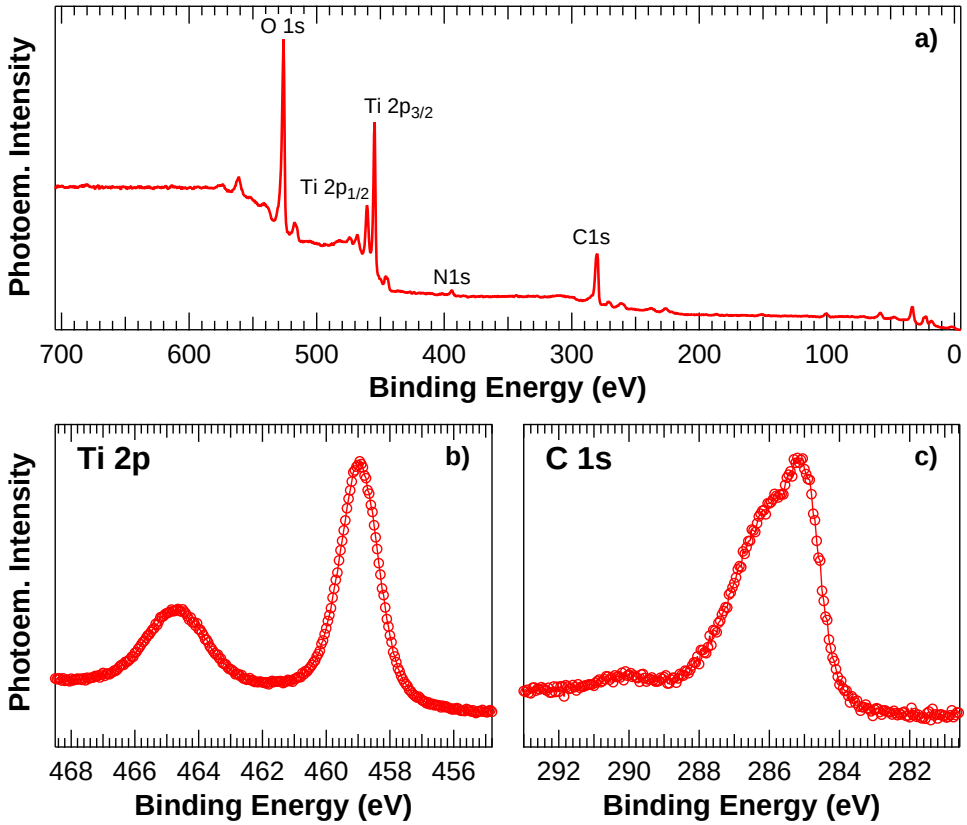

Figure 4.17: XPS measurements of the TiO_2/graphene powdered composite ($h\nu$ = 1253.6 eV). a) Survey spectrum, b) Ti $2p$ spectrum, c) C $1s$ spectrum.

atmospheric edge filter to eliminate UV radiation below 300 nm wavelenght. The light beam was focused on the sample, a 9 mm diameter disc, with a resulting light intensity of 25 mW/cm^2 in the 250-400 nm UV-visible region and 180 mW/cm^2 in the 400-1000 nm visible-near infrared region. These values are approximately equivalent to 2 Suns, which is a value typically obtained with a common solar concentrator. Samples were kept in a closed environment represented by a 20 ml vial with 12.5 ml solution. Air was substituted by argon, bubbling the pure noble gas in the solution before starting the irradiation. The analysis of the gas composition present inside the vial after the 20 hours exposition was performed by a gas chromatograph, quantifying the amount of hydrogen with a thermal conductivity detector using argon as a carrier gas. To perform a comparison between our systems and a commercial-derived TiO_2/Gr system in solution, a reference composite powder was also synthesized and characterized. It was obtained from commercial graphene material and $Ti(OBu)_4$ polymer. Polymers were dissolved in ethanol and graphene flakes

	TM	TGM	TGTM	TiO_2/Gr powder
H_2 production $\left(\frac{\text{mol } H_2}{\text{mol } TiO_2}\right)$	$(3.5 \pm 0.9) \times 10^{-2}$	$(1.03 \pm 0.08) \times 10^{-1}$	$(8.35 \pm 0.05) \times 10^{-1}$	$(1.28 \pm 0.02) \times 10^{-4}$

Table 4.1: Results of the photocatalytic measurement. The hydrogen amount is normalised to the amount of titanium actually present in each system.

were dispersed in the solution by ultrasound sonication. Hydrolisis of the titanium precursor was realized adding a solution of HNO_3, ethanol and H_2O, maintaining the graphene suspension by stirring until the formation of a gel. After 24 h at room temperature and 80 °C overnight drying, gel was finally calcinated at 300 °C for 6 hours to remove the inorganic residues.

The powder was then characterized with different techniques. By thermogravimetric analysis it was possible to estimate the amount of graphene, which results to be 4.9 wt% of the total composite photocatalyst. Raman spectroscopy indicates that the titanium dioxide so obtained is in the anatase form. XPS measurements of the compressed TiO_2/Gr powder were performed at the SSL laboratory, using the non-monochromatized Mg Kα X-ray source. Results are shown in figure 4.17. The Ti $2p$ spectrum presents one single component at about BE = 459 eV The C $1s$ signal presents various components, with the most intense ones attributed to sp^2-hybridized C atoms (BE = 285.4 eV) and to CO groups (BE = 286 eV). A small signal at 290 eV derives from carboxyl groups and from Ti–O–C interface [46]. This indicates that graphene is partially oxidized, with a high density of functional groups. The traces of N detected in the survey can also be attributed to impurities in graphene.

The results of the hydrogen production measurements are reported in table 4.1. By comparing the results, a ratio of about two orders of magnitude between the powder composite and TM system is observed. The efficiency of semiconductor-metal junctions in the enhancement of photocatalytic activity is indeed widely recognised and such a result was expected, at least qualitatively [47, 48]. More interesting is the activity enhancement obtained with graphene supported titania particles. The large difference between TM and TGM confirms the effectiveness of the graphene support in improving the photocatalytic activity, which is attributed to its capability to act as electron acceptor increasing the lifetime of the charge carriers [49]. It is worth noting that the mechanism proposed to describe the advantages in using graphene in

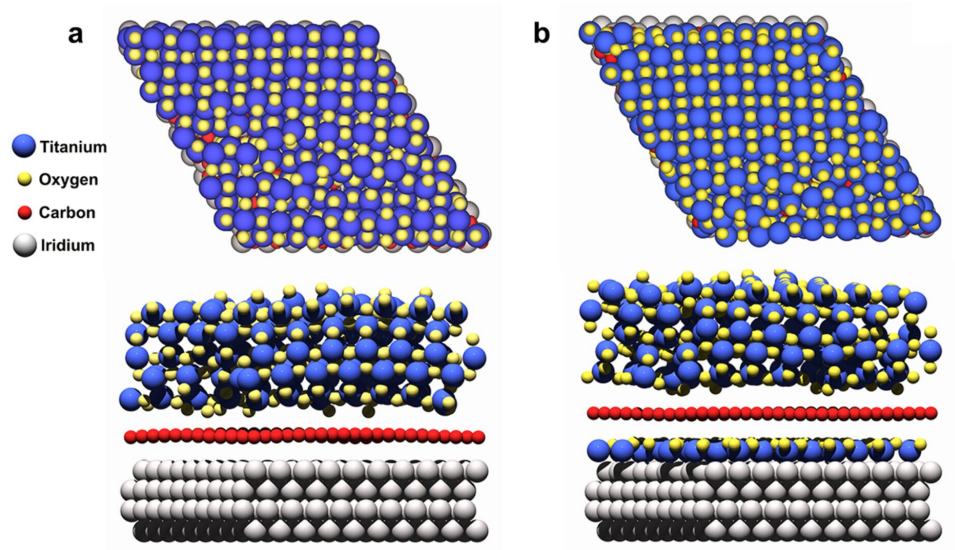

Figure 4.18: Structure of the TGM and TGTM nanoarchitectures corresponding to the (100) anatase TiO_2 surface termination from DFT calculations. a) Top and side view of the relaxed TGM supercell. b) Top and side view of the relaxed TGTM supercell.

association with TiO_2 requires a low density of defects and functional groups, in order to preserve its electronic properties, a condition hardly achievable through the application of graphene oxide reduction methodologies. The most remarkable result regards anyway the activity difference between TGM and TGTM. The system provided with the titanium oxide interfacial layer shows an activity eight times larger than the simple TiO_2/Gr/Ir. This appears as a clear experimental demonstration of the possibility to modify the chemical properties of solid supported nanoparticles through a modification of the electronic properties of the substrate.

To investigate the details of this effect we performed first principles calculations to get a description of the electronic structure of TGM and TGTM and possibly identify the mechanism behind the interface-driven photocatalytic activity enhancement. Density functional theory calculations have been selected as an effective way to identify the modifications on the partial densities of states for the two graphene-based interfaces. To perform this kind of calculations we designed the atomic supercells that could best describe the two nanostructures. For computational restriction, we described the particles interfaces as periodic crystals with a unit cell dimension comparable to that of the Gr/Ir (111) moiré lattice. Despite the moiré structure results from the experimentally observed

superposition of 10×10 graphene cells on 9×9 of Ir (111), we defined the lateral dimension of our TGM and TGTM supercells equal to 10×10 Ir (111) unit cells. In this way it was possible to accurately represent the 2×2 $TiO_{1.5}$ superstructure of the interface layer respect to the Ir (111) lattice, introducing at the same time a less than 1% strain in the graphene lattice.

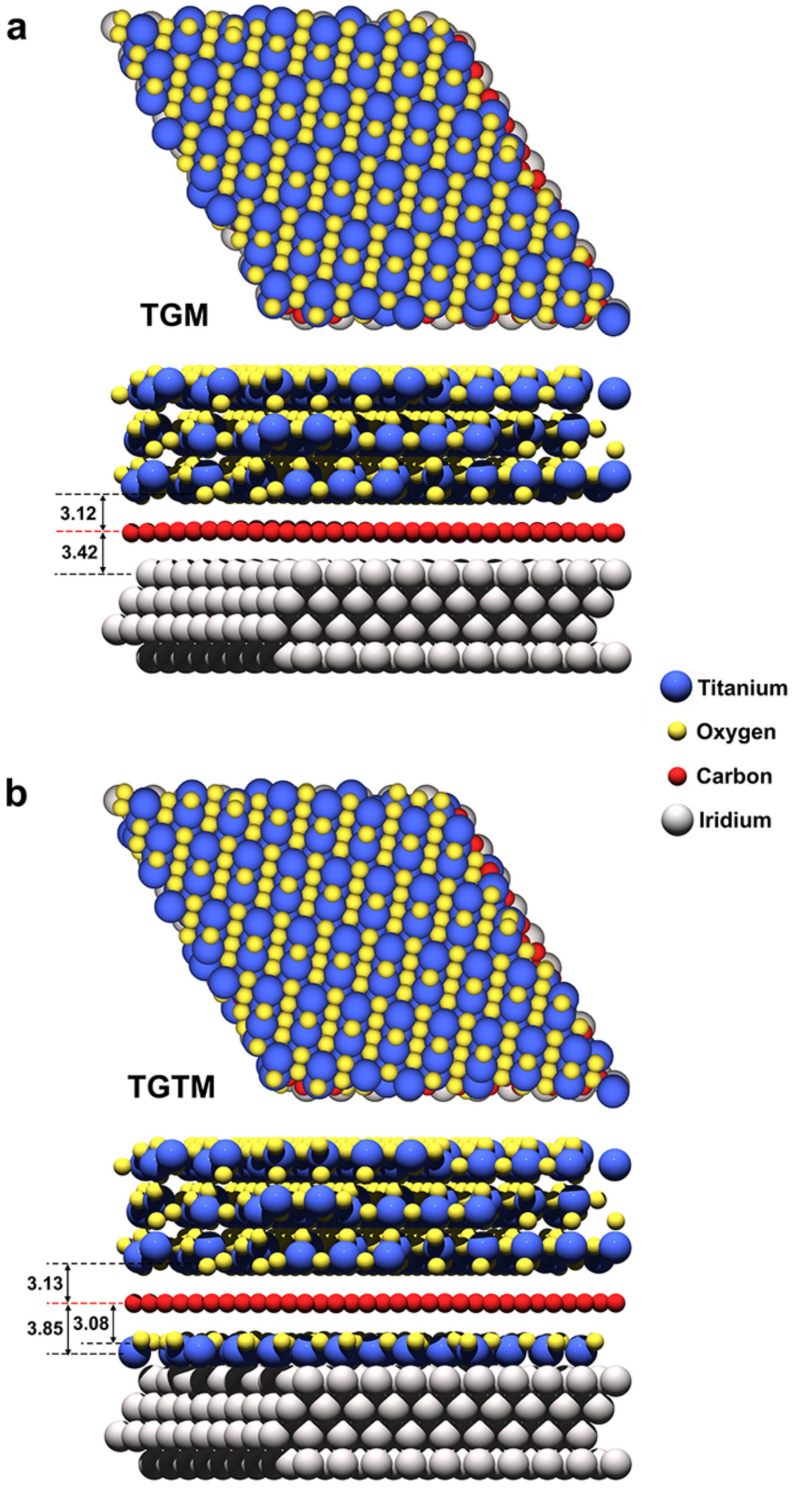

Figure 4.19: DFT calculation results for the geometric structure of the TGM (a) and TGTM (b) nanoarchitectures designed by aligning the anatase layers along the (101) crystallographic direction. The consideration made for the vanishing of the graphene corrugation in presence of the interfacial layer (see section 4.2.1) are valid also in presence of the supported TiO_2 layer. The average distance between titania and graphene is not significantly affected by the $TiO_{1.5}$ interface.

On these substrates, containing four iridium layers, graphene and $TiO_{1.5}$ interface in the case of TGTM, anatase TiO_2 was added in form of a layer containing an amount of Ti equivalent to 2 ML. Anatase was initially oriented to expose the (001) crystallographic plane. Preliminary structural calculations, shown in figure 4.18, pointed out the tendency of this TiO_2 surface to reconstruct [50], leading in our case to a disordered and unstable structure. The supported anatase layer was then modified rotating the lattice to align the surface to the (101) crystallographic plane, which proved to be energetically more stable, in agreement with the Wulff construction [51]. The thickness of the titania (101) layer was 9.70 Å, a value very close to the one measured by STM. The two sets of atomic coordinates, relative to more than thousand atoms for both TGM and TGTM, were set as free parameters for the simulated atomic relaxation, except for the bottom two iridium layers that were kept fixed to their bulk geometry with a lattice parameter of 2.74 Å. In order to accurately calculate the structural parameters, van der Waals interactions demonstrated to be essential, both for Gr/metals [52] and for Gr/TiO_2 interfaces [53]. The rev-vdw-DF2 functional was therefore used and the relaxation procedure has been run until the largest residual force was less than 0.015 eV/Å. The geometry obtained with this procedure are shown in figure 4.19 for the two structures.

On the basis of these structural results, the partial density of states was computed for carbon and for the titanium atoms constituting the TiO_2 layer (figure 4.20). For these calculation, the HSE06 hybrid functional was used, since it proved to be a reliable tool for the description of semiconductor band gaps and Gr–TiO_2 charge transfer [53]. Regarding titania, the calculated band gap results to be 3.2 eV both for TGM and TGTM, in good agreements with the optical band gap of anatase, measured at 4 K [54]. The most evident modification introduced by the titanium oxide interface on the electronic structure of titania is a shift of the Ti PDOS of about 0.5 eV to higher energies. The same shift is found for the graphene π and π^* bands, reflecting the p-doping effect of the interface experimentally observed through core level spectroscopy and work function measurements. Considering the Ti PDOS, a consequence of the shift is the presence of a zero density of state region above the Fermi level. The absence of free states extended for 0.5 eV above E_F could be the reason for a longer excited electron lifetime. In this condition, the minimum energy of a photoexcited electron will be 0.5 eV above the Fermi level. It has been shown that in anatase the radiative recombination of excited electron is suppressed [55], so in order for the electron in the Ti states to recombine through a non radiative process, it has to be involved in a multi-phonon process with a probability

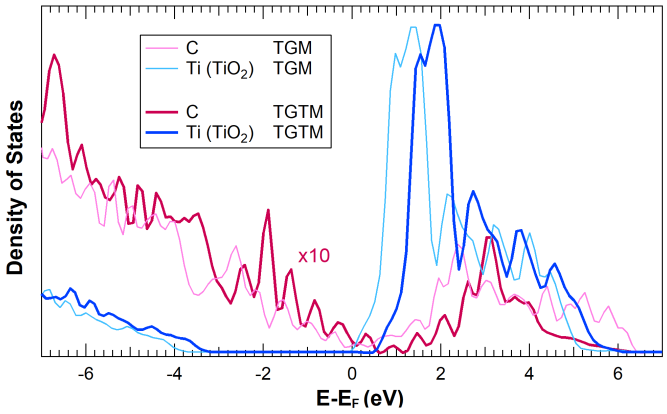

Figure 4.20: Calculated partial density of states of TGM (pink and light blue curves for carbon and titanium respectively) and TGTM (red and blue). The reported carbon PDOS is multiplied by a factor 10.

rapidly decreasing with the increasing extension of the zero PDOS region above E_F. The reduced recombination rate would determine a longer excited electron lifetime and consequently a higher photocatalytic activity.

A parallel cause for the activity enhancement in TGTM could be the increased carbon PDOS at the Fermi level due to the shift of the graphene Dirac cones, that would enhance the photon absorption efficiency of the system providing a higher density of initial states for the photoexcitation transition.

In summary, we demonstrated the possibility to change the photocatalytic properties of a nanoscaled material by modifying its supporting substrate. Through a multi-technique approach we characterized three nanostructured interfaces of titanium dioxide, in layered and nanoparticles form, which resulted to be indistinguishable for composition and local crystalline structure. Moreover, the morphology of the particles was observed to be the same for both graphene-based substrates. The electronic structure of the three systems was investigated in order to find the most significant differences among them, pointing out that while the energy band gap of titania remains unchanged for all the systems, the work function varies as a function of the substrate. Photocatalytic measurements showed an outstanding enhancement of the activity of titanium dioxide particles when supported by a p-doped graphene substrate, four orders of magnitude higher than a commercial reference system tested in solution and one order of magnitude higher than the same particles deposited on graphene/Ir (111). Possible explanations for this last observation were retrieved from DFT based calculations of the partial density of states

of the two systems, bringing to the conclusion that the activity enhancement is reasonably due to the larger electron hole lifetime achievable shifting the titanium electronic structure through the modification of the graphene charge transfer, defined, in turn, by its substrate.

This work demonstrates that the construction of tailored nanostructures is possible by exploiting the possibility to tune the properties of the clusters through the modification of their solid support. Furthermore, the method described above is not limited to the materials considered here, nor to the specific photocatalytic water splitting process, but could be generally applied to a variety of catalytic applications. In this perspective we investigated similar nanoarchitectures based on different metal oxides.

References

[1] Weir, A.; Westerhoff, P.; Fabricius, L.; Hristovski, K.; Von Goetz, N. Titanium dioxide nanoparticles in food and personal care products. *Environmental Science & Technology* **46**, 2242 (2012).

[2] Hagfeldt, A.; Boschloo, G.; Sun, L.; Kloo, L.; Pettersson, H. Dye-sensitized solar cells. *Chemical Reviews* **110**, 6595 (2010).

[3] Chu, L.; Qin, Z.; Yang, J. Anatase TiO_2 nanoparticles with exposed {001} facets for efficient dye-sensitized solar cells. *Scientific Reports* **5**, 12143 (2015).

[4] Hashimoto, K.; Irie, H.; Fujishima, A. TiO_2 photocatalysis: a historical overview and future prospects. *Japanese Journal of Applied Physics* **44**, 8269 (2005).

[5] Kato, S.; Mashio, F. Autooxidation by TiO_2 as a photocatalyst. *Abtr. Book Annu. Meet Chemical Society of Japan* **223**, (1956).

[6] Fujishima, A.; Honda, K. Electrochemical photolysis of water at a semiconductor electrode. *Nature* **238**, 37 (1972).

[7] Ma, G.; Hisatomi, T.; Domen, K. *From Molecules to Materials*; Springer, 2015.

[8] Hisatomi, T.; Kubota, J.; Domen, K. Recent advances in semiconductors for photocatalytic and photoelectrochemical water splitting. *Chemical Society Reviews* **43**, 7520 (2014).

[9] Ma, Y.; Wang, X.; Jia, Y.; Chen, X.; Han, H.; Li, C. Titanium dioxide-based nanomaterials for photocatalytic fuel generations. *Chemical Reviews* **114**, 9987 (2014).

[10] Fujishima, A.; Rao, T. N.; Tryk, D. A. Titanium dioxide photocatalysis. *Journal of Photochemistry and Photobiology C: Photochemistry Reviews* **1**, 1 (2000).

[11] Fujishima, A.; Zhang, X. Titanium dioxide photocatalysis: present situation and future approaches. *Comptes Rendus Chimie* **9**, 750 (2006).

[12] Nishimoto, S.; Ohtani, B.; Kajiwara, H.; Kagiya, T. Correlation of the crystal structure of titanium dioxide prepared from titanium tetra-2-propoxide

with the photocatalytic activity for redox reactions in aqueous propan-2-ol and silver salt solutions. *Journal of the Chemical Society, Faraday Transactions 1: Physical Chemistry in Condensed Phases* **81**, 61 (1985).

[13] Sclafani, A.; Palmisano, L.; Schiavello, M. Influence of the preparation methods of titanium dioxide on the photocatalytic degradation of phenol in aqueous dispersion. *Journal of Physical Chemistry* **94**, 829 (1990).

[14] Fox, M. A.; Dulay, M. T. Heterogeneous photocatalysis. *Chemical Reviews* **93**, 341 (1993).

[15] Banfield, J. Thermodynamic analysis of phase stability of nanocrystalline titania. *Journal of Materials Chemistry* **8**, 2073 (1998).

[16] Zhang, H.; Banfield, J. F. Understanding polymorphic phase transformation behavior during growth of nanocrystalline aggregates: insights from TiO_2. *The Journal of Physical Chemistry B* **104**, 3481 (2000).

[17] Naicker, P. K.; Cummings, P. T.; Zhang, H.; Banfield, J. F. Characterization of titanium dioxide nanoparticles using molecular dynamics simulations. *The Journal of Physical Chemistry B* **109**, 15243 (2005).

[18] Thompson, T. L.; Yates, J. T. Surface science studies of the photoactivation of TiO_2 new photochemical processes. *Chemical Reviews* **106**, 4428 (2006).

[19] Thompson, T. L.; Yates, J. T. Control of a surface photochemical process by fractal electron transport across the surface: O_2 photodesorption from TiO_2 (110). *The Journal of Physical Chemistry B* **110**, 7431 (2006).

[20] Caruso, T.; Lenardi, C.; Mazza, T.; Policicchio, A.; Bongiorno, G.; Agostino, R.; Chiarello, G.; Colavita, E.; Finetti, P.; Prince, K. Photoemission investigations on nanostructured TiO_2 grown by cluster assembling. *Surface Science* **601**, 2688 (2007).

[21] Petrik, N. G.; Kimmel, G. A. Reaction kinetics of water molecules with oxygen vacancies on rutile TiO_2 (110). *The Journal of Physical Chemistry C* **119**, 23059 (2015).

[22] Verma, R.; Samdarshi, S. Correlating oxygen vacancies and phase ratio/interface with efficient photocatalytic activity in mixed phase TiO_2. *Journal of Alloys and Compounds* **629**, 105 (2015).

[23] Leary, R.; Westwood, A. Carbonaceous nanomaterials for the enhancement of TiO_2 photocatalysis. *Carbon* **49**, 741 (2011).

[24] Xiang, Q.; Yu, J.; Jaroniec, M. Graphene-based semiconductor photocatalysts. *Chemical Society Reviews* **41**, 782 (2012).

[25] Liang, Y.; Wang, H.; Casalongue, H. S.; Chen, Z.; Dai, H. TiO_2 nanocrystals grown on graphene as advanced photocatalytic hybrid materials. *Nano Research* **3**, 701 (2010).

[26] Zhang, Y.; Tang, Z.-R.; Fu, X.; Xu, Y.-J. Engineering the unique 2D mat of graphene to achieve graphene-TiO_2 nanocomposite for photocatalytic selective transformation: what advantage does graphene have over its forebear carbon nanotube? *ACS Nano* **5**, 7426 (2011).

[27] Zhang, H.; Lv, X.; Li, Y.; Wang, Y.; Li, J. P25-graphene composite as a high performance photocatalyst. *ACS Nano* **4**, 380 (2009).

[28] An, X.; Jimmy, C. Y. Graphene-based photocatalytic composites. *RSC Advances* **1**, 1426 (2011).

[29] Zhang, Y.; Tang, Z.-R.; Fu, X.; Xu, Y.-J. TiO_2- graphene nanocomposites for gas-phase photocatalytic degradation of volatile aromatic pollutant: is TiO_2- graphene truly different from other TiO_2- carbon composite materials? *ACS Nano* **4**, 7303 (2010).

[30] Alfe, D.; Pozzo, M.; Miniussi, E.; Günther, S.; Lacovig, P.; Lizzit, S.; Larciprete, R.; Burgos, B. S.; Menteş, T.; Locatelli, A.; Baraldi, A. Fine tuning of graphene-metal adhesion by surface alloying. *Scientific Reports* **3**, 2430 (2013).

[31] Ma, Y.; Travaglia, E.; Bana, H.; Bignardi, L.; Lacovig, P.; Lizzit, S.; Batzill, M. Periodic Modulation of Graphene by a 2D-FeO/Ir (111) Moiré Interlayer. *The Journal of Physical Chemistry C* **121**, 2762 (2017).

[32] Presel, F.; Jabeen, N.; Pozzo, M.; Curcio, D.; Omiciuolo, L.; Lacovig, P.; Lizzit, S.; Alfe, D.; Baraldi, A. Unravelling the roles of surface chemical composition and geometry for the graphene–metal interaction through C1s core-level spectroscopy. *Carbon* **93**, 187 (2015).

[33] Larciprete, R.; Ulstrup, S.; Lacovig, P.; Dalmiglio, M.; Bianchi, M.; Mazzola, F.; Hornekær, L.; Orlando, F.; Baraldi, A.; Hofmann, P.; Lizzit, S.

Oxygen switching of the epitaxial graphene–metal interaction. *ACS Nano* **6**, 9551 (2012).

[34] Omiciuolo, L.; Hernández, E. R.; Miniussi, E.; Orlando, F.; Lacovig, P.; Lizzit, S.; Menteş, T. O.; Locatelli, A.; Larciprete, R.; Bianchi, M.; Ulstrup, S.; Hofmann, P.; Alfè, D.; Baraldi, A. Bottom-up approach for the low-cost synthesis of graphene-alumina nanosheet interfaces using bimetallic alloys. *Nature Communications* **5**, 5062 (2014).

[35] Biesinger, M. C.; Lau, L. W.; Gerson, A. R.; Smart, R. S. C. Resolving surface chemical states in XPS analysis of first row transition metals, oxides and hydroxides: Sc, Ti, V, Cu and Zn. *Applied Surface Science* **257**, 887 (2010).

[36] Barcaro, G.; Agnoli, S.; Sedona, F.; Rizzi, G. A.; Fortunelli, A.; Granozzi, G. Structure of reduced ultrathin TiO_x polar films on Pt (111). *The Journal of Physical Chemistry C* **113**, 5721 (2009).

[37] Klapetek, P.; Nečas, D.; Anderson, C. *Gwyddion User Guide*; 2009; p 54.

[38] Ruus, R.; Kikas, A.; Saar, A.; Ausmees, A.; Nommiste, E.; Aarik, J.; Aidla, A.; Uustare, T.; Martinson, I. Ti $2p$ and O $1s$ X-ray absorption of TiO_2 polymorphs. *Solid State Communications* **104**, 199 (1997).

[39] Diebold, U.; Ruzycki, N.; Herman, G. S.; Selloni, A. One step towards bridging the materials gap: surface studies of TiO_2 anatase. *Catalysis Today* **85**, 93 (2003).

[40] Ranade, M.; Navrotsky, A.; Zhang, H.; Banfield, J.; Elder, S.; Zaban, A.; Borse, P.; Kulkarni, S.; Doran, G.; Whitfield, H. Energetics of nanocrystalline TiO_2. *Proceedings of the National Academy of Sciences* **99**, 6476 (2002).

[41] Biesinger, M. C.; Payne, B. P.; Grosvenor, A. P.; Lau, L. W.; Gerson, A. R.; Smart, R. S. C. Resolving surface chemical states in XPS analysis of first row transition metals, oxides and hydroxides: Cr, Mn, Fe, Co and Ni. *Applied Surface Science* **257**, 2717 (2011).

[42] Bertel, E.; Stockbauer, R.; Madey, T. E. Resonant electron emission in Ti and TiO_2. *Physical Review B* **27**, 1939 (1983).

[43] Das, C.; Richter, M.; Tallarida, M.; Schmeißer, D. Electronic properties of atomic layer deposition films, anatase and rutile TiO_2 studied by resonant

photoemission spectroscopy. *Journal of Physics D: Applied Physics* **49**, 275304 (2016).

[44] Pletikosić, I.; Kralj, M.; Pervan, P.; Brako, R.; Coraux, J.; N'Diaye, A.; Busse, C.; Michely, T. Dirac cones and minigaps for graphene on Ir (111). *Physical Review Letters* **102**, 056808 (2009).

[45] Hsu, A. L.; Koch, R. J.; Ong, M. T.; Fang, W.; Hofmann, M.; Kim, K. K.; Seyller, T.; Dresselhaus, M. S.; Reed, E. J.; Kong, J.; Palacios, T. Surface-induced hybridization between graphene and titanium. *ACS Nano* **8**, 7704 (2014).

[46] Johra, F. T.; Lee, J.-W.; Jung, W.-G. Facile and safe graphene preparation on solution based platform. *Journal of Industrial and Engineering Chemistry* **20**, 2883 (2014).

[47] Chen, X.; Shen, S.; Guo, L.; Mao, S. S. Semiconductor-based photocatalytic hydrogen generation. *Chemical Reviews* **110**, 6503 (2010).

[48] Wang, H.; Zhang, L.; Chen, Z.; Hu, J.; Li, S.; Wang, Z.; Liu, J.; Wang, X. Semiconductor heterojunction photocatalysts: design, construction, and photocatalytic performances. *Chemical Society Reviews* **43**, 5234 (2014).

[49] Xiang, Q.; Yu, J.; Jaroniec, M. Enhanced photocatalytic H_2-production activity of graphene-modified titania nanosheets. *Nanoscale* **3**, 3670 (2011).

[50] Lazzeri, M.; Selloni, A. Stress-driven reconstruction of an oxide surface: the anatase TiO_2 (001)-(1×4) surface. *Physical Review Letters* **87**, 266105 (2001).

[51] Gong, X.; Selloni, A.; Batzill, M.; Diebold, U. Steps on TiO_2 anatase (101). *Nature Materials* **5**, 665 (2006).

[52] Miniussi, E.; Pozzo, M.; Baraldi, A.; Vesselli, E.; Zhan, R.; Comelli, G.; Menteş, T.; Niño, M.; Locatelli, A.; Lizzit, S.; Alfè, D. Thermal stability of corrugated epitaxial graphene grown on Re (0001). *Physical Review Letters* **106**, 216101 (2011).

[53] Ferrighi, L.; Fazio, G.; Valentin, C. D. Charge carriers separation at the graphene/(101) anatase TiO_2 interface. *Advanced Materials Interfaces* **3**, 1500624 (2016).

[54] Tang, H.; Levy, F.; Berger, H.; Schmid, P. Urbach tail of anatase TiO_2. *Physical Review B* **52**, 7771 (1995).

[55] Yamada, Y.; Kanemitsu, Y. Determination of electron and hole lifetimes of rutile and anatase TiO_2 single crystals. *Applied Physics Letters* **101**, 133907 (2012).

Chapter 5

Iron oxide-graphene interfaces

The search for a low-cost metallic photocatalyst has identified iron as a potential, effective candidate for the task. It is the fourth most abundant element in the Earth's crust in terms of parts per million and the first in terms of mass [1]. As a straightforward consequence, considering also the efficiency of its industrial production, it is one of the less expensive metals available. Despite its use is mostly related to metallurgy, the chemical properties of iron and iron compounds are widely exploited in organic and inorganic chemistry applications as well as in biology and medicine.

In the field of inorganic chemistry, iron has been used extensively for its catalytic activity since long time. Fe and Fe-oxides are indeed efficient catalysts in two of the historically most important catalytic reactions. The first one in chronological order, is the Haber–Bosch process, that can be briefly summarized in the production of ammonia from hydrogen and nitrogen; it was developed at the beginning of the 20^{th} century and still used nowadays for the production of fertilizers. The second one, also extremely important, is the Fischer–Tropsch process, that is a collection of chemical reactions that converts a mixture of carbon monoxide and hydrogen into liquid hydrocarbons [2].

Relatively to the photocatalytic properties, iron oxides were largely investigated since 1980's, mostly focusing the attention on the hydrogen production by water splitting, on the basis of the results reported few years before regarding the titanium dioxide [3, 4]. Among the existent iron oxides, Fe_2O_3, the most common form in nature, has been the most studied for this kind of applications, especially in its α form (hematite).

The activity of iron oxides, independently from stoichiometry and polymorphic phase, resulted to be sensibly lower with respect that of TiO_2. This

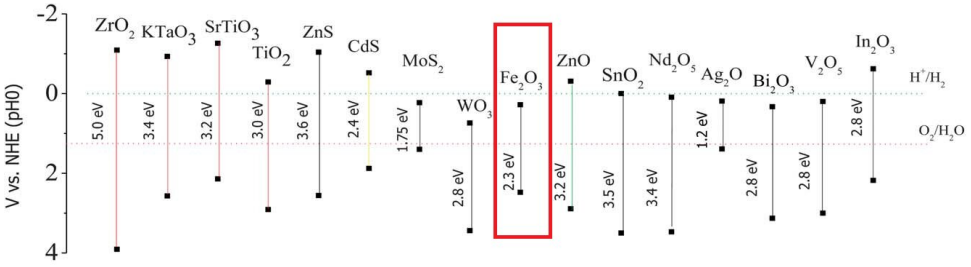

Figure 5.1: Band gap values and position of the most common metal-oxide and metal-sulfide semiconductors, referred to the Normal Hydrogen Electrode potential. Image reproduced from [8].

low activity has been ascribed to the particularly short mean free path of photoexcited charges in the material (about 20 nm [5]) and the subsequently high recombination rate of the electron-hole pairs created within the light penetration depth (of the order of 100 nm at 500 nm wavelength [6]). On the basis of these observation, Kay *et al.* [7] proposed a nanostructured Fe_2O_3 photoelectrode constituted by a stacking of thin iron oxide films separated by conductive SnO_2 glass. With this architecture they managed to obtain an unprecedented efficiency.

Fe_2O_3, despite having a favourable band gap value for the photocatalytic water splitting, has not been considered as promising as titanium dioxide. In fact, in addition to the short mean free path of the photoexcited charges, the position of the band gap with respect to the water splitting reaction potential is not ideally suitable, since the potential of the conduction band is lower that the hydrogen reduction potential (see image 5.1).

Nevertheless, attempts to obtain an efficient photocatalyst were performed improving the nanostructuring of iron oxide-base photocatalyst by the association with different materials as titanium dioxide [9, 10] and other semiconductors [8, 11]. Iron oxide semiconductor heterostructures were indeed introduced to exploit the built-in potential at the interface to promote the separation of the photogenerated charges. Another effect obtained using semiconductor heterojunction is the improvement in light harvesting: Fe_2O_3 was used to sensitize wider band gap semiconductors and improve the light absorption, as for example in the WO_3-Fe_2O_3 structure reported by Sivula *et al.* [12]. Further composite photocatalysts were obtained by association of iron oxide with metallic or metal-oxide co-catalysts to suppress charge recombination and improve therefore its catalytic activity, as Co and Mn [13] or IrO_2 [14].

Unlike the case of titanium dioxide, few experimental investigations report

about the association of Fe_2O_3, and other iron oxides, with graphene. This could be attributed to the fact that iron oxide is usually considered a secondary constituent of photocatalytic heterostructures. An example of Fe_2O_3/Gr structure is reported by Hou *et al.* [15]. They synthesized and characterized a ternary nanocomplex formed by α-Fe_2O_3 nanorod/graphene/Mo-doped $BiVO_4$, where the nanorods constitute the core of the complex and graphene stands as an interlayer between the iron oxide core and the Mo-doped $BiVO_4$ shell. In this heterostructure iron oxide is used to enhance the light harvesting due to its small band gap. In addition, its association with graphene results to be an effective way to increase the charge carriers mobility. Moreover, the heterojunction induces a shift of the two oxides bands with the final result of a fourfold photocatalytic activity with respect to Fe_2O_3.

In this chapter we are going to discuss an alternative way to obtain similar electronic effects and possibly further improved photocatalytic activity, exploiting the possibility offered by graphene-based substrates.

5.1 Sandwiched Fe-oxide/graphene architectures

We grew and characterized Fe-oxide nanoparticles supported by Gr/Ir (111) (FGM) and we compared them with Fe-oxide NPs deposited on Gr/Fe-oxide/Ir (111) (FGFM), in analogy with the sandwiched titanium-dioxide architectures described in the previous chapter. Our goal was to find an efficient method to change the electronic properties of Fe-oxide NPs for photocatalytic application through the interaction with the Gr-based support. Fe-oxide/Ir (111) (FM) was characterized in parallel as a reference system. The description of our experimental work begins with a section dedicated to the growth and characterization of the iron oxide thin-layer intercalated below graphene for the FGFM architecture and its comparison with a similar thin-layer grown on Ir (111). The following section will be then dedicated to the supported Fe-oxide nanoparticles.

The experimental procedures described in this chapter were performed at the SuperESCA beamline, except for the STM measurements performed at the CoSMoS end station.

5.1.1 Interfacial iron oxide

For the creation of the FGFM nanostructure, we grew a thin layer of Fe-oxide below graphene with the same requirements imposed for the intercalated titanium oxide, i.e. graphene integrity after the intercalation process and complete modification of the Gr/Ir (111) interface. The Fe-oxide growth was performed in two steps: metallic Fe deposition first and oxidation afterwards. For Fe deposition we used a filament evaporator, capable of depositing Fe vapours sublimated by a high purity filament with a rate of few ML/h at a pressure of the order of 10^{-10} mbar. The Fe intercalation at the Gr/Ir (111) interface was already reported in literature. Intercalation temperatures ranging from 600 [16] to 700 K [17] were used, as well as different techniques where the sample was either kept at high temperature during the Fe vapour exposure or it was annealed after Fe deposition performed at room temperature. We adopted the latter strategy, annealing the sample at 600 K after the room temperature deposition.

The necessary amount of intercalated metal was determined preliminarily by performing successive intercalation of sub-monolayer quantities of iron, and acquiring time-resolved XPS measurements of the C $1s$ and Ir $4f_{7/2}$ during the annealing. As described in section 3.3, we iterated the intercalation procedure until the complete suppression of the $4f_{7/2}$ surface component. A refinement on the annealing temperature has been done lowering it to 570 K to preserve the quality of graphene and allowing at the same time the complete Fe intercalation. The Fe coverage necessary for the creation of our Gr/Fe-oxide/Ir (111) (GFM) interface resulted to be (0.5±0.1) ML. Data displayed in figure 5.2 are related to the iron intercalation obtained through a single Fe deposition.

Regarding the first step of the intercalation process, i.e. the Fe deposition at room temperature on top of Gr, C $1s$ spectra acquired before and after the Fe deposition are reported in figure 5.3a and b, along with all other spectra relative to each stage of the intercalation process. No significant changes are observed for the line shape and the binding energy of the single component at 284.11 eV, apart from the attenuation of the photoemission signal due to the screening effect of Fe atoms on the C $1s$ photoelectrons. A new small component around 284.89 eV is observed; this component could be reasonably attributed to C atoms strongly interacting with Fe at the Gr defects.

On the other hand, a screening effect is observed on the Ir photoemission signal (not reported here) which does not show modification regarding neither the binding energies of the bulk and surface components nor their spectral

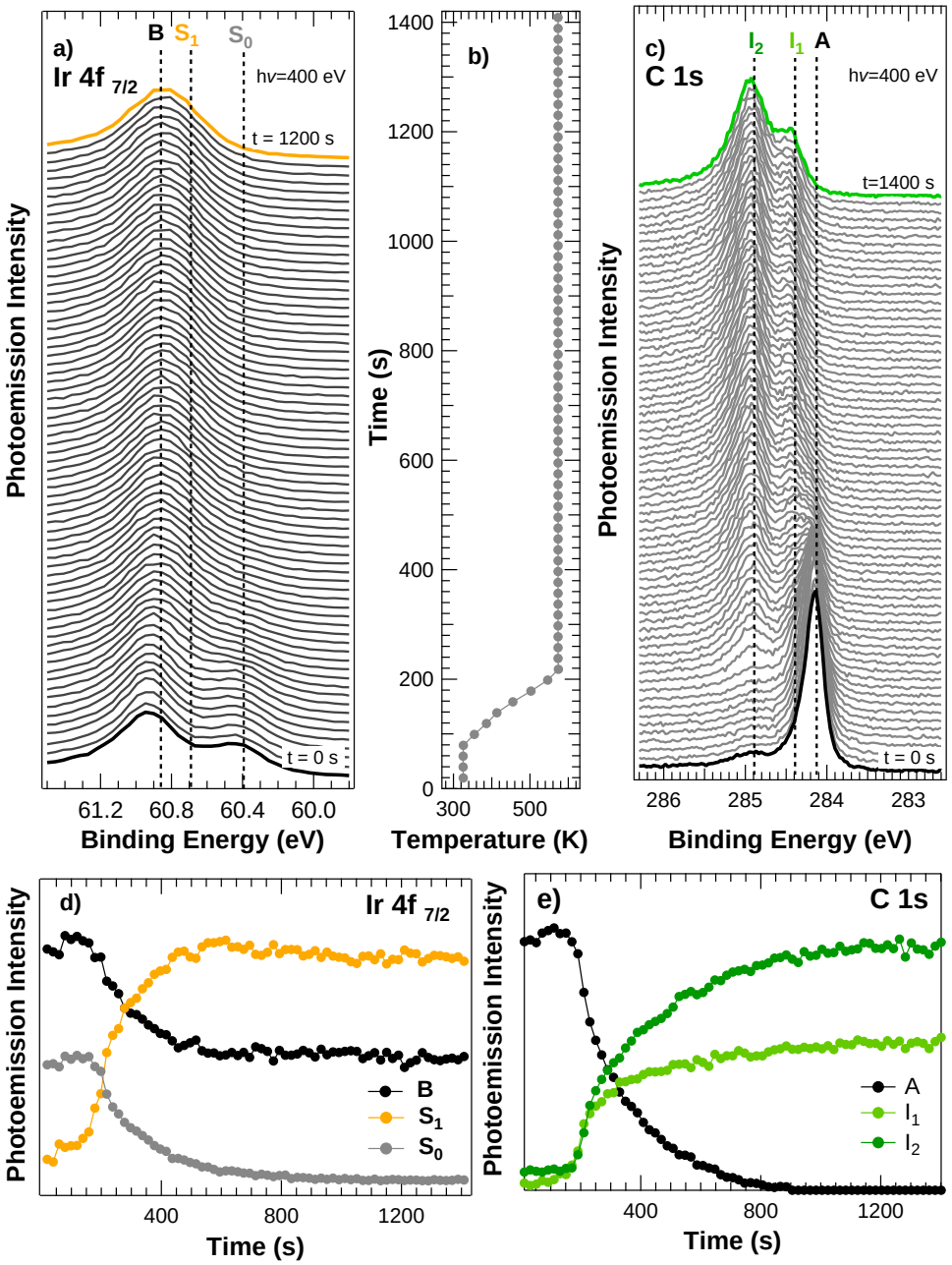

Figure 5.2: Time resolved photoemission spectra of a) Ir $4f_{7/2}$ and c) C $1s$, acquired during the intercalation. b) Temperature of the sample during the intercalation procedure as a function of time. The intensity of each photoemission component is plotted as a function of time for d) Ir $4f_{7/2}$ and e) C $1s$;

weight ratio, suggesting the absence of any significant amount of intercalated iron. Major modifications of these two spectra are observed however during

the annealing. The temperature of the sample was raised progressively with a rate of about 2 K/s and then kept fixed until no further spectral variations were appreciable.

For the time evolution analysis of the XPS spectra, a remark is needed regarding the photoemission signal intensity. A general signal enhancement is indeed measured at the beginning of the process for the Ir $4f_{7/2}$ (fig. 5.2a); this can be attributed to the effect of the field generated by the heating filament placed behind the sample. Therefore the trend of the photoemission intensity of each spectroscopic component can be considered fully reliable just after the end of the temperature ramp (fig. 5.2b), when the current flowing through the heating filaments gets stabilized. Focusing on the time evolution of the Ir $4f_{7/2}$ spectrum, a decrease in the total signal is detected during the intercalation after reaching 570 K. The surface (S_0) and bulk (B) components decrease with a similar rate for the first minutes. Then the S_0 component, that was preserved by the low-interacting graphene layer, disappears progressively, while a new surface component S_1 grows. After 15 minuted from the end of the temperature ramp, the decay of the total intensity stops, as well as the evolution of all the single components, meaning that the intercalation process is complete and, on the other hand, iron is not diffusing inside the crystal. A bulk diffusion phenomenon, in fact, would have led to a recovery of the S_0 intensity.

Regarding the evolution of the C 1*s* spectrum (fig. 5.2c), we observed the enhancement of the 284.89 eV binding energy component (labelled I_2) and the appearance of a new one at 284.39 eV (I_1). At the same time the component at 284.11 eV (A) decreases in intensity until vanishing. No shift is observed for A during the intercalation, suggesting that, unlike Ti, Fe tends to form islands below Gr.

The high resolution C 1*s* spectrum acquired after the intercalation is reported in figure 5.3c. The presence of spectral components at higher binding energy with respect to A (figure 5.2c) suggests a stronger interaction with graphene, as for the case of graphene on Fe (110) [18]. Moreover, Fe is known to grow pseudomorphic on Ir (111) when it is intercalated [17], therefore the moiré superstructure is preserved and the corrugation is enhanced. For this reason strongly and weakly interacting carbon species are present in the supercell, giving rise to a two-peak photoemission components distribution, similarly to what happen for titanium and other strongly interacting substrates as Re, Ru and Rh [19, 20]. The Lorentzian width (0.13 eV) and asymmetry parameter (0.08) found for the Gr/Ir (111) spectrum were used as initial values for the fit of the other photoemission components. No significant differences emerged

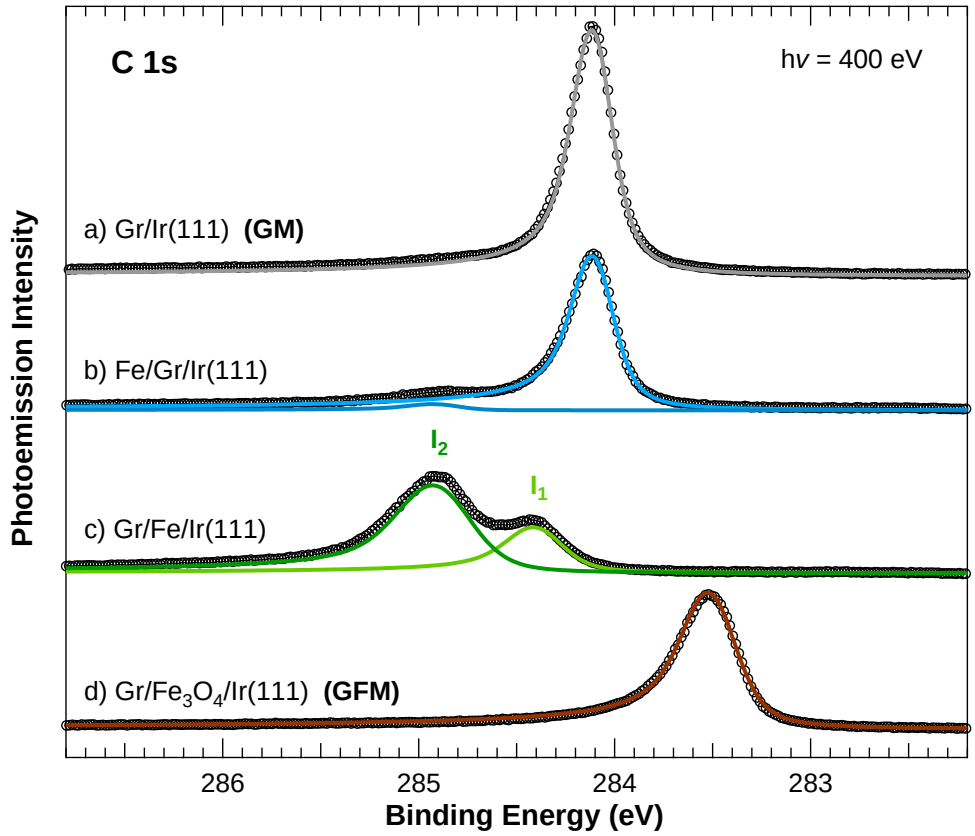

Figure 5.3: High resolution photoemission spectra acquired at 400 eV photon energy for a) Gr/Ir (111) (GM), b) after Fe deposition, c) after intercalation and d) after oxidation (GFM).

from the numerical fitting procedure for the Lorentzian value, while an enhancement of the metallicity of graphene is suggested by the asymmetry parameter, which results 0.14 for both I_1 and I_2; this is compatible with the fact that graphene is strongly interacting with the Fe substrate. The Gaussian width (0.16 eV for A) results to be greater for I_1 and I_2 (0.25 and 0.35 eV, respectively) due to the presence of chemically non-equivalent C atoms in the strongly and weakly interacting areas of the moiré supercell. The observed evolution of both Ir $4f_{7/2}$ and C $1s$ spectra confirmed the effective intercalation of iron, therefore we proceeded with the oxidation of the Fe layer.

The oxidation procedure we used is the same we applied for the oxidation of intercalated Ti and Co. Temperature, pressure and total O_2 exposure are parameters related to the intercalation of oxygen through graphene and they appear to be independent from the intercalated metallic species [21, 22]. Indeed,

the oxidation of iron below graphene was successfully achieved by exposing the sample to O_2 for 1 h at 570 K by means of a gas doser; the oxygen pressure measured in the experimental chamber was 1×10^{-4} mbar, correspondent to 5×10^{-3} mbar on the sample, which means a total exposure of 1.8×10^{7} L.

The C 1*s* spectrum acquired after the oxidation is displayed in fig.5.3 (GFM). The spectrum is characterized by a single sharp component at 283.50 eV, with 0.13 eV Lorentian and 0.25 eV Gaussian width. The C 1*s* binding energy is therefore lower than that of graphene, indicating a marked charge transfer from graphene to the substrate (p-doping). Interestingly, the asymmetry parameter of the single component used to fit the spectrum is equal to 0.14, larger than that of Gr/Ir (111), which indicates an enhancement in the metallicity of the graphene layer, which is compatible with the doping. The presence of a single components suggests also that the moiré corrugation, enhanced by the Fe intercalation, is removed after its oxidation as observed also for the case of intercalated titanium.

To investigate the composition of the intercalated layer, Fe $2p_{3/2}$ high resolution XPS spectra were acquired, along with C 1*s*, at each stage of the preparation. We acquired spectra at 850 eV photon energy after the metallic Fe deposition and intercalation (figure 5.4a and b respectively) and we compared them with the spectrum acquired after an equivalent 0.5 ML Fe deposition performed on clean Ir (111) at room temperature (figure 5.4d). In all the three cases we identified the same spectral components. The one at lowest binding energy is associated to the iron atoms in the metallic state. We measured a slightly lower value for the binding energy of Fe 2*p* for metallic iron on graphene, 706.46 eV, respect to the one measured for iron in contact with Ir, 706.55 eV. This difference could be simply attributed to the different chemical environment, while the line shape remains unchanged. The second component in binding energy is related to multiplet effects typically observed in Fe 2*p* photoemission spectra [23, 24]. For simplicity, we described these effects as a single component in the photoemission spectra with an intensity between 60 and 70% of that of the metallic component, at a binding energy of 707.17 eV on graphene and 707.45 eV on Ir (111). The small peak observed at high binding energies in all the three different systems at 709.95 eV is compatible with the photoemission signal generated by iron atoms in the +2 oxidation state [24, 25]. The spectral weight of this oxide component is less that 10% for Fe/Ir (111) as well as for Fe on top and below graphene, suggesting that the deposited iron is almost metallic. This result was achieved thanks to the good cleanliness condition of the UHV chamber, where the pressure during the intercalation process never

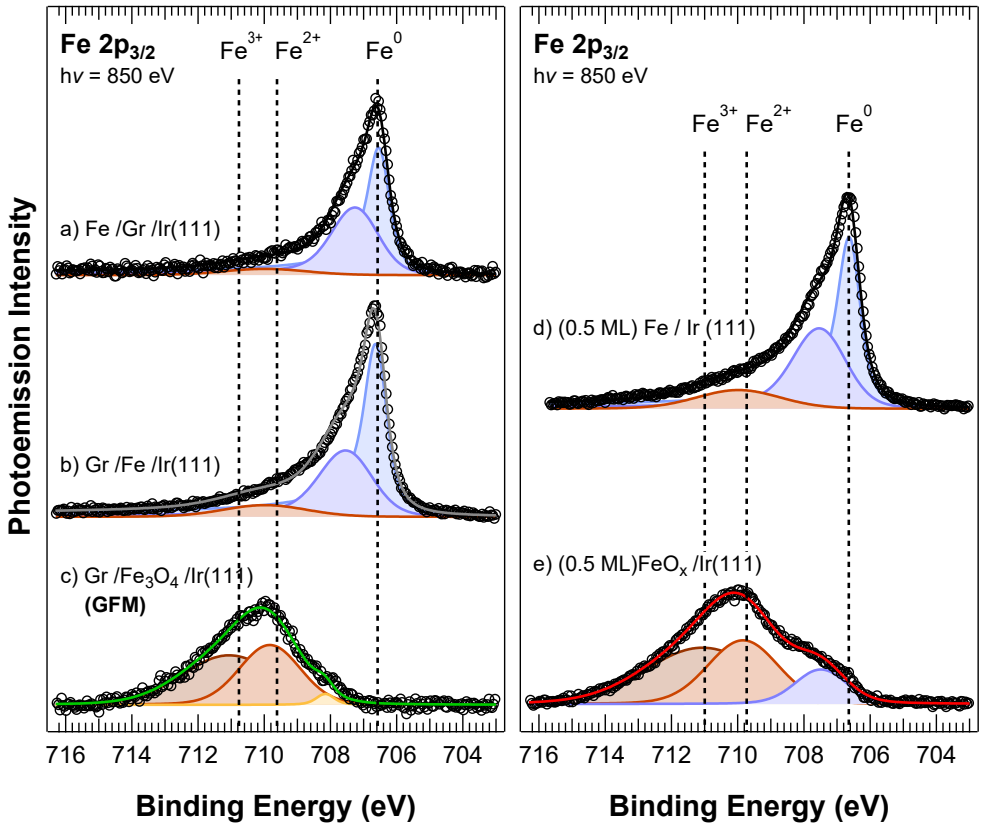

Figure 5.4: Fe $2p$ photoemission spectra acquired during the preparation of $Gr/Fe_3O_4/Ir\,(111)$ (GFM) and $FeO_x/Ir\,(111)$ (FM). a) 0.5 ML Fe deposition on graphene at room temperature; b) Fe intercalation; c) Fe oxidation below graphene; d) 0.5 ML Fe deposition on Ir (111) at room temperature; e) Fe/Ir (111) oxidation at room temperature.

exceeded 2×10^{-10} mbar.

Regarding the morphology of the Fe layer, we make some observation on the intensity of the Fe $2p$ photoemission signal measured for Fe/Ir (111) and Fe/Gr/Ir (111). Despite the amount of Fe is the same, the intensity measured in the first case is about 15% higher. This finding could be attributed to the formation of 3D Fe cluster on Gr, already reported in literature [17, 26], and a layer-by-layer growth on Ir (111), as reported, for example, for Fe/Ru (0001) [27]; in the case of 3D clusters the photoemission signal from the lower Fe layer is screened by the overlaying atoms. It is worth noting that after the intercalation we measured an increase of the Fe $2p$ photoemission signal. This increase, despite the screening effect of graphene, can be attributed to the disgregation of the 3D Fe clusters and the creation of a pseudomorphic Fe thin-layer on

Ir (111) as reported in literature [16, 17]. This hypothesis is supported by the concurrent decrease of the overall Ir $4f_{7/2}$ signal.

In order to investigate the composition of the iron oxide we acquired the Fe $2p$ spectrum after the oxidation process of the intercalated layer (GFM) and we compared it with the one we acquired for Fe-oxide on Ir (111) (FM) (figure 5.4c and e). The oxidation of Fe/Ir (111) was performed at room temperature, exposing the surface to 5×10^{-6} mbar of oxygen for 600 s. Time-resolved XPS was performed during the exposure to verify the complete oxidation of Fe. In this case, iron is completely oxidized at room temperature and with a partial pressure of O_2 that is lower than in the case of the GFM architecture. This is due to the absence of the Gr layer, which acts as a passivating agent for the Fe layer.

In both (0.5 ML)FeO_x/Ir (111) and GFM spectra a new component is observed at 711.05 eV. This is associated to the presence of Fe^{3+}. While for FeO_x/Ir (111) the 707.2 eV metallic component is still present, with a spectral wheight of 35%, for GFM we have the complete disappearance of this peak. A weak signal emerges instead at 708.13 eV in the GFM spectrum. This component can be assigned to iron in a sub-stoichiometric oxide of the form $Fe_{1-x}O$.

From the ratio between the 2+ and 3+ components, it is possible to calculate the average stoichiometry of the oxide. For the case of GFM we calculate that the ratio $I_{(+2)}/I_{(+3)}$ is 0.75 ± 0.03. This suggests that the oxide formed on Ir (111) below graphene is, in average, of the form Fe_3O_4. For (0.5 ML)FeO_x/Ir (111) an analogous calculation could be misleading, due to the presence of residual metallic Fe. Nevertheless, the average oxidation state calculated in this case is compatible with a FeO stoichiometry, which is the one observed for iron oxide grown on Pt (111) by procedures similar to the one we used and for coverage below 1 ML [28, 29].

Interestingly, the stoichiometry of the two oxide layers is different. The amount of oxygen with respect to iron is higher when the oxide layer is grown below graphene. This fact could be explained by the higher pressure and temperature values used for the oxidation of intercalated Fe. Furthermore, the Fe_3O_4 stoichiometry measured for GTM could appear in contrast with other experimental results reported for iron oxide intercalation, which declare a FeO stoichiometry [16, 30]. Nevertheless, 3+ and 2+ photoemission components are not singularly discussed in these experimental works and their overall Fe $2p$ spectra are anyway compatible with our data.

5.1.2 Iron thin-film and NPs/Gr growth

After their characterization, the two graphene-based interfaces (GM and GFM) were used as substrates for the iron oxide clusters growth. The growth procedure we performed consisted of the deposition of metallic iron at room temperature and its subsequent oxidation. To make a direct comparison with the analogous TiO_2 clusters, we deposited the same amount of metal, i.e. 2 ML. The coverage has been estimated from the Fe vapour exposure time, which was set to the quadruple of the evaporation time needed for the interfacial layer growth. This calibration of the evaporation time was carried out since it has been experimentally demonstrated that iron tends to form clusters when deposited on graphene at room temperature [17, 26]. Therefore it is not possible to accurately and reliably obtain the deposited iron quantity from XPS measurements. A reference system (FM) was prepared by depositing and oxidizing directly on Ir (111) the same amount of iron used for the cluster growth, equivalent to 2 ML.

Clusters and thin layer oxidation was performed by exposing the sample for 600 s to 5×10^{-6} mbar O_2 pressure at room temperature. We observed the evolution of the Fe $2p$ photoemission spectrum by time-resolved XPS during the oxygen exposure to verify that an equilibrium condition had been reached.

To acquire information about the morphology of the Fe-oxide grown on graphene we performed scanning tunneling microscopy measurements. In figure 5.5 a 500×500 nm surface scan is reported. Round shaped clusters are present, randomly distributed on graphene. This is in agreement with the experimental observation reported in literature and it is related to the fact that the Fe–Fe interaction dominates on the Fe–C one.

A statistical investigation of the clusters size dispersion was performed by the Gwyddion built-in function we used also for titanium dioxide clusters. The histogram in fig.5.5b shows the size distribution of the clusters observed in the displayed image. A size dispersion between 10 and 60 nm is measured. The average dimension of iron oxide particles (around 30 nm) results to be sensibly larger than that we measured for TiO_2 (9 nm). To understand this result we have to consider the factors that determine the average particles size and that have been discussed by Meakin and Amar [31, 32]. The average size of the clusters grown on a solid surface by evaporation depends on the deposition rate, on the diffusion of the adsorbed atoms and clusters and on the adatom–cluster and cluster–cluster sticking probability. Considering that the deposition rate for Ti and Fe was about 1 ML/h in both cases, the different size

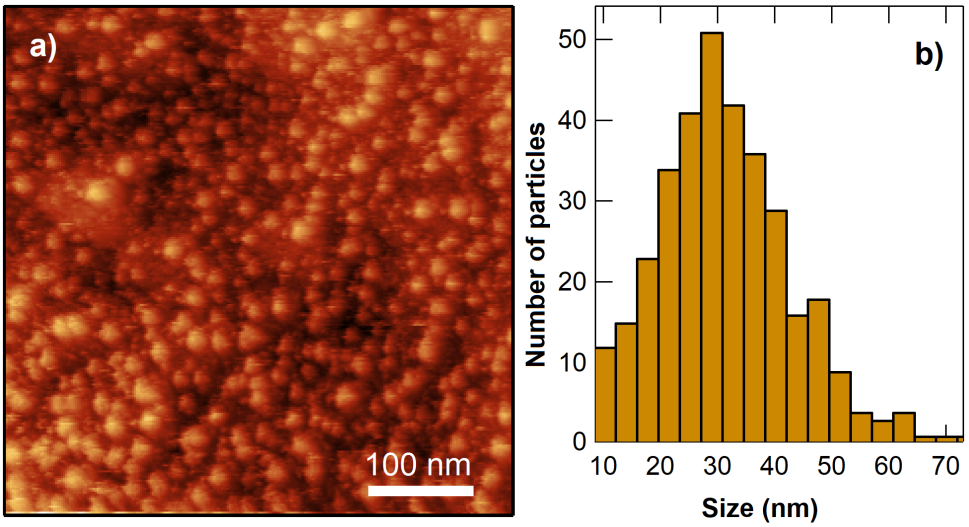

Figure 5.5: Morphological characterization of FGFM. a) STM image of a representative area of the sample ($500\times500\,\mathrm{nm}^2$, bias=1.25 V, current=0.09 nA) where iron oxides clusters, brighter, can be distinguished from graphene. b) Size distribution of the nanoparticles obtained from a.

distribution between the two particles population can be reasonably ascribed to the higher diffusion of Fe atoms and particles on graphene with respect to Ti, supposing that the oxidation process at room temperature does not affect the initial size distribution by promoting, for example, particles aggregation.

To retrieve information on the crystalline structure of the Fe-oxide we performed Near Edge X-ray Absorption Fine Structure measurements on the O K-edge and Fe $L_{2,3}$-edge; results are shown in figure 5.6. Measurements were performed on clusters supported by graphene with and without the interfacial oxide layer (FGFM and FGM respectively) and they were compared with the results obtained for the iron oxide layer directly grown on Ir (111) (FM). By comparing the absorption feature we observe on the O K-edge spectra with the ones associated to maghemite (γ-Fe_2O_3), magnetite ($Fe^{2+}Fe_2^{3+}O_4$) and hematite (α-Fe_2O_3) [33], we can infer that both clusters architectures seem to be mostly characterized by the presence of maghemite and/or magnetite. A more pronounced feature at 541 eV in the O K-edge of the thin layer suggests instead the possible presence of hematite.

From the Fe $L_{2,3}$-edge comparison, we observe a difference between the thin layer and the clusters in the intensity of the low binding energy shoulder of the L_3 component. The higher intensity of this feature has been attributed to a higher density of Fe^{2+} [34], that is compatible with the observation of the excess

of hematite in the thin layer with respect to the clusters. A remark is anyway necessary, regarding the fact that nanoclusters are intrinsically characterized by a non-negligible density of defects with respect to bulk, both compositional and structural, and a rigorous characterization of their crystallographic structure is not always straightforward. A similar consideration could be done for ultra-thin oxide layers, as the one we investigated, whose growth and oxidation mechanisms are strictly related to the specific substrate. Further details about the composition of the iron oxide in the three architectures can be obtained from the analysis of the photoemission spectra.

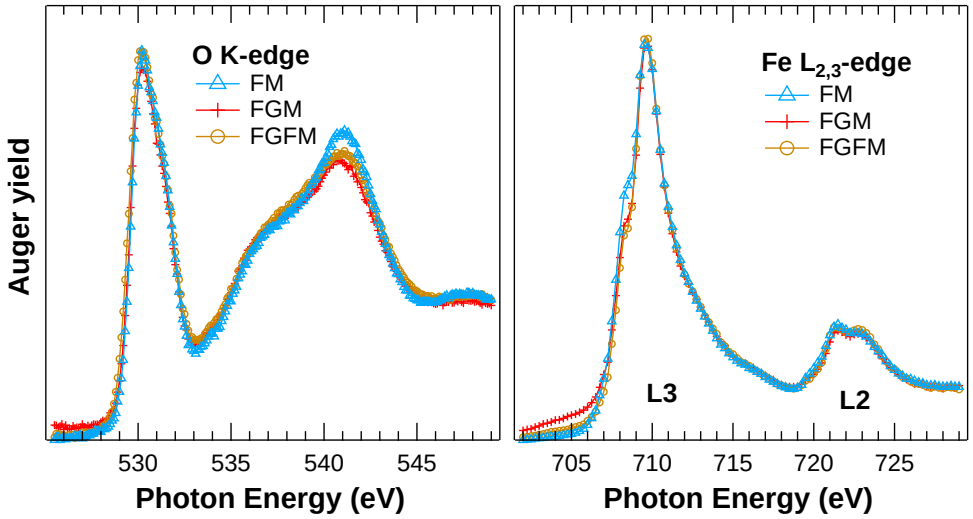

Figure 5.6: Near Edge X-ray Absorption Fine Structure spectra for FM, FGM and FGFM, acquired varying the photon energy through the a) O K and b) Fe $L_{2,3}$ absorption edges. The absorption measurements were performed in Auger yield mode.

High-resolution XPS measurements were performed for FM, FGM and FGFM after the metallic iron deposition and after its oxidation. Fe $2p$ spectra relative to the metal deposition are reported in figure 5.7a, b and c. The observed Fe $2p$ spectral components are the same shown previously in figure 5.4. The 706.46 eV component is the one related to metallic iron and it is always associated to the multiplet component at higher binding energy. A small amount of Fe^{2+} is observed for the case of iron directly deposited on Ir (111) while just traces of oxidized iron are found after the deposition on GM. Traces are also detected after the deposition on GFM, even if their quantification is more difficult, due to the presence of the already oxidized iron at the interface.

From the observation of the spectra acquired after the oxidation, we observe

that the metallic component is completely suppressed for FGM and FGFM, while a small residue can be detected in the FM. All spectra can be fitted with the same two main spectral components at BE = 710.00 eV and 711.05 eV, relative to Fe^{2+} and Fe^{3+} respectively. An additional component at 708.10 eV is present in the three spectra, particularly in FM where its spectral weight is about 5% of the total intensity. This spectroscopic feature could be either attributed to the presence of defects within the iron oxide or to Fe atoms interacting with the substrate, since it is detected for both Fe-oxide deposited on graphene and on Ir (111).

The spectroscopic intensity ratio Fe^{3+}/Fe^{2+} can be used to retrieve the average Fe oxidation state. This ratio results to be 1.7±0.1 for FM and 2.5±0.1 for FGM and FGFM. From these values we can calculate an average stoichiometry of $Fe_{0.76}O$ and $Fe_{0.74}O$. Therefore, Fe_3O_4 is a good approximation for the stoichiometry of the oxide forming all the three nanostructures.

We observed that the structural and compositional characteristics of the oxide nanoparticles grown on graphene with and without the oxide interface are virtually undistinguishable and this finding is similar to the one we made for titania nanoparticles. In that case the differences between TGM and TGTM consisted in the electronic structure of the systems and were reflected by the electronic structure of graphene. For this reason we investigated the C 1*s* photoemission spectrum after the Fe nanoparticles growth and after their oxidation on both GM and GFM substrates (figure 5.8).

We already discussed the effect of Fe deposited on Gr/Ir (111) which leaves almost unaffected the binding energy of the main C 1*s* component with respect to that of graphene (284.11 eV). After the oxidation we do not observe any modification of this value and we observe the disappearing of the small component at higher binding energy. Differently from what expected on the basis of the observation made on the titania nanostructures, from these spectral measurements there is no clear evidence of doping effects of graphene induced by the presence of Fe-oxide nanoparticles.

The situation is quite different when metallic Fe nanoparticles are deposited on GFM. In this case a split of the C 1*s* main component is observed along with a small shift to higher binding energies (283.65 and 283.95 eV, while the single component of GFM was at 283.50 eV). Two photoemission components are observed also after the oxidation at 283.56 and 283.85 eV. The deposition of metallic Fe tends to reduce the p-doping generated by the interfacial layer, while the particles oxidation tends to recover the p-doping. This behaviour was already observed for titania, while the presence of two well-defined spectro-

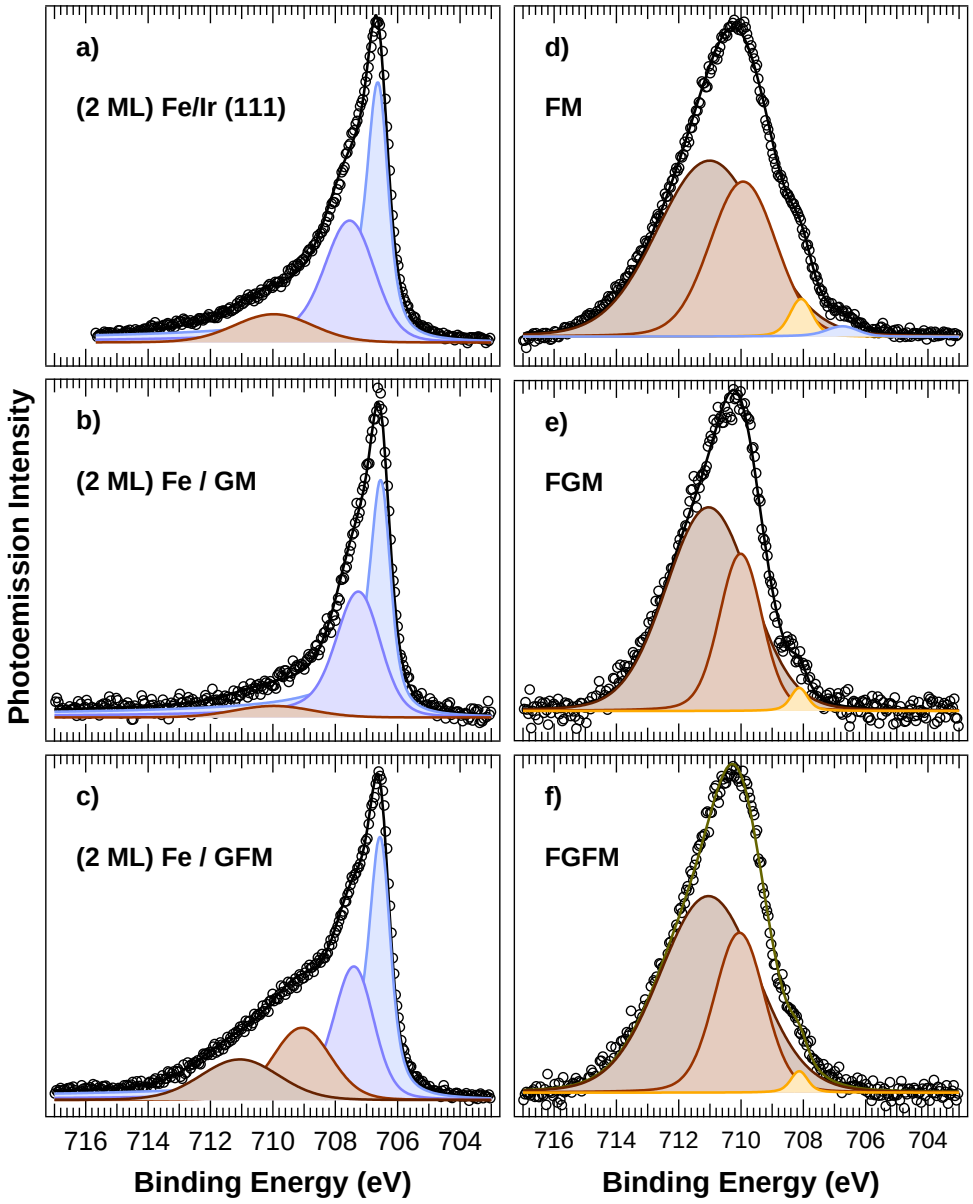

Figure 5.7: Fe $2p_{3/2}$ photoemission spectra acquired after 2 ML Fe deposition at room temperature on a) Ir (111), b) Gr/Ir (111) and c) Gr/FeO_x/Ir (111) are shown on the right. On the left are displayed the related Fe $2p_{3/2}$ spectra acquired after room temperature oxidation for d) Fe_3O_4/Ir (111), e)Fe_3O_4/Gr/Ir (111), f) Fe_3O_4/Gr/FeO_x/Ir (111).

scopic component is a remarkable difference. These are related to two distinct C species that arise after particles deposition on the p-doped graphene. An hypothesis that could explain these observation is that the interaction between iron and graphene is enhanced when graphene is doped and the presence of

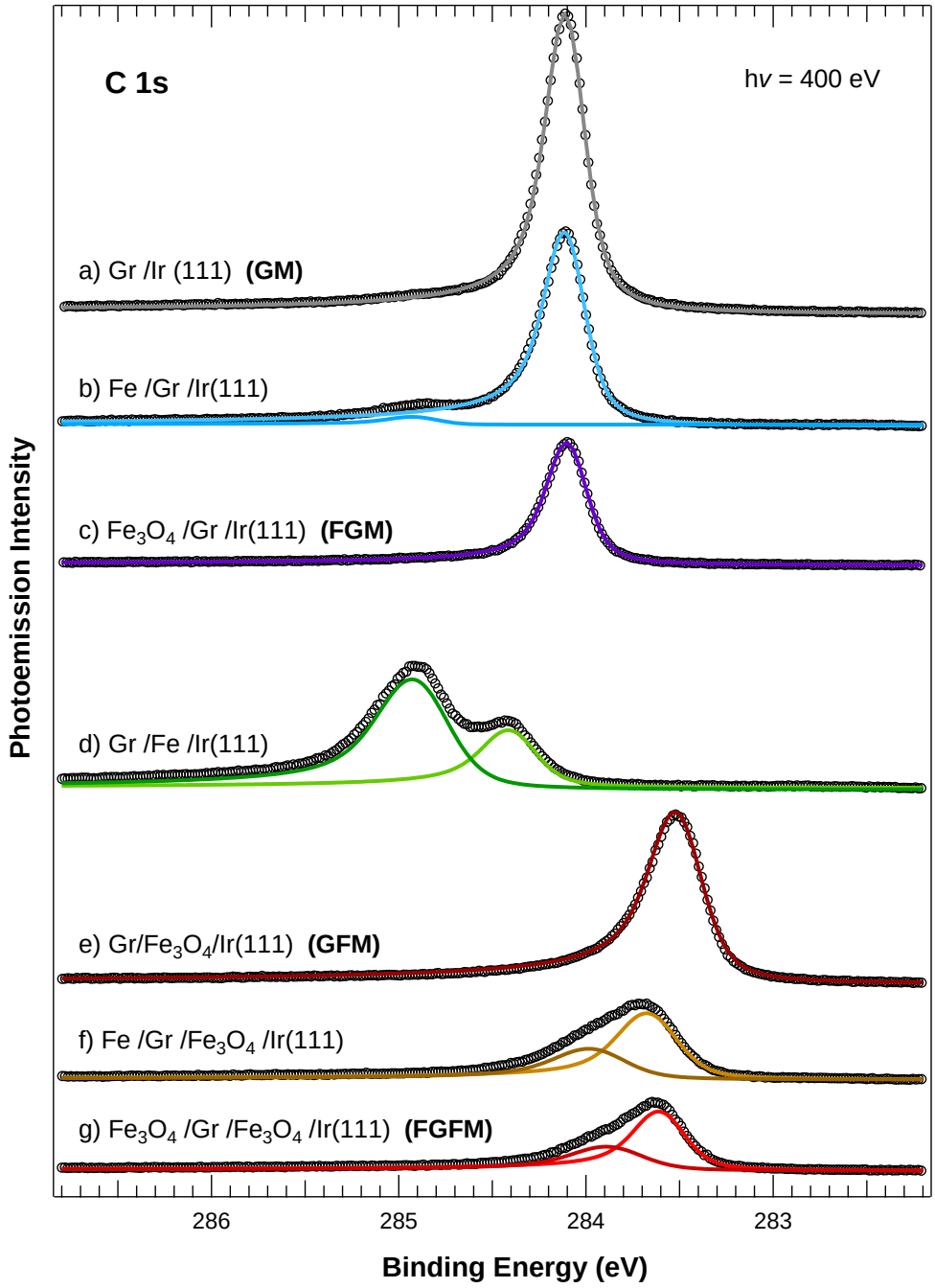

Figure 5.8: C 1*s* core level photoemission spectra acquired at 400 eV photon energy after each stage of the FGM and FGFM particles growth.

particles on graphene determines the existence of two C species, the one in contact with particles and the ones still facing vacuum.

To further investigate the electronic features of our architectures we ex-

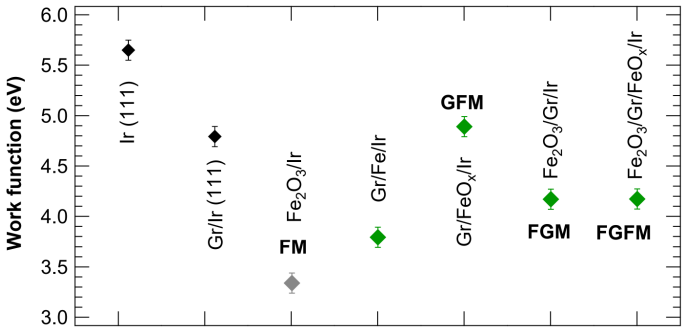

Figure 5.9: Work function values measured by photoelectron spectroscopy on the most significant iron-based nanostructured surfaces.

ploited HR-XPS to measure their work function; results are displayed in figure 5.9. The values for Ir (111) and FM are respectively the higher and the lower of the series (5.6 and 3.3 eV). An interesting observation can be done about the fact that the work function of GFM (4.9 eV) differs from the work function of Gr/Ir (111) (4.8 eV) by just 0.1 eV. This fact, considering that the error associated to these measurements is 0.1 eV, could be at the basis of the equivalence between the work function values measured for FGM and FGFM (4.0 eV).

In conclusion, we characterized two different graphene-based oxide interfaces from the compositional, structural and electronic point of view. We observed significant differences in the electronic structure of the two architectures that can be ascribed to the presence of the thin interfacial oxide layer below graphene. We demonstrated that, as it was for titanium dioxide, it is possible to sensibly modify the doping state of graphene also with iron oxide. In this case we obtained two composite systems with the same work function, in which iron oxide nanoparticles show the same structural and electronic properties, but in which graphene is present in two different doping states.

We believe that, if the graphene doping is actually the main difference between FGM and FGFM, the study of these Fe architectures represents a valuable opportunity to understand the capabilities of the nanofabrication in photocatalytic applications. The next step in the characterization of these architectures will be testing their photocatalytic activity. FM, FGM and FGFM samples are going to be prepared with the same procedures described in this chapter and they are going to be tested in the same condition used for the photocatalytic activity measurements on the titania architectures.

References

[1] Emsley, J.; Emsley, S. *Nature's Building Blocks: An A-Z Guide to the Elements*; Oxford Pakistan Paperbacks Series; Oxford University Press, 2001.

[2] Kolasinski, K. *Surface Science: Foundations of Catalysis and Nanoscience*; Surface Science: Foundations of Catalysis and Nanoscience; Wiley, 2002.

[3] Fendler, J. H. Photochemical solar energy conversion. An assessment of scientific accomplishments. *The Journal of Physical Chemistry* **89**, 2730 (1985).

[4] Kormann, C.; Bahnemann, D. W.; Hoffmann, M. R. Environmental photochemistry: Is iron oxide (hematite) an active photocatalyst? A comparative study: α-Fe_2O_3, ZnO, TiO_2. *Journal of Photochemistry and Photobiology A: Chemistry* **48**, 161 (1989).

[5] Dare-Edwards, M. P.; Goodenough, J. B.; Hamnett, A.; Trevellick, P. R. Electrochemistry and photoelectrochemistry of iron (III) oxide. *Journal of the Chemical Society, Faraday Transactions 1: Physical Chemistry in Condensed Phases* **79**, 2027 (1983).

[6] Gardner, R.; Sweett, F.; Tanner, D. The electrical properties of alpha ferric oxide—II.: Ferric oxide of high purity. *Journal of Physics and Chemistry of Solids* **24**, 1183 (1963).

[7] Kay, A.; Cesar, I.; Grätzel, M. New benchmark for water photooxidation by nanostructured α-Fe_2O_3 films. *Journal of the American Chemical Society* **128**, 15714 (2006).

[8] Wang, Y.; Wang, Q.; Zhan, X.; Wang, F.; Safdar, M.; He, J. Visible light driven type II heterostructures and their enhanced photocatalysis properties: a review. *Nanoscale* **5**, 8326 (2013).

[9] Tada, H.; Jin, Q.; Nishijima, H.; Yamamoto, H.; Fujishima, M.; Okuoka, S.-i.; Hattori, T.; Sumida, Y.; Kobayashi, H. Titanium (IV) dioxide surface-modified with iron oxide as a visible light photocatalyst. *Angewandte Chemie International Edition* **50**, 3501 (2011).

[10] Wu, Y.; Zhang, J.; Xiao, L.; Chen, F. Properties of carbon and iron modified TiO_2 photocatalyst synthesized at low temperature and pho-

todegradation of acid orange 7 under visible light. *Applied Surface Science* **256**, 4260 (2010).

[11] Wu, W.; Jiang, C.; Roy, V. A. Recent progress in magnetic iron oxide–semiconductor composite nanomaterials as promising photocatalysts. *Nanoscale* **7**, 38 (2015).

[12] Sivula, K.; Formal, F. L.; Gratzel, M. WO_3-Fe_2O_3 photoanodes for water splitting: A host scaffold, guest absorber approach. *Chemistry of Materials* **21**, 2862 (2009).

[13] Hou, Y.; Zuo, F.; Dagg, A.; Feng, P. A three-dimensional branched cobalt-doped α-Fe_2O_3 nanorod/$MgFe_2O_4$ heterojunction array as a flexible photoanode for efficient photoelectrochemical water oxidation. *Angewandte Chemie International Edition* **52**, 1248–1252 (2013).

[14] Tilley, S. D.; Cornuz, M.; Sivula, K.; Grätzel, M. Light-induced water splitting with hematite: improved nanostructure and iridium oxide catalysis. *Angewandte Chemie International Edition* **49**, 6405–6408 (2010).

[15] Hou, Y.; Zuo, F.; Dagg, A.; Feng, P. Visible light-driven α-Fe_2O_3 nanorod/graphene/BiV_{1-x} Mo_xO_4 core/shell heterojunction array for efficient photoelectrochemical water splitting. *Nano Letters* **12**, 6464 (2012).

[16] Ma, Y.; Travaglia, E.; Bana, H.; Bignardi, L.; Lacovig, P.; Lizzit, S.; Batzill, M. Periodic modulation of graphene by a 2D-FeO/Ir (111) moiré interlayer. *The Journal of Physical Chemistry C* **121**, 2762 (2017).

[17] de Campos Ferreira, R. C.; de Lima, L. H.; Barreto, L.; Silva, C. C.; Landers, R.; de Siervo, A. Unraveling the atomic structure of Fe intercalated under graphene on Ir (111): a multi-technique approach. *Chemistry of Materials* **30**, 7201 (2018).

[18] Vinogradov, N. A.; Zakharov, A.; Kocevski, V.; Rusz, J.; Simonov, K.; Eriksson, O.; Mikkelsen, A.; Lundgren, E.; Vinogradov, A.; Mårtensson, N.; *et al.*, Formation and structure of graphene waves on Fe (110). *Physical Review Letters* **109**, 026101 (2012).

[19] Miniussi, E.; Pozzo, M.; Baraldi, A.; Vesselli, E.; Zhan, R.; Comelli, G.; Menteş, T.; Niño, M.; Locatelli, A.; Lizzit, S.; Alfè, D. Thermal stability of corrugated epitaxial graphene grown on Re (0001). *Physical Review Letters* **106**, 216101 (2011).

[20] Preobrajenski, A.; Ng, M. L.; Vinogradov, A.; Mårtensson, N. Controlling graphene corrugation on lattice-mismatched substrates. *Physical Review B* **78**, 073401 (2008).

[21] Larciprete, R.; Ulstrup, S.; Lacovig, P.; Dalmiglio, M.; Bianchi, M.; Mazzola, F.; Hornekær, L.; Orlando, F.; Baraldi, A.; Hofmann, P.; Lizzit, S. Oxygen switching of the epitaxial graphene–metal interaction. *ACS Nano* **6**, 9551 (2012).

[22] Larciprete, R.; Lacovig, P.; Orlando, F.; Dalmiglio, M.; Omiciuolo, L.; Baraldi, A.; Lizzit, S. Chemical gating of epitaxial graphene through ultrathin oxide layers. *Nanoscale* **7**, 12650 (2015).

[23] Rossi, G.; Panaccione, G.; Sirotti, F.; Lizzit, S.; Baraldi, A.; Paolucci, G. Magnetic dichroism in the angular distribution of Fe $2p$ and $3p$ photoelectrons: Empirical support to Zeeman-like analysis. *Physical Review B* **55**, 11488 (1997).

[24] Soldemo, M.; Lundgren, E.; Weissenrieder, J. Oxidation of Fe (110) in oxygen gas at 400 °C. *Surface Science* **644**, 172 (2016).

[25] Lin, T.-C.; Seshadri, G.; Kelber, J. A. A consistent method for quantitative XPS peak analysis of thin oxide films on clean polycrystalline iron surfaces. *Applied Surface Science* **119**, 83 (1997).

[26] Cattelan, M.; Peng, G.; Cavaliere, E.; Artiglia, L.; Barinov, A.; Roling, L. T.; Favaro, M.; Píš, I.; Nappini, S.; Magnano, E. The nature of the Fe–graphene interface at the nanometer level. *Nanoscale* **7**, 2450 (2015).

[27] Santos, B.; Loginova, E.; Mascaraque, A.; Schmid, A. K.; McCarty, K. F.; de la Figuera, J. Structure and magnetism in ultrathin iron oxides characterized by low energy electron microscopy. *Journal of Physics: Condensed Matter* **21**, 314011 (2009).

[28] Weiss, W.; Ritter, M. Metal oxide heteroepitaxy: Stranski-Krastanov growth for iron oxides on Pt (111). *Physical Review B* **59**, 5201 (1999).

[29] Sala, A.; Marchetto, H.; Qin, Z.-H.; Shaikhutdinov, S.; Schmidt, T.; Freund, H.-J. Defects and inhomogeneities in Fe_3O_4 (111) thin film growth on Pt (111). *Physical Review B* **86**, 155430 (2012).

[30] Dahal, A.; Batzill, M. Growth from behind: Intercalation-growth of two-dimensional FeO moiré structure underneath of metal-supported graphene. *Scientific Reports* **5**, 11378 (2015).

[31] Meakin, P.; Vicsek, T.; Family, F. Dynamic cluster-size distribution in cluster-cluster aggregation: Effects of cluster diffusivity. *Physical Review B* **31**, 564 (1985).

[32] Amar, J. G.; Family, F. Critical cluster size: Island morphology and size distribution in submonolayer epitaxial growth. *Physical Review Letters* **74**, 2066 (1995).

[33] Giovannini, S.; Boscherini, F.; Carboni, R.; Signorini, L.; Pasquini, L.; Mahne, N.; Giglia, A.; Pedio, M.; Nannarone, S.; Benfatto, M. Multiple scattering analysis of O K-edge NEXAFS in iron oxides. *Physica Scripta* **2005**, 424 (2005).

[34] Thakur, P.; Choi, W.; Chae, K.; Kim, J.; Choudhary, R.; Tiwari, S.; Prakash, R.; Phase, D.; Kumar, R. X-ray absorption spectroscopic studies of pulsed-laserdeposited thin films of Fe_3O_4 on Si (111) substrate. *Journal of Korean Physical Society* **53**, 3694 (2008).

Chapter 6

Cobalt oxide-graphene interfaces

Among transition metals used in catalysis, cobalt is one of the most common. Along with iron, it is employed as a catalyst in the Fischer-Tropsch process for the synthesis of hydrocarbons [1, 2]. It is also historically known as an efficient catalyst in hydroformylation, a chemical process for the production of aldehydes from alkenes, which is at the basis of the industrial synthesis of a wide range of chemical products [3, 4].

Cobalt oxide was also largely studied. Its capability to act as a catalyst in the oxidation of CO is known since long time [5] and this specific catalytic process has been characterized in detail [6]. As demonstrated for Ti- and Fe-oxide, also for Co-oxide the chemical activity is enhanced when it is employed in form of nanoparticles. One of the most significant example is the enhanced catalytic activity of Co_3O_4 nanorods in the CO oxidation reaction with respect to the bulk material [7].

Concerning the water splitting reaction, cobalt-based materials are considered promising catalysts, despite their efficiency doesn't match the one of titanium dioxide and other complex metal oxide semiconductors. Nontheless, cobalt was studied as an the Earth abuntant metal for electrocatalytic water splitting with good results [8], in particular within organic compounds. Considerable research efforts were dedicated to the synthesis of Co-based molecular catalysts for both water oxidation and hydrogen reduction half reactions [9]. However, the chemical stability of these compounds represents a major issue in their practical application. Solid catalysts as well as cobalt compounds deposited on solid supports were therefore explored, to obtain more efficient and stable systems [10–12].

In the field of heterogeneous catalysis, cobalt oxide effectiveness in elec-

trochemical water splitting was proved [13, 14]. A comprehensive investigation of this process was carried out by Gerken *et al.* [15], who demonstrated that the cobalt oxide surface actively participate to the chemical process and that the oxidation state of Co atoms changes in time. This active behaviour is related to its chemical instability, especially in the hydrogen reduction process. Nevertheless, many studies were conducted about its activity in the oxygen evolution reaction.

The properties of cobalt oxide nanosized objects were explored with the aim of increasing its electrochemical catalytic efficiency. An interesting work by Chou *et al.* [16] reported that cobalt oxide NPs having similar size and shape show similar electrochemical activity independently of the stoichiometry of the constituen oxide. This is a remarkable example of size-dependent behaviour, which dominates over the chemical composition of NPs.

Along with the electrochemical characterization of cobalt-based materials, photocatalytic properties of analogous systems were investigated. The major issue in this context was initially the reduced light harvesting capability of these materials. For this reason cobalt compounds have been used as co-catalysts in combination with semiconductor photosensitizers [17, 18]. Few results are instead reported for stand-alone cobalt oxide. Among these, experiments on two-dimensional porous Co_3O_4 sheets demonstrated the capability of nanostructured cobalt oxide to act as an efficient photocatalysts [19]. An experimental work which is closer to our research topic is the one reported by Liao *et al.* who measured the photocatalytic activity of CoO nanoparticles for hydrogen production by water splitting [20]. They demonstrated the effectiveness of CoO NPs in both oxygen and hydrogen evolution reactions as they measured a 50 times higher photocatalytic activity for CoO NPs with respect to CoO micro-powder. The enhancement was attributed to the different alignment of the band gap of NPs and micro-powder relatively to the hydrogen reduction and water oxidation potentials (figure 6.1).

Several attempts to improve the photocatalytic activity of Co-oxide were made by associating metal oxide nanoparticles with graphene. Promising results were reported for Co_3O_4 nanocrystals on reduced graphene oxide, even if referred only to the oxygen evolution reaction [21]. Photocatalytic activity enhancement was reported for a similar catalyst made of cobalt ferrite nanoparticles on graphene [22]. In this particular case the efficiency enhancement was attributed to the increased mobility of the photo-excited charges in graphene.

At this point, a promising way for the production of a high performance cobalt oxide photocatalyst seems likely to arise from the combination of the

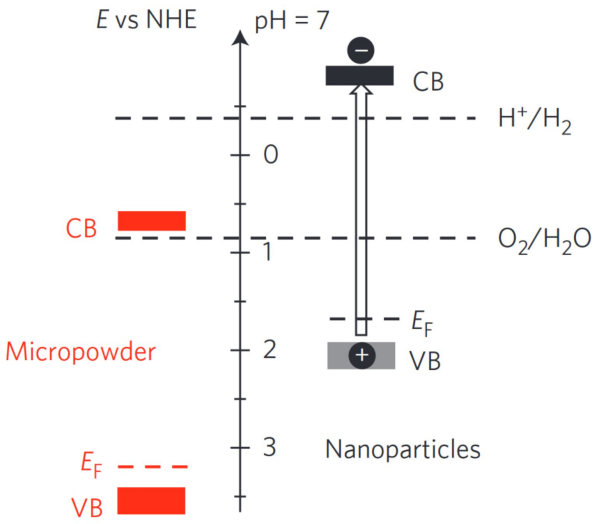

Figure 6.1: Energy diagram of the band gap for CoO micro-powder and nanoparticles reported by Liao *et al.* [20].

NPs size tuning, which can positively change the band gap alignment of cobalt oxide with respect to the water splitting reaction potentials, with the use of graphene, which provides a higher charge carriers mobility.

In this perspective we designed the cobalt oxide graphene-based interfaces described in this chapter. Moreover, our architectures combine the size control on the NPs, the association with graphene and the use of a solid support, which is expected to increase the thermal and chemical stability of the nanoparticles. In the following we will discuss their growth and characterization.

6.1 Sandwiched Co-oxide/graphene architectures

In our experiments we used cobalt oxide to grow nanostructured surfaces in analogy with the ones based on Ti- and Fe-oxide previously described. This part of the investigation is focused on cobalt oxide nanoparticles deposited on Gr/Ir (111) and on Gr/CoO_x/Ir (111). Within the present chapter, we will refer to these two architectures with CGM and CGCM respectively. The goal of this part of the experimental activity was to grow cobalt oxide sandwiched nanostructures and to compare them with the Ti- and Fe-based ones, considering in particular the electronic properties of graphene and its effect on the metal oxide clusters.

To this purpose, the characterization of the intercalated oxide layer is paramount and will be discussed in the first part of this chapter. In parallel,

a cobalt oxide thin layer directly grown on Ir (111) (CM) will be discussed, before moving the attention to the NPs growth and characterization.

The experimental activity regarding the preparation of these three interfaces and their XPS investigation was performed at the Materials Science beamline of the Elettra synchrotron radiation facility.

6.1.1 Interfacial cobalt oxide

The cobalt oxide intercalation was performed in two stages with a procedure similar to the one applied for titanium oxide: cobalt was firstly intercalated at the Gr/Ir interface and then oxidized. Metallic cobalt has been already used as an intercalating material for different purposes, such as the modification of graphene electronic structure [23–25], the investigation of the magnetic properties of 2D Co layers [26, 27] and the application in the field of energy storage [28].

Since Co intercalation has been widely studied, also by means of microscopic approaches [29], we applied an already used procedure that allowed us to intercalate cobalt below graphene, heating up the sample during the cobalt evaporation. This one-step process presents some advantages with respect to the procedure we followed for iron intercalation. In this case, the creation of clusters on top of graphene is hindered by the prompt diffusion and intercalation of the single atoms. Therefore, the probability of producing non-intercalated cobalt clusters is minimised. Moreover, the exposure of the sample to the contaminant gas pressure due to the evaporator and the heating filaments is reduced in time, providing overall cleaner condition for the interface preparation.

The calibration of the Co evaporation was performed by depositing cobalt in steps on clean Ir (111) and following the same procedure described for Fe. It is known from literature that Co grows in a pseudomorphic way on Pt (111) which has a 9.6% lattice mismatch [30], and that the growth is layer-by-layer [31]. By applying the methods described in section 2.1.2 we observed, during preliminary experiments, that the growth of Co is layer-by-layer also on Ir (111). Considering the similarities in the chemical and structural properties between Pt (111) and Ir (111), this result was expected. The evaporator calibration resulted to be particularly useful, since the experimental setup for the Materials Science beamline did not allow to perform fast XPS measurements during cobalt deposition and the coverage calibration cannot be obtained in real time.

The Co intercalation was achieved by heating Gr/Ir (111) at 670 K while

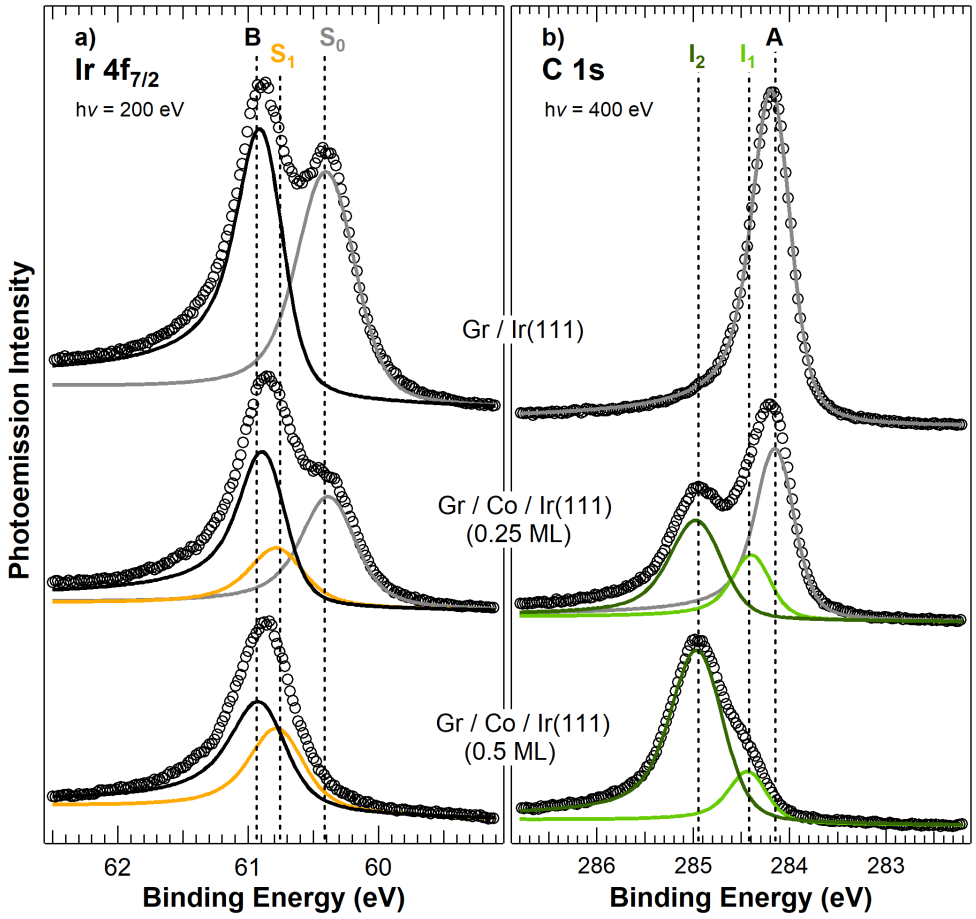

Figure 6.2: XPS spectra acquired before and after the two step Co intecalation. a) Ir $4f_{7/2}$ spectra; b) C $1s$ spectra.

evaporating Co. We observed that for lower temperature values the intercalation was not efficient, while it has been observed that, when Co is intercalated at temperatures above 700 K, an unwanted surface alloying phenomenon occours [32]. The intercalation was performed in steps, by depositing (0.25±0.05) ML at a time. After each step we acquired high resolution photoemission spectra, shown in figure 6.2, to monitor the intensity of the Ir $4f_{7/2}$ surface component and the changes in the C $1s$ spectrum. The initial Ir $4f_{7/2}$ spectrum, relative to Gr/Ir (111), is characterized by the typical surface (S_0) and bulk (B) components found at 60.34 and 60.89 eV respectively, while the C $1s$ spectrum is described by a single narrow component at 284.11 eV.

After the intercalation of 0.25 ML of Co, a decrease of the Ir $4f_{7/2}$ S_0 component is observed, along with the appearance of a third photoemission component at BE = 60.75 eV, which can be attributed to the presence of Co atoms bonded

with Ir. On the other hand, in the C 1*s* spectrum two new components I_1 and I_2 are found at higher binding energies with respect to A, at BE = 284.41 and 284.97 eV respectively.

After the second intercalation step, a total amount of cobalt equivalent to 0.5±0.1 ML is reached. The corresponding Ir $4f_{7/2}$ can be fitted by the B and the S_1 components only. The surface component S_0 is suppressed, suggesting that the chemical environment of all the atoms of the Ir (111) surface had changed. On the other hand, the A component of the C 1*s* spectrum is not detected and I_1 and I_2 entirely describe the shape of the spectrum. As already observed for the iron intercalation, two distinct chemical environment are present for carbon atoms, suggesting the enhancement of the moiré corrugation, as discussed in section 3.3. The higher binding energy values for I_1 and I_2 with respect to A hint a strong interaction between graphene and cobalt, with a charge transfer from cobalt to graphene and a strong re-hybridization.

I_1 and I_2 components were fitted with the same Lorentian width of the Gr/Ir (111) spectrum (0.14 eV) and a Gaussian width of 0.4 and 0.5 eV respectively, which do not differ significantly from the Ir-supported case (0.4 eV).

The concurrent suppression of the Ir $4f_{7/2}$ S_0 and C 1*s* A components can be interpreted as the evidence of a successful intercalation. The preservation of the C 1*s* total photoemission intensity (within less than 5%) is a further confirmation of the fact that the possible amount of residual non-intercalated Co on graphene is negligible. Therefore, we proceeded with the oxidation of the intercalated layer by exposing the sample to 1×10^{-1} mbar of oxygen at 520 K for 1 h.

The C 1*s* spectrum of Gr/CoO_x/Ir (111) is shown in figure 6.3 and compared with Gr/Ir (111) and Gr/(0.5 ML)Co/Ir (111). After the oxidation, the two high-BE components I_1 and I_2 vanish completely and the spectrum can be described by one single components J at BE = 283.66 eV. It is worth noting that the asymmetry parameter, which is related to the metallicity of the system, increases from 0.08 to 0.14 after the Co intercalation for both I_1 and I_2 and it remains higher than 0.08 also after the oxidation process (0.12), as it is expected for doped graphene. The density of states at the Fermi level is indeed higher, the higher is the degree of doping. Also in this case, as observed for the intercalated titanium and iron oxide layers, the moiré corrugation seems to be reduced.

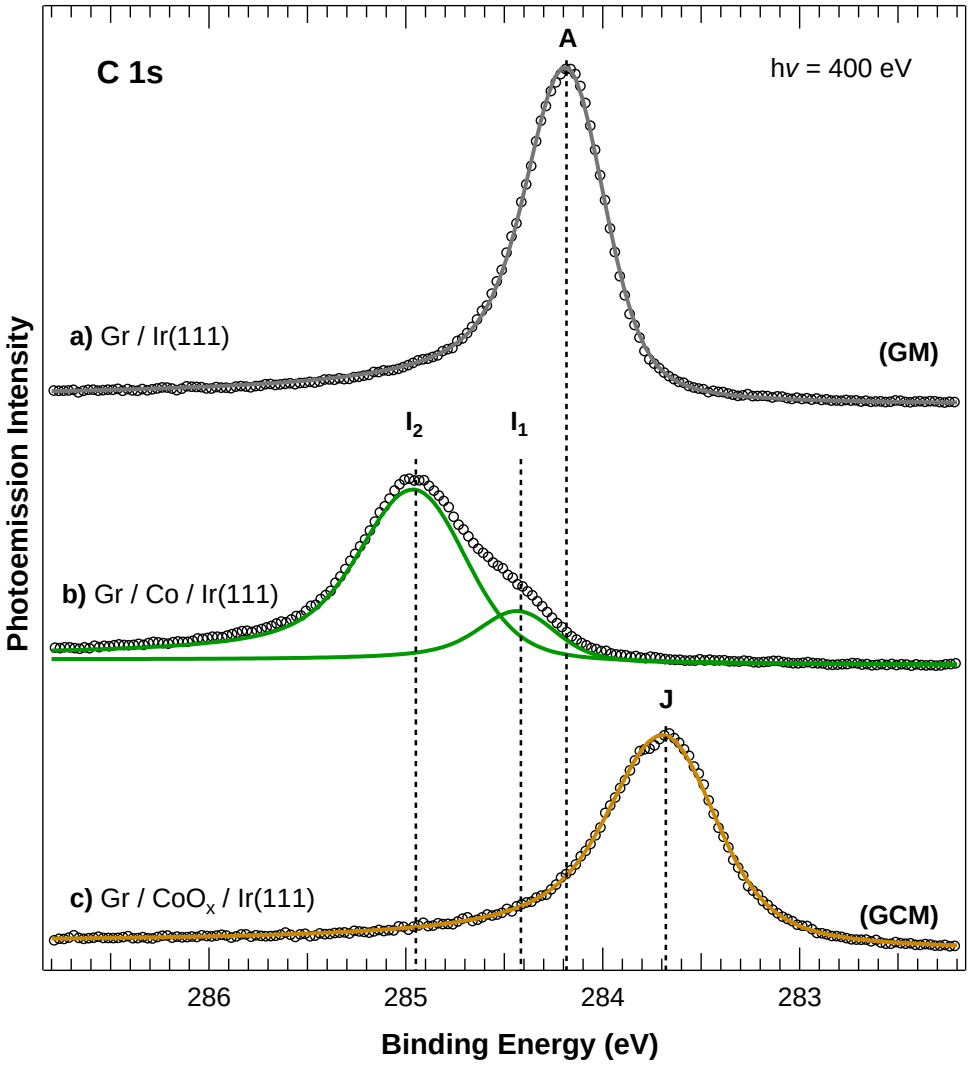

Figure 6.3: C 1*s* photoemission spectra acquired at 400 eV photon energy for a) Gr/Ir (111) (GM), b) Gr/Co/Ir (111) and c) Gr/CoO_x/Ir (111) (GCM).

To characterize the intercalated oxide layer we analysed the Co $2p_{3/2}$ photoemission spectra, starting from the intercalated metallic cobalt. In figure 6.4, a comparison is shown between the photoemission spectra relative to Co/Ir (111)(a) and Gr/Co/Ir (111) (b). The first interface was prepared by depositing 0.5 ML of Co at room temperature on clean Ir (111). Each photoemission spectrum was deconvolved on the basis of the already known binding energies associated with the cobalt oxidation states [33]. We observed the metallic component at 778.3 eV binding energy for both Co deposited on Ir (111) and Co intercalated below graphene, as well as two components at higher bind-

ing energies (779.4 and 780.9 eV), that are associated to cobalt with +3 and +2 oxidation state, respectively. A fourth spectral component at 785.8 eV was introduced in the fitting function to describe the various undistinguishable additional peaks generated by correlation and final state effects. The amount of oxide detected in both the deposited and the intercalated layers could be related to the presence of impurities in the experimental chamber during the Co evaporation, when the pressure was about 5×10^{-9} mbar.

In figure 6.4c and d the Co $2p_{3/2}$ spectra acquired after the oxidation are shown. While the Co $2p_{3/2}$ spectra acquired after the Co deposition are similar for Co/Ir (111) and Gr/Co/Ir (111), remarkable differences are detected in this case. It has to be noted, firstly, that the oxidation procedures applied for the two systems are different. The oxidation of Co/Ir (111) was performed at room temperature, exposing the sample to 5×10^{-6} mbar of oxygen for 600 s, while higher temperature and exposure values were used for the oxidation of the intercalated Co.

The Co $2p_{3/2}$ photoemission spectrum acquired on CoO_x/Ir (111) shows a Co^{2+} component whose intensity is about 3.5 times that of Co^{3+}. A significant amount of metallic Co is still present and comparable to the amount of Co^{3+}. On the other hand, the intercalated CoO_x layer is even less oxidized. The amount of metallic Co is again almost equal to that of Co^{3+}, while Co^{2+} is just double respect to it.

Further oxygen exposure in the same condition did not produce any appreciable change in the photoemission spectra of the two structures. This partial oxidation of Co could be related, in principle, either to a strong interaction between Co and Ir or to the formation of 3D Co clusters. Though, the latter hypothesis seems unlikely, considering that a Stranski-Krastanov growth should take place at least on Ir (111). The high affinity of Co with Ir was instead proved by experimental observation of Co-Ir alloying phenomena after annealing [32].

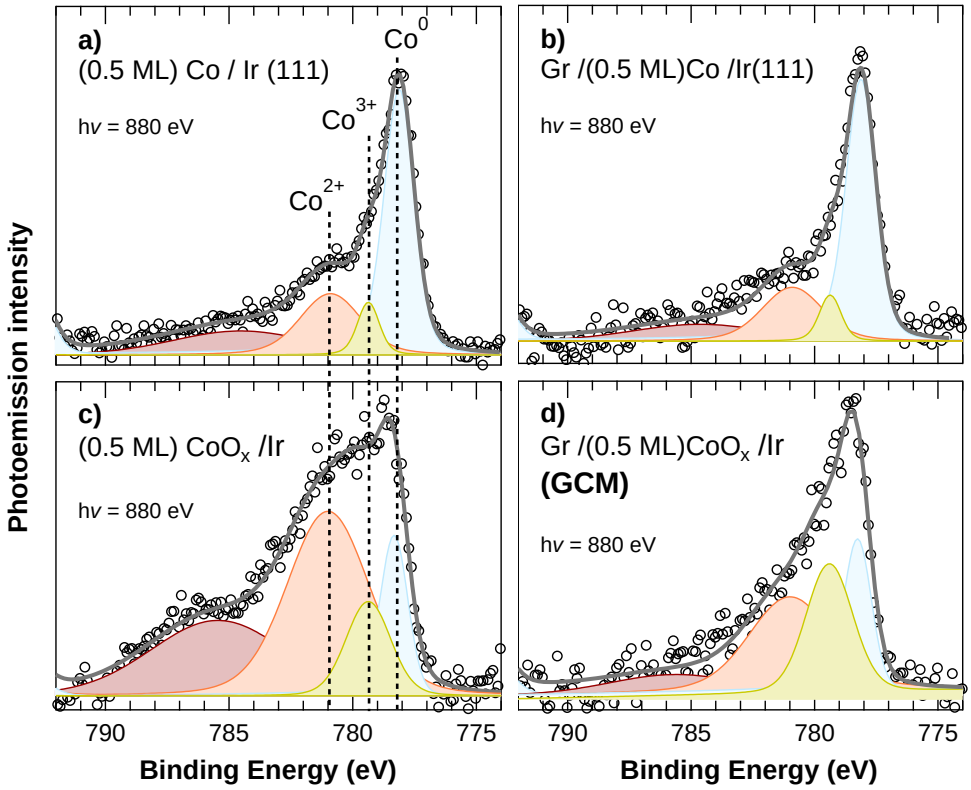

Figure 6.4: Co $2p$ photoemission spectrum, acquired at 880 eV photon energy for a) 0.5 ML of Co deposited at room temperature on Ir (111); b) 0.5 ML Co intercalated at the Gr/Ir (111) interface; c) 0.5 ML Co-oxide on Ir (111); d) 0.5 ML of Co-oxide intercalated.

6.2 Cobalt thin-film and NPs/Gr growth

CM, CGM and CGCM nanostructures were prepared depositing cobalt oxide on Ir (111), Gr/Ir (111) and Gr/CoO_x/Ir (111) respectively. The growth was performed by sublimating Co to deposit the equivalent of 2 ML of Co at room temperature. Afterwards, oxidation was performed exposing the interfaces to an oxygen pressure of 5×10^{-6} mbar for 600 s at room temperature.

A morphological investigation was performed on the CGCM architecture by scanning tunneling microscopy to characterize the cobalt oxide deposited on (doped) graphene. CoO_x appears to form flat, straight-edge-shaped islands. This observation suggests that the CoO_x–Gr interaction is strong enough to

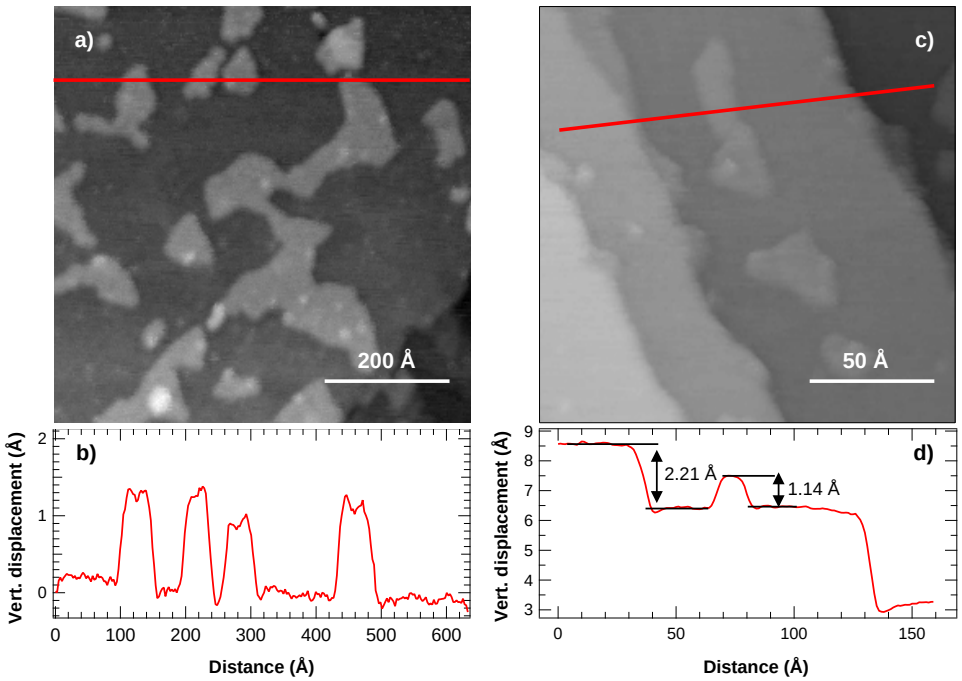

Figure 6.5: STM images acquired on CGCM. a) CoO_x nanoislands on a flat portion of the substrate; b) line profile acquired on the red line in image a. c) stepped area of the CGCM interface. Steps are due to the morphology of Ir (111) beneath. d) line profile on the red line in image c). The vertical tip displacement was calibrated on the height on the Ir (111) steps.

hinder the 3D growth of the oxide clusters. In figure 6.5 two representative STM images are reported along with image line profiles acquired on them. Images were acquired at constant current. We calibrated the vertical displacement of the tip on the basis of the Ir (111) interlayer distance (2.21 Å) measured on a stepped portion of the sample surface (figure 6.5c). With this calibration, we calculated an average value for the island height of 1.2 Å. Since the tunneling current is strongly dependent on the chemical composition of the investigated sample, this value should be considered just as an estimate. Nevertheless, the flatness of the CoO_x island could be associated to a certain degree of crystallographic order. To retrieve information from this point of view, we performed NEXAFS measurements on CGCM and on the other two interfaces.

Co $L_{2,3}$ absorption edge was investigated in Auger-yield mode scanning the photon energy from 770 to 810 eV. Despite the spectra do not show particularly defined features, a shoulder is detected at 778 eV, at lower photon energies with respect to the principal Co L_3 components at 779.5 and 781 eV. A further spectral feature is observed at 783.5 eV. The characteristics of these absorption

spectra, almost identical for CM, CGM and CGCM, result to be similar to the one reported in literature for CoO [34].

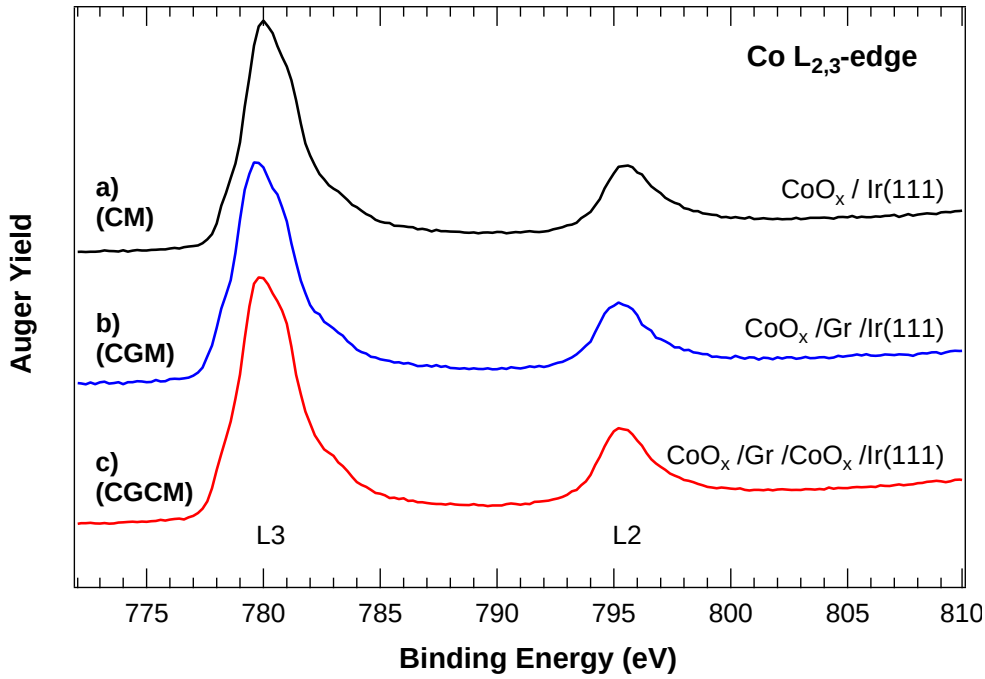

Figure 6.6: Near Edge X-ray Absorption Fine Structure spectra measured at the Co $L_{2,3}$-edge for a) CM, b) CGM and c) CGCM.

To characterize the chemical composition of the cobalt oxide we analysed the Co $2p_{3/2}$ photoemission spectra reported in figure 6.7. In a, b and c, the spectra relative to the metallic Co deposition are reported for Ir (111) and the two Gr-based interfaces. In all the three cases we detected the presence of oxidized Co atoms with +2 and +3 oxidation state, probably due to impurities in the experimental chamber. The binding energy values and the line shapes used for the fitting of this set of experimental data are identical to the one used for the description of the 0.5 ML Co deposition spectra reported in figure 6.4.

The amount of metallic Co calculated from the spectral weight of the photoemission components results to be between 39 and 42% of the total amount of deposited Co. The largest part of Co is therefore already oxidized after the deposition. Nevertheless, our goal was to completely oxidise it. CoO_x spectra are shown in figure 6.7 d, e and f. For cobalt oxide deposited on Ir (111) we are not able to distinguish the metallic component, which is very close in binding energy to the Co^{3+} component, and which was observed, instead, in

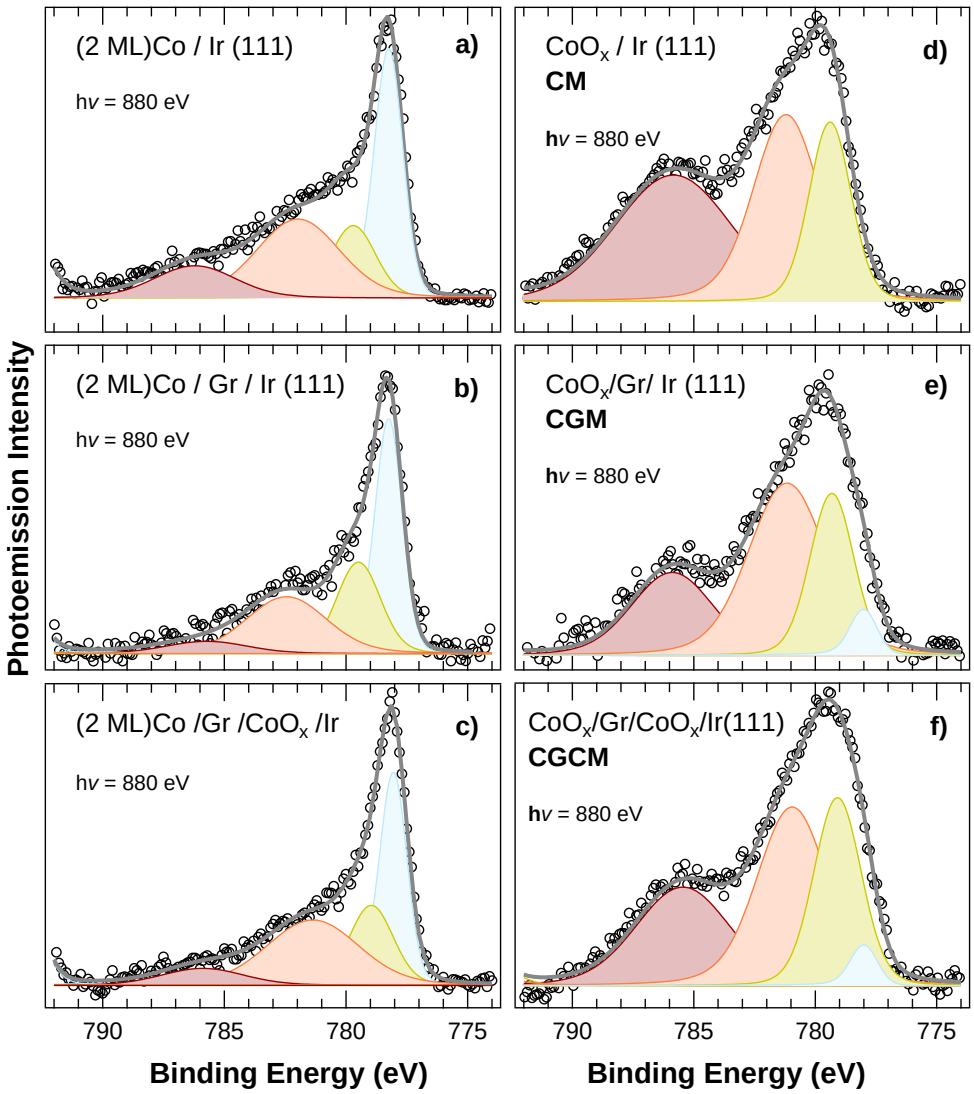

Figure 6.7: Co $2p_{3/2}$ photoemission spectra acquired during the two-steps cobal oxide growth on the three substrate under investigation.

the 0.5 ML oxide on Ir (111). This discrepancy could be ascribed to the fact that the oxygen dissociation probability, and therefore the efficiency of the oxidation procedure, could depend on both, the local Co configuration and the Co coverage. The measured photoemission intensity of the Co^{2+} component is about 1.7 times that of the Co^{3+}, therefore we can calculate an average stoichiometry of $CoO_{1.15}$, which is not significantly different from that of CoO, in agreement with the NEXAFS results.

The cobalt oxide island supported by graphene, with and without the interfacial layer, are almost indistinguishable from each other on the basis of

their chemical composition. The average stoichiometry of cobalt oxide islands is $CoO_{1.17}$ for bot CGM and CGCM. Their stoichiometry is very close to that of Co-oxide on Ir (111).

Cobalt oxide clusters deposited on graphene, with and without interface layer, are characterized by a residual amount of metallic Co, which gives rise to the 5 and 7% of the total photoemission intensity for CGM and CGCM respectively. For the case of CGCM, a small amount of the metallic Co could be due to the non-oxidized atoms at the interface. Nevertheless, the presence of metallic Co in the Gr-supported islands cannot be excluded. An explanation for the presence of metallic Co atoms could be related to their interaction with graphene either on the flat surface or at the defects.

In figure 6.8 the overall evolution of the C 1*s* spectrum during the CGM and CGCM nanostructures growth is reported. The spectrum measured on Gr/Ir (111) (a) does not differ from that measured after Co deposition (b), neither for the binding energy, nor for the line shape, while intensity is reduced due to the photoelectron inelastic scattering caused by Co. This behaviour is similar to the one observed in the previous chapter for iron and suggests that supported cobalt does not induce any appreciable doping.

Contrary to what observed for Fe-oxide, the oxidation of the supported Co islands (spectrum 6.8c) produces a large modification in the C 1*s* spectrum, in particular a shift of the photoemission component towards lower binding energy from 284.11 to 283.34 eV, concurrently with a slight increase of the Gaussian width from 0.35 to 0.42 eV. If we compare this result with the one obtained for the analogous architecture fabricated with titanium (TGM in figure 4.15), we detect a significant difference. For TGM the position of the C 1*s* was at slightly higher binding energies with respect to the one of Gr/Ir (111), so a n-doped graphene was observed, while it is the opposite for CGM graphene.

Concerning the graphene architecture with the interfacial Co-oxide, we measure an appreciable shift of the C 1*s* after the deposition of metallic Co on $Gr/CoO_x/Ir$ (111) (spectrum 6.8f) towards higher binding energy. The photoemission component moves from 283.66 to 283.86 eV. A similar behaviour was observed for both Ti- and Fe-based interfaces and it could be related to a partial compensation of the charge transfer. In this case we observe a Gaussian broadening of the photoemission component which can be associated to a higher degree of disorder and a higher number of chemically inequivalent C atoms. The broadening is further increased up to 0.7 eV after the Co oxidation. It has to be noticed that this trend has just a very reduced counterpart in the case of CGM, meaning that the combined effect of the interfacial and supported

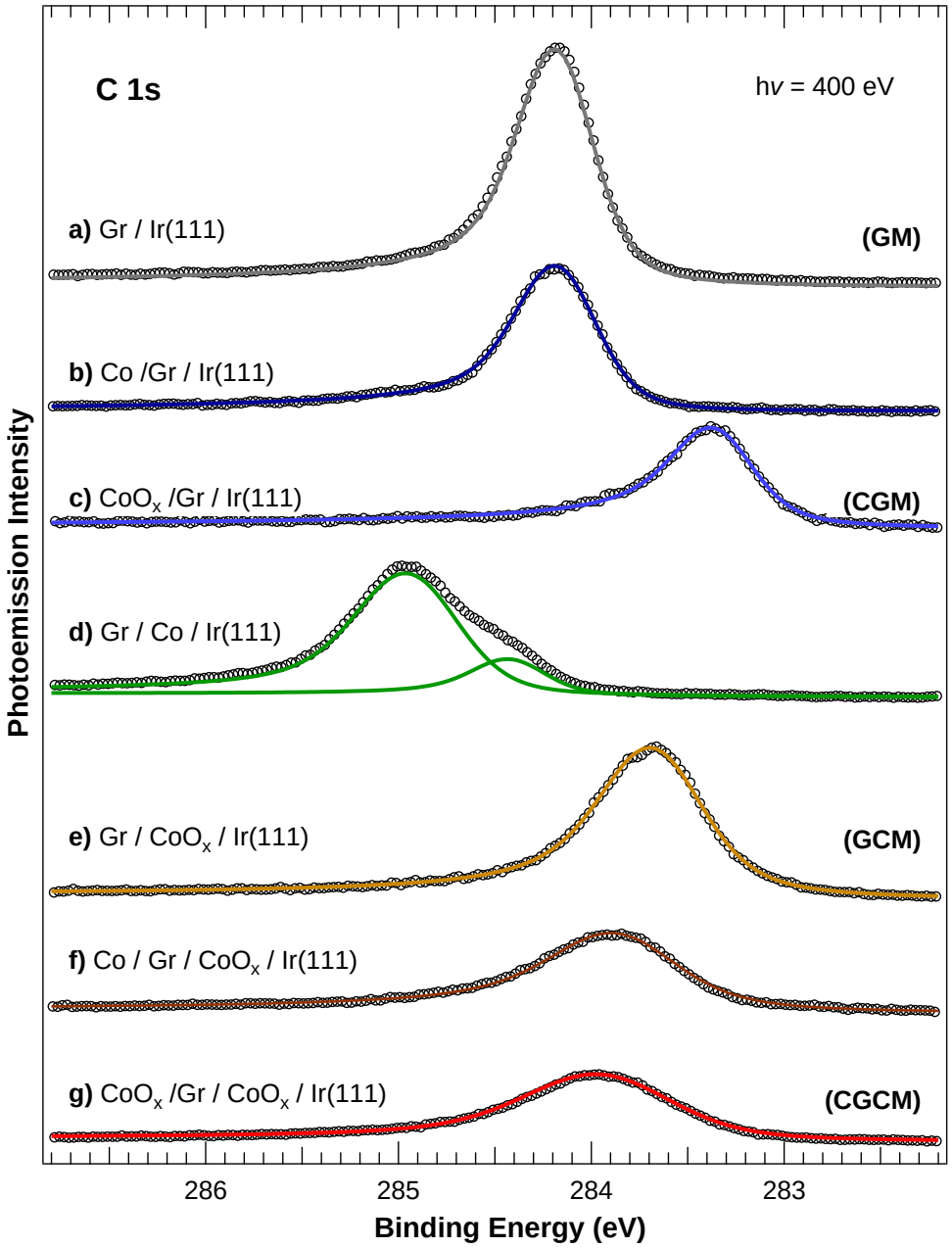

Figure 6.8: C 1*s* core level photoemission spectra acquired at 400 eV photon energy after each stage of the CGM and CGCM growth.

cobalt oxide is responsible for a large number of non-equivalent configurations for the C atoms in graphene. Moreover, the oxidation of Co islands supported by doped graphene (spectrum 6.8g) induces a further slight shift of the C 1*s* component to higher binding energy, from 283.86 to 283.93 eV. This small

reduction of the p-doping goes in the opposite direction with respect to the doping variation in the Ti-based system.

At this point it seems useful to summarize the observation on the doping state of graphene in the graphene-based interfaces for the three transition metal we considered. The deposition of metal oxide on Gr/Ir (111) induced different modification depending on the specific metal. While for Fe_3O_4 nanoparticles we did not appreciate any variation, we observed that TiO_2 NPs negatively dope graphene, while CoO_x islands induce a positive doping. The qualitative behaviour of graphene concerning the intercalation is instead the same for the three elements. Metal intercalation always induces an enhancement of the Gr–substrate interaction and the increase the moiré corrugation, while the metal oxide interface is responsible for the opposite effect, a charge transfer from graphene to the substrate and the suppression of the moiré corrugation.

The p-doping of graphene is preserved after the deposition of all the three metal oxides, suggesting that the substrate dominates the electronic modification of graphene with respect to the supported particles. Another common aspect is that the deposition of metal oxide on Gr/MO/Ir (111) tends to reduce the graphene doping generated by the interfacial oxide layer.

An analogous consideration about the differences and the similarities among the Gr-based interfaces made by the three metals species can be done observing the work function values. In figure 6.9 work function values of the Co-based interfaces are reported. It appears, in general, that higher binding energies of the C 1*s* are associated to higher values for the work function. For example, the WF of the interface containing the most p-doped graphene ($Gr/CoO_x/Ir$ (111)), is larger than the one of CGM, CGCM and Gr/Ir (111), as it was also for the Ti- and Fe-based architectures. The experimental error on the WF values does not allow to perform a detailed and comprehensive comparison, but the qualitative trend of the results suggests that a strict correlation between graphene doping state and work function exists.

In conclusion, we observed that cobalt oxide, as titanium and iron oxides, can be employed as intercalating material to substantially change the doping state of graphene and that a graphene electronic modification is observed after the deposition of cobalt oxide particles. Remarkable structural and compositional similarities were found between CoO_x NPs grown on graphene with and without the interfacial oxide. Moreover, the stoichiometry of the cobalt oxide deposited on graphene is not very dissimilar from that of CoO, which proved to be a good photocatalyst in form of nanoparticles [20]. In this respect, with the final aim of investigating the role of the graphene doping on the chemical

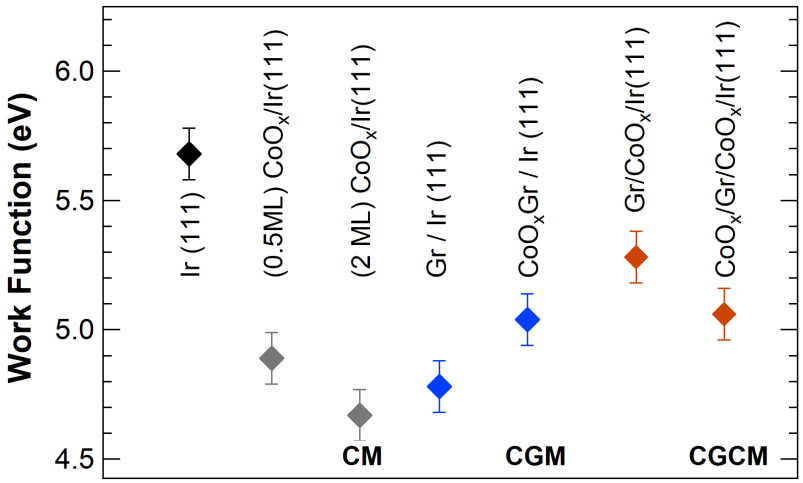

Figure 6.9: Work function values measured by XPS on the most significant cobalt-based nanostructures.

properties of the supported oxide, we executed preliminary photocatalytic measurements on our graphene-based architectures. We measured the amount of hydrogen produced by CGM and CGCM under simulated solar light in the same condition used for the titania architectures. Unfortunately, we did not detect any appreciable photocatalytic activity. The reason for this could be attributed to the fact that the amount of produced hydrogen was below the detection limit of the instrument. However, the negative results most probably could be attributed to the composition of the our cobalt oxide island. The chemical state of cobalt, in fact, has been shown not only to affect the reactivity of the catalyst, but also to determine the reaction mechanisms [34]. Despite Liao and co-workers demonstrated the activity of CoO nanoparticles, in literature the most active form of cobalt oxide seems to be Co_3O_4. Our intention was indeed to obtain this oxide. To increase the oxidation state of Co in the oxide islands we exposed them to higher O_2 pressure, but we did not observed significant changes. Alternatively, Co_3O_4 could be obtained by oxidizing Co islands at high temperature, as done for example by Faisal *et al.* [33] for a Co_3O_4 layer, grown on Ir (100), which was obtained at 523 K. Nevertheless, this method is not suitable for nano-sized aggregates, since the increase of the atomic mobility would likely induce coalescence phenomena among the islands that would sensibly increase the NPs dimensions and reduce their surface-to-bulk ratio.

References

[1] Kolasinski, K. *Surface Science: Foundations of Catalysis and Nanoscience*; Surface Science: Foundations of Catalysis and Nanoscience; Wiley, 2002.

[2] Khodakov, A. Y.; Chu, W.; Fongarland, P. Advances in the development of novel cobalt Fischer-Tropsch catalysts for synthesis of long-chain hydrocarbons and clean fuels. *Chemical Reviews* **107**, 1692 (2007).

[3] Slaugh, L. H.; Mullineaux, R. D. Novel hydroformylation catalysts. *Journal of Organometallic Chemistry* **13**, 469 (1968).

[4] Franke, R.; Selent, D.; Boörner, A. Applied hydroformylation. *Chemical Reviews* **112**, 5675 (2012).

[5] Pope, D.; Walker, D.; Moss, R. Preparation of cobalt oxide catalysts and their activity for CO oxidation at low concentration. *Journal of Catalysis* **47**, 33 (1977).

[6] Singh, S. A.; Madras, G. Detailed mechanism and kinetic study of CO oxidation on cobalt oxide surfaces. *Applied Catalysis A: General* **504**, 463 (2015).

[7] Xie, X.; Li, Y.; Liu, Z.-Q.; Haruta, M.; Shen, W. Low-temperature oxidation of CO catalysed by Co_3O_4 nanorods. *Nature* **458**, 746 (2009).

[8] Thoi, V. S.; Sun, Y.; Long, J. R.; Chang, C. J. Complexes of earth-abundant metals for catalytic electrochemical hydrogen generation under aqueous conditions. *Chemical Society Reviews* **42**, 2388 (2013).

[9] Karkas, M. D.; Verho, O.; Johnston, E. V.; Åkermark, B. Artificial photosynthesis: molecular systems for catalytic water oxidation. *Chemical Reviews* **114**, 11863 (2014).

[10] Cobo, S.; Heidkamp, J.; Jacques, P.-A.; Fize, J.; Fourmond, V.; Guetaz, L.; Jousselme, B.; Ivanova, V.; Dau, H.; Palacin, S.; Fontecave, M.; Artero, V. A Janus cobalt-based catalytic material for electro-splitting of water. *Nature Materials* **11**, 802 (2012).

[11] Sun, Y.; Liu, C.; Grauer, D. C.; Yano, J.; Long, J. R.; Yang, P.; Chang, C. J. Electrodeposited cobalt-sulfide catalyst for electrochemical and photoelectrochemical hydrogen generation from water. *Journal of the American Chemical Society* **135**, 17699 (2013).

[12] Lim, C. S.; Chua, C. K.; Sofer, Z.; Jankovský, O.; Pumera, M. Alternating misfit layered transition/alkaline earth metal chalcogenide $Ca_3Co_4O_9$ as a new class of chalcogenide materials for hydrogen evolution. *Chemistry of Materials* **26**, 4130 (2014).

[13] Wang, J.; Cui, W.; Liu, Q.; Xing, Z.; Asiri, A. M.; Sun, X. Recent progress in cobalt-based heterogeneous catalysts for electrochemical water splitting. *Advanced Materials* **28**, 215 (2016).

[14] Artero, V.; Chavarot-Kerlidou, M.; Fontecave, M. Splitting water with cobalt. *Angewandte Chemie International Edition* **50**, 7238 (2011).

[15] Gerken, J. B.; McAlpin, J. G.; Chen, J. Y.; Rigsby, M. L.; Casey, W. H.; Britt, R. D.; Stahl, S. S. Electrochemical water oxidation with cobalt-based electrocatalysts from pH 0–14: the thermodynamic basis for catalyst structure, stability, and activity. *Journal of the American Chemical Society* **133**, 14431 (2011).

[16] Chou, N. H.; Ross, P. N.; Bell, A. T.; Tilley, T. D. Comparison of cobalt-based nanoparticles as electrocatalysts for water oxidation. *ChemSusChem* **4**, 1566 (2011).

[17] Sun, Y.; Sun, J.; Long, J. R.; Yang, P.; Chang, C. J. Photocatalytic generation of hydrogen from water using a cobalt pentapyridine complex in combination with molecular and semiconductor nanowire photosensitizers. *Chemical Science* **4**, 118–124 (2013).

[18] Barroso, M.; Cowan, A. J.; Pendlebury, S. R.; Graätzel, M.; Klug, D. R.; Durrant, J. R. The role of cobalt phosphate in enhancing the photocatalytic activity of α-Fe_2O_3 toward water oxidation. *Journal of the American Chemical Society* **133**, 14868 (2011).

[19] Liu, J.; Wang, D.; Wang, M.; Kong, D.; Zhang, Y.; Chen, J.-F.; Dai, L. Uniform two-dimensional Co_3O_4 porous sheets: facile synthesis and enhanced photocatalytic performance. *Chemical Engineering & Technology* **39**, 891 (2016).

[20] Liao, L.; Zhang, Q.; Su, Z.; Zhao, Z.; Wang, Y.; Li, Y.; Lu, X.; Wei, D.; Feng, G.; Yu, Q.; Cai, X.; Zhao, J.; Ren, Z.; Fang, H. Efficient solar water-splitting using a nanocrystalline CoO photocatalyst. *Nature Nanotechnology* **9**, 69 (2014).

[21] Liang, Y.; Li, Y.; Wang, H.; Zhou, J.; Wang, J.; Regier, T.; Dai, H. Co_3O_4 nanocrystals on graphene as a synergistic catalyst for oxygen reduction reaction. *Nature Materials* **10**, 780 (2011).

[22] Fu, Y.; Chen, H.; Sun, X.; Wang, X. Combination of cobalt ferrite and graphene: high-performance and recyclable visible-light photocatalysis. *Applied Catalysis B: Environmental* **111**, 280 (2012).

[23] Enderlein, C.; Kim, Y.; Bostwick, A.; Rotenberg, E.; Horn, K. The formation of an energy gap in graphene on ruthenium by controlling the interface. *New Journal of Physics* **12**, 033014 (2010).

[24] Gyamfi, M.; Eelbo, T.; Waśniowska, M.; Wiesendanger, R. Impact of intercalated cobalt on the electronic properties of graphene on Pt (111). *Physical Review B* **85**, 205434 (2012).

[25] Presel, F.; Jabeen, N.; Pozzo, M.; Curcio, D.; Omiciuolo, L.; Lacovig, P.; Lizzit, S.; Alfe, D.; Baraldi, A. Unravelling the roles of surface chemical composition and geometry for the graphene–metal interaction through C1s core-level spectroscopy. *Carbon* **93**, 187 (2015).

[26] Decker, R.; Brede, J.; Atodiresei, N.; Caciuc, V.; Blügel, S.; Wiesendanger, R. Atomic-scale magnetism of cobalt-intercalated graphene. *Physical Review B* **87**, 041403 (2013).

[27] Rougemaille, N.; N'Diaye, A.; Coraux, J.; Vo-Van, C.; Fruchart, O.; Schmid, A. Perpendicular magnetic anisotropy of cobalt films intercalated under graphene. *Applied Physics Letters* **101**, 142403 (2012).

[28] Kumar, R.; Kim, H.-J.; Park, S.; Srivastava, A.; Oh, I.-K. Graphene-wrapped and cobalt oxide-intercalated hybrid for extremely durable supercapacitor with ultrahigh energy and power densities. *Carbon* **79**, 192 (2014).

[29] Vlaic, S.; Kimouche, A.; Coraux, J.; Santos, B.; Locatelli, A.; Rougemaille, N. Cobalt intercalation at the graphene/iridium (111) interface: Influence of rotational domains, wrinkles, and atomic steps. *Applied Physics Letters* **104**, 101602 (2014).

[30] Grütter, P.; Dürig, U. Growth of vapor-deposited cobalt films on Pt (111) studied by scanning tunneling microscopy. *Physical Review B* **49**, 2021 (1994).

[31] De Santis, M.; Buchsbaum, A.; Varga, P.; Schmid, M. Growth of ultrathin cobalt oxide films on Pt (111). *Physical Review B* **84**, 125430 (2011).

[32] Drnec, J.; Vlaic, S.; Carlomagno, I.; Gonzalez, C. J.; Isern, H.; Carlà, F.; Fiala, R.; Rougemaille, N.; Coraux, J.; Felici, R. Surface alloying upon Co intercalation between graphene and Ir (111). *Carbon* **94**, 554 (2015).

[33] Faisal, F.; Bertram, M.; Stumm, C.; Cherevko, S.; Geiger, S.; Kasian, O.; Lykhach, Y.; Lytken, O.; Mayrhofer, K. J.; Brummel, O.; Libuda, J. Atomically Defined Co_3O_4 (111) Thin Films Prepared in Ultrahigh Vacuum: Stability under Electrochemical Conditions. *The Journal of Physical Chemistry C* **122**, 7236 (2018).

[34] Zafeiratos, S.; Dintzer, T.; Teschner, D.; Blume, R.; Hävecker, M.; Knop-Gericke, A.; Schlögl, R. Methanol oxidation over model cobalt catalysts: Influence of the cobalt oxidation state on the reactivity. *Journal of Catalysis* **269**, 309 (2010).

Chapter 7

Size-selected nanocluster source

Nanoparticles have been extensively studied for their employment in a variety of applications and their size has always been a fundamental parameter within these investigations. In the previous chapter we reported some evidence from literature about the size-dependent photocatalytic activity of nanoparticles, but that is just one of the size-induced effects that are observable in such systems. Electronic, magnetic, chemical and optical properties of nanoscopic aggregates are strongly size-related, and the smaller are the particles, the stronger is the size effect. Despite the existance of these effects has been known for long time, still fascinating observation are done nowadays due to the vastness of this field of research [1]. Sometimes the term nanoclusters (NCs) is used instead of nanoparticles to refer to atomic aggregates formed by a small number atoms and showing quantum effects [2–4].

The interest on this kind of physical systems rose few decades ago, when the possibility to fabricate aggregates of few atoms provided a way to create new structures, sometimes called superatoms, that for their quantum nature could be actually considered as new synthetic atoms or, more properly, molecules which showed completely new properties. To prove the validity of this theoretical approach, diverse nano-fabrication techniques were introduced for the production of free and solid-incorporated quantum systems such as metal clusters [5] or semiconductor heterostructures [6]. However, a great advance in the study of nanoscale systems was made with the introduction of the first size-selected cluster sources.

The first milestone achieved by means of a cluster source was the resounding discovery of Buckminsterfullerene [7]. The possibility to produce large amounts of identical C_{60} aggregates brought to the further discovery of the extraordinary

properties of fullerene molecular solids. This stands as a bright example of the employment of superatoms intended as fundamental constituents of new materials. Since then a large community of researchers continued to develop size-selected cluster sources, testing different technical strategies to achieve the best performances.

A state-of-the-art size selected nanocluster source is installed in the Surface Science Laboratory at Elettra. The machine was developed in collaboration with the research group of Prof. Ulrich Heiz from the Technical University of Munich, on the basis of one of their operating size-selected nanocluster sources [8]. In this chapter I will describe the structure and the working principles of our cluster source, along with the results of the first functional tests we performed immediately after its completion.

7.1 Working principles and description of the SSL cluster source

The practical approach implemented in our source, as in the large majority of size-selected clusters sources, is the bottom-up production of free atomic aggregates. In this kind of sources, the NCs production process consists of the disgregation of the raw material down to single atoms and their condensation into atomic aggregates, which are delivered in a vacuum chamber and can be finally mass-selected by a dedicated instrument.

The specific disgregation and condensation methods define a series of cluster source families that were developed during the years. The cluster source in operation at the Surface Science Laboratory is a laser-ablation/supersonic-aggregation source. It is designed to deposit NCs in ultra-high vacuum condition, with the possibility to select clusters with a precise number of atoms. A schematic representation of this machine is reported in figure 7.1.

The structure of the SSL source consists of four vacuum chambers, each one equipped with a dedicated pumping stage, connected to each other through small apertures so to create a differential pumping system. Good vacuum conditions are indeed required during the aggregation process to produce high purity clusters. Moreover, the presence of contaminants in the final NCs deposition environment has to be minimized, due to the high chemical reactivity of these small atomic aggregates.

To understand the need of a differentially pumped system is necessary to go through the details of the production process, which are described in the

following.

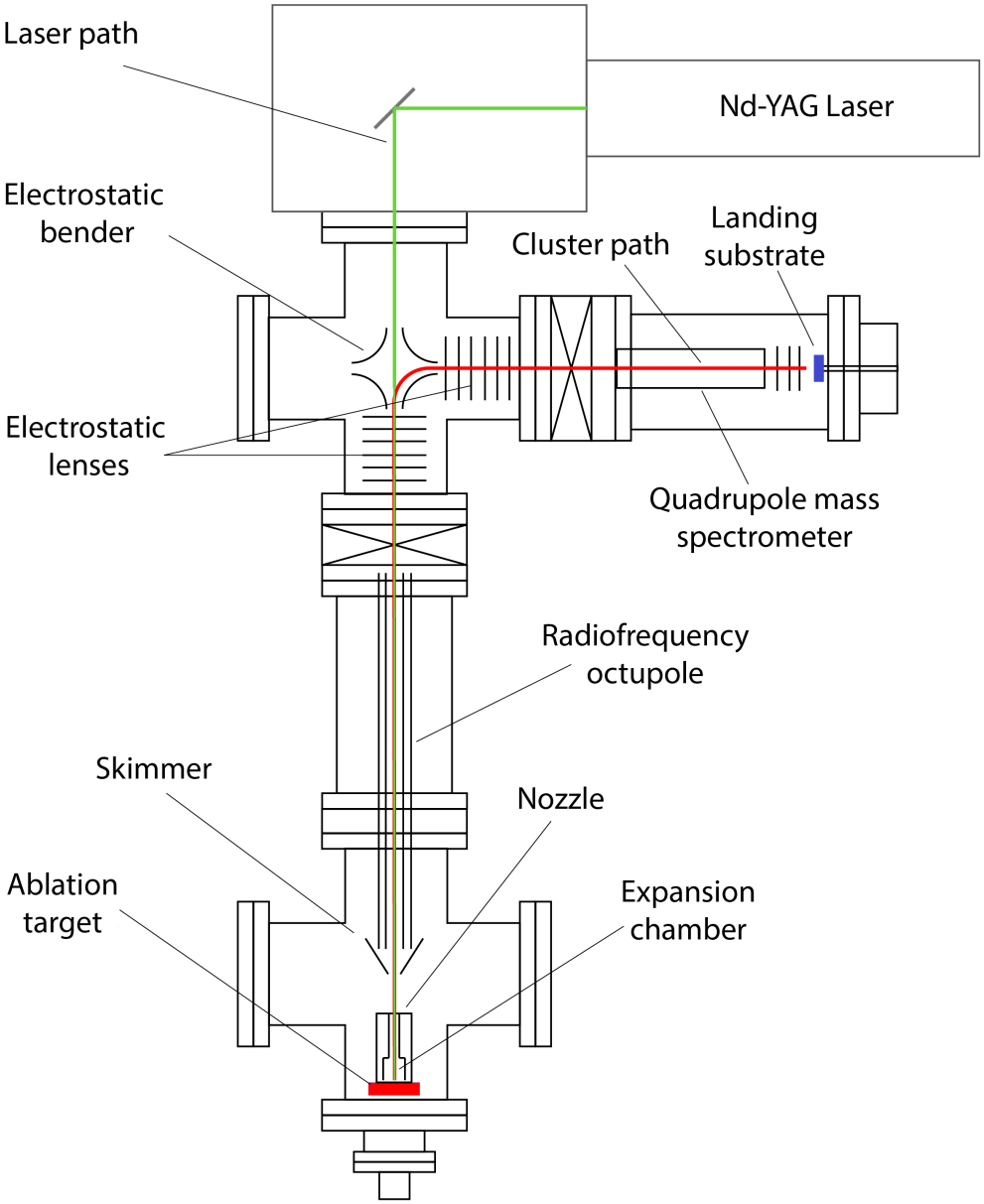

Figure 7.1: Schematic representation of the size selected nanoclusters source installed at the Surface Science Laboratory of Elettra.

Monomers production. By definition, aggregation sources requires the atomization of the raw material, for which various methods were proposed. In figure 7.2 some historical solutions are represented [9]; some of them slowly

fallen into disuse, as the evaporation by thermal heating in a so called "hot oven" configuration. The main disadvantage of the thermal vaporization is the presence of contaminants from the heated vacuum chamber walls, partially attenuated by heat-shields.

The evaporation of the material by arc discharge is instead actually employed as an efficient method for the production of metal clusters, despite some limitations related, for example, to the electrical conductivity of the raw material.

Another widespread atomization method is the ion sputtering, for example, by cesium ions, as implemented in one of the first compact sputter sources [10]. Plasma sputtering was subsequently developed and can be considered an improvement of the ion sputtering, whose most important advantage is that a significant proportion of sputtered material, including clusters from the condensation process, is readily ionized by the plasma [11].

Among the several atomization techniques under development, laser ablation was early introduced in the history of the cluster sources to directly sublimate solid targets. Nowadays, laser ablation sources are still widely used due to a series of advantages [12].

Ablation by short laser pulses proved to be an efficient method to obtain monomers without heating a consistent amount of material and therefore providing a low concentration of contaminants during the cluster aggregation. The first laser ablation source was introduced in 1981 [13] and, by means of a similar machine, C_{60}-buckminsterfullerene was discovered just five years later [7].

The efficiency of the ablation process is related to a series of parameters describing the laser pulse. The duration of the laser pulse is an important aspect since it determines the efficiency of the ablation process. Usually the laser pulse duration employed in this kind of sources is of the order of nanoseconds. It is indeed demonstrated that, for metal targets, the ablation efficiency (defined as the mass of removed material per unit of pulse energy) is maximised for these time duration values [14]. The ablation process in the nanosecond regime can be classically described as subsequent phase transitions, namely solid to liquid and liquid to vapour, followed by ionization [15].

In the SSL cluster source, the ablation of the raw material target is performed by a pulsed Nd-YAG laser, operating in the second harmonic wavelength at 532 nm. The duration of a single pulse is fixed and equal to 7 ns. The power of each single pulse has a Gaussian spatial distribution in the transverse direction and the energy delivered by a single pulse can be varied between 5 and 140 mJ.

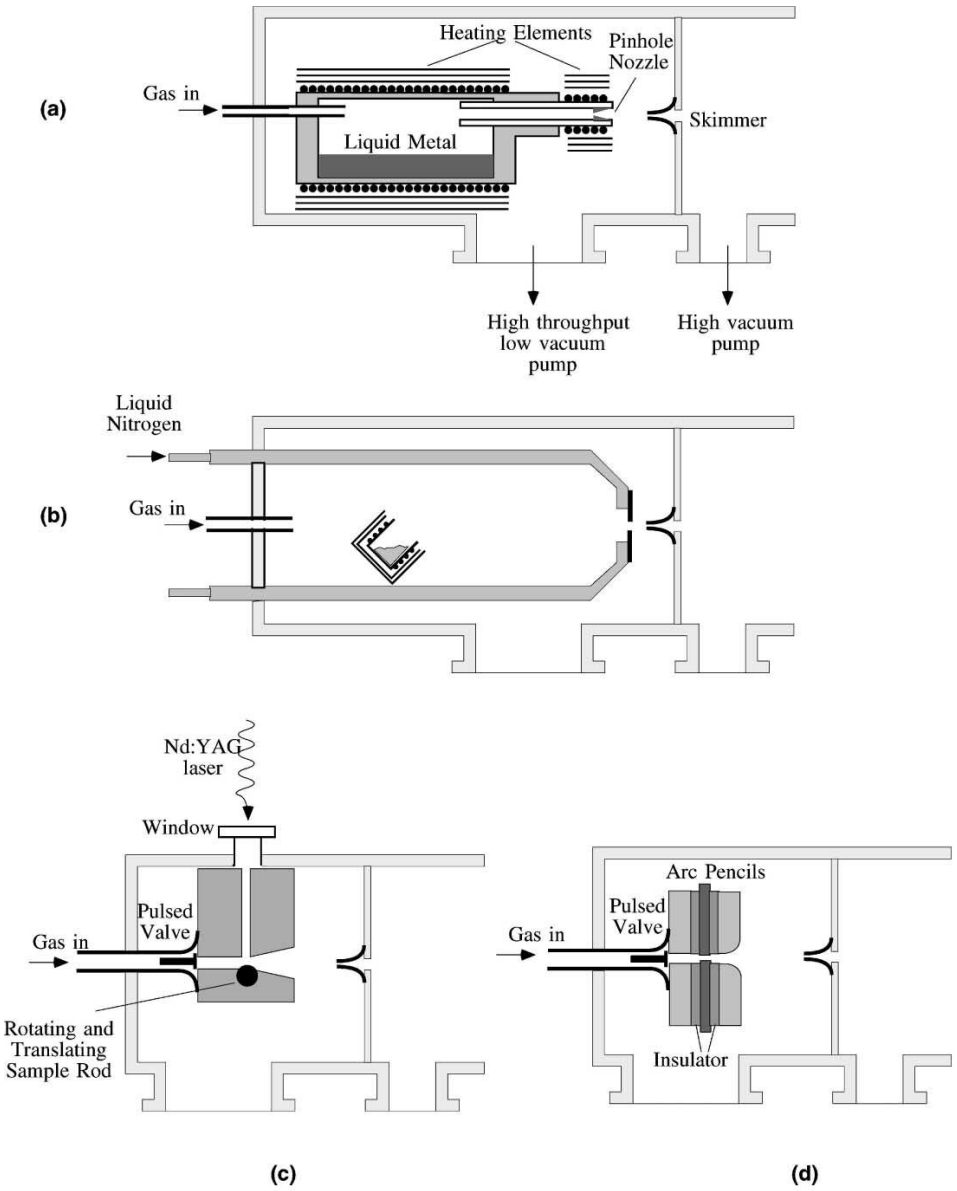

Figure 7.2: Basic layout of aggregation sources. A flux of inert gas is employed to control the aggregation process in all the depicted setups. a) example of a source with a hot oven configuration; b) hot oven clustersource, equipped with a liquid nitrogen heat-shield; c) laser ablation source; d) pulsed arc discharge cluster source. Image reproduced from [9].

The laser beam is focused on the raw material target by a convex lens with 1200 mm focal length and driven into the chamber through a fused silica UHV viewport. The section of the laser beam is about 7 mm in diameter at the viewport and less than 1 mm on the target.

The target used in the tests described in this chapter consists of a 40 mm diameter disc of silver with 99.99% purity degree. The target is kept in motion during the ablation to avoid the perforation of the the metal plate, that for a 2 mm thickness plate would occur in a few minutes. The disc is connected to an off-axis electric motor; an external/internal gear coupling is employed to obtain a hypocycloidal motion of the laser spot on the target (see figure 7.3). With this setup, the laser ablation is distributed in a wide area of the target and the velocity of the laser spot on the target remains continuously different from zero, avoiding the heating of the material around the ablation point.

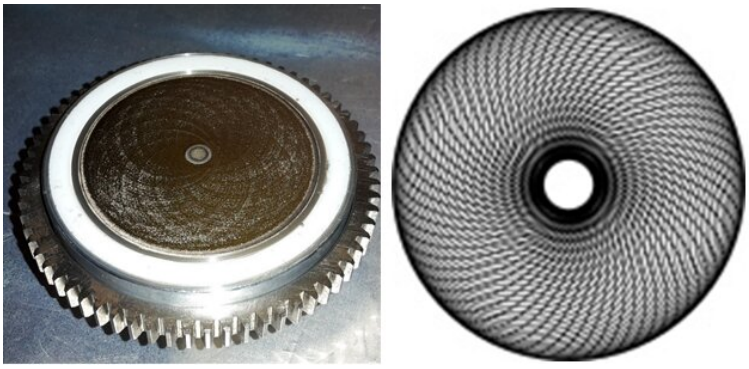

Figure 7.3: A picture of the silver target and the drawing of the hypocycloidal path obtained coupling the 71 teeth target gear with an 103 internal toothed gear. The high value for the two prime numbers of teeth ensures a reduced superposition of the laser path and a wide available ablation area on the metal disc.

Cluster aggregation. After the laser pulse, an amount of raw material is produced in form of ionized vapours near the ablation region. At this point, the aggregation of NCs is generally induced by the cooling effect of an inert carrier gas which is fluxed into the chamber on the ablation target.

The carrier gas transports the ablated material into a so called thermalization chamber (see figure 7.4), where a heat exchange takes place between the plasma and the chamber walls, mediated by the carrier gas. The thermalization process narrows the velocity distribution of the gas and plasma particles, before a supersonic adiabatic expansion of the gas mixture takes place within the exit channel towards the vacuum chamber. During this expansion the temperature of the gas decreases at a rate ranging between 10^8 and 10^{11} K/s [16]. During this expansion, the condensation of NCs takes place, producing a population with a relatively narrow mass distribution.

The mass distribution is related to the characteristics of the supersonic

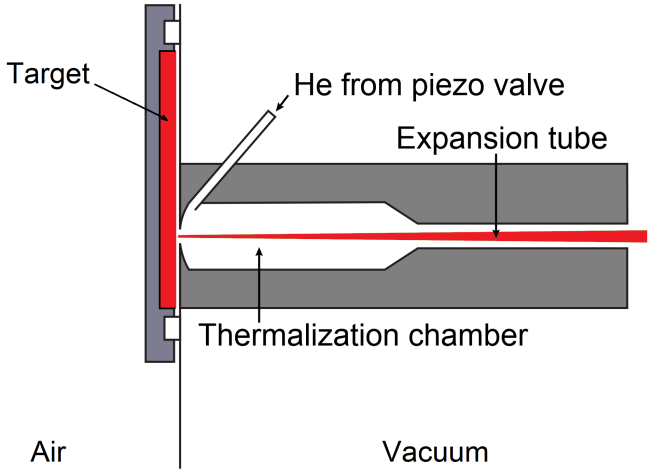

Figure 7.4: Section view of the thermalization chamber. The target is represented on the left.

expansion which is determined by the features of the carrier gas flux. In pulsed laser-ablation sources the gas is operated in a pulsed regime, typically by means of an automated valve triggered by the laser.

Three important parameters are used to define the characteristics of the gas pulse and affect the mass distribution: (i) the pressure of the gas behind the valve, (ii) the time duration of the gas pulse and (iii) the time delay between the laser and the gas pulses. Each of these parameters has to be properly set in order to give rise to an efficient aggregation process. Nonetheless, other important parameters are related to this distribution: (iv) the total amount of produced plasma (controlled by the laser pulse energy), (v) the temperature of the carrier gas, (vi) the shape of the aggregation chamber and of expansion tube [17].

Despite these parameters have fundamental importance in the clusters production and they can be reliably employed to control it, their optimization for a specific mass distribution has to be done through an empirical procedure.

Numerical models for the quantitative description of the aggregation process were introduced over the years, but the conditions of the physical system under consideration, strongly far from equilibrium, are difficult to schematize [18].

One of the first attempts to provide a description for the aggregation process was made by Soler *et al.* [19], who schematized the kinetic of the clusters growth as follows. The kinetic equations for the concentration (per unit volume) of

clusters of size k can be written as

$$\frac{dn_k}{dt} = \sum_{i+j=k} C_{ij} n_i n_j - \sum_i C_{ik} n_i n_k$$

where the first summation gives the rate of creation of clusters with dimension k and the second one is equal to the rate at which clusters of size k are lost by growth to larger clusters. Assuming thermal velocities for all the k-mers, the rate coefficients are

$$C_{ij} = 2\sigma_{ij} \left(\frac{2k_B T}{\pi} \right)^{1/2} \left(\frac{m_i + m_j}{m_i m_j} \right)^{1/2}$$

where σ_{ij} is the cross section and $m_i = im_1$, where m_1 is the mass of the all identical monomers. It worth noting that $C_{1j} \gg Cij$ for $i \gg 1$, meaning that, as expected, in the early stage of the cluster production the growth process is dominated by a single monomer addition. Despite these simple equations give an overview on the aggregation mechanisms, they are not sufficient to perform any numerical simulation. In this framework, in fact, the role of the temperature, as well as the possible temperature-dependence of the aggregation cross sections, was neglected. Moreover, the presence of charged particles and free electrons is not considered.

Other examples of formal descriptions for the aggregation process are present in literature. Their goal is often the numerical modelling of a process taking place in a specific experimental apparatus. Nevertheless, the practical application of the theoretical results is generally not fully satisfying, because of the severe approximations introduced to perform numerical simulation.

For example, the supersonic expansion of a gas mixture composed by rare gas and clusters was described by Christen *et al.* [20]. In their simulation, they separately considered a liquid and a vapour expansion through a nozzle in adiabatic conditions. They managed to calculate the velocities of the particles mixture after the expansion, as a function of its pressure and temperature in the thermalization chamber, considering the condensation phenomenon. Nonetheless, this remarkable result does not describes the kinetics of the condensation process during the expansion, which instead is exactly the point of the NCs aggregation process. More recently, the condensation process of water droplets within a vapour supersonic expansion was successfully modelled for a specific experimental configuration [21].

An important observation about the aggregation process concerns the charge state of the produced clusters. Since the cross section of the electron

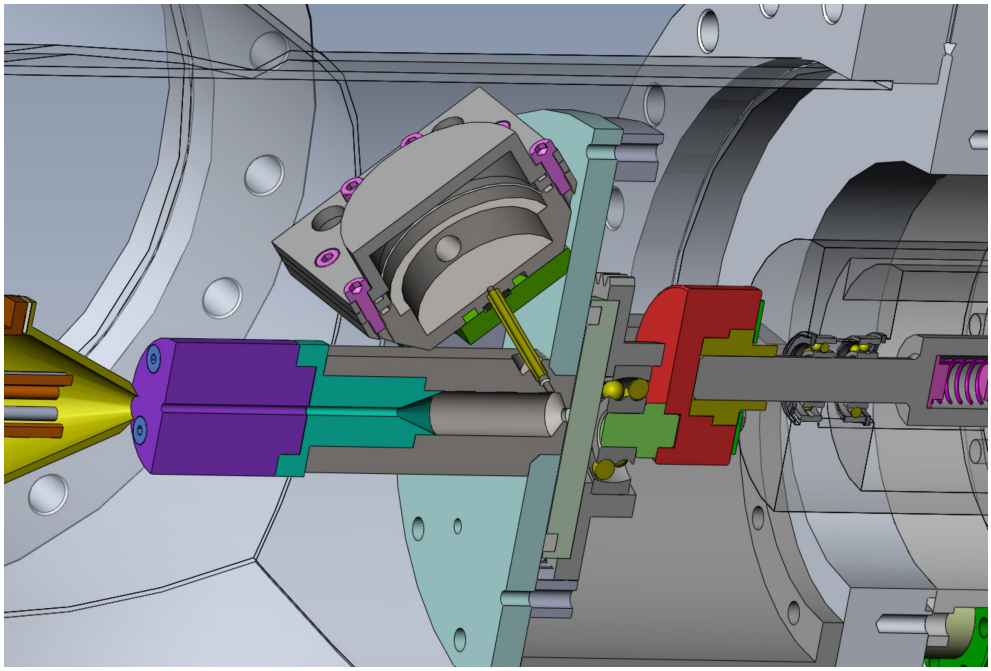

Figure 7.5: Section of the first chamber. The thermalisation chamber is shown at the center of the image, just in front of the rotating target depicted on the right side. Above, the piezoelectric valve housing is represented, connected to the bottom of the aggregation chamber by a channel directed to the ablation zone. On the left hand side of the image, in front of the nozzle (violet) the skimmer is represented (in yellow), covering the first part of the radiofrequency octupole.

capture process in a collision is generally lower than that of the loss, the population of positively charged clusters tends to be larger than the negative. For this reason the SSL cluster source, as other similar sources, is optimized for the transport of positively charged particles.

At the exit of the expansion tube, clusters are transported by the carrier gas within a free supersonic jet, no longer confined in the transverse direction. The supersonic expansion out of the nozzle develops a proper zone of silence in which most of the particles moves in linear trajectories, with a narrow kinetic energy distribution and without colliding with each other. A consistent amount of carrier gas surrounds the silence cone. To get rid of a large part of the gas and collect the clusters, a both aerodynamical and electrostatic optical element is placed in front of the jet. This element, named skimmer, consists of a metallic hollow truncated cone facing the supersonic jet, with an aperture that is fully inside the silence zone. In this configuration it is possible to deliver the produced NCs to a second vacuum chamber equipped with a

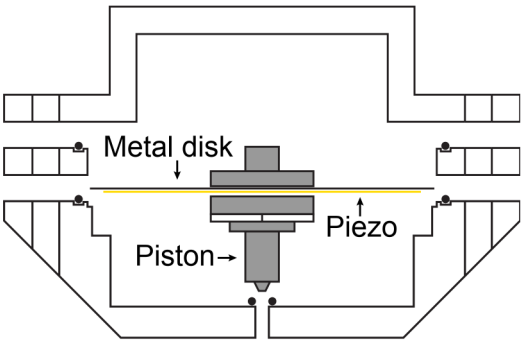

Figure 7.6: Section view of the piezoelectric valve. The square voltage pulse is applied to the piezoelectric disc whose deformation lift the piston letting the gas flowing through the channel below.

dedicated pumping system where the pressure is lower than that of the first chamber even by two orders of magnitude. This kind of differential pumping is a common implementation in the supersonic aggregation cluster sources and it is paramount to the final deposition of clusters in high vacuum conditions.

The structure of the production stage of the SSL source is shown in figure 7.5. The plasma burst generated by the laser pulse is intercepted after a calibrated time delay by a 5-7 bar helium pulse controlled by a piezoelectric valve. The opening of the piezo valve is indeed actuated by a square voltage signal triggered by the laser electronic control system. Dedicated electronic devices are used to set the time delay, the amplitude and the time duration of the opening signal. The helium carries the plasma in the expansion chamber and through the nozzle. The supersonic expansion cone at the nozzle exit is intercepted by the electrostatic skimmer which represents the access to the second chamber. In normal conditions the average pressure in the first chamber is less or equal to 1×10^{-1} mbar, while in the second chamber pressure never exceeds 1×10^{-2} mbar.

Cluster transport. Despite the efficient differential pumping condition established between the first two vacuum stages of a supersonic expansion source, additional pumping stages are generally necessary to achieve high vacuum conditions. An efficient transport system to deliver clusters through the vacuum stages is therefore necessary. Our cluster transport systems is designed to work with charged particles, since mass selection is performed exploiting their mass/charge ratio. In this context, electrostatic lenses and radiofrequency optical elements are used to confine and drive the cluster beam. In our cluster

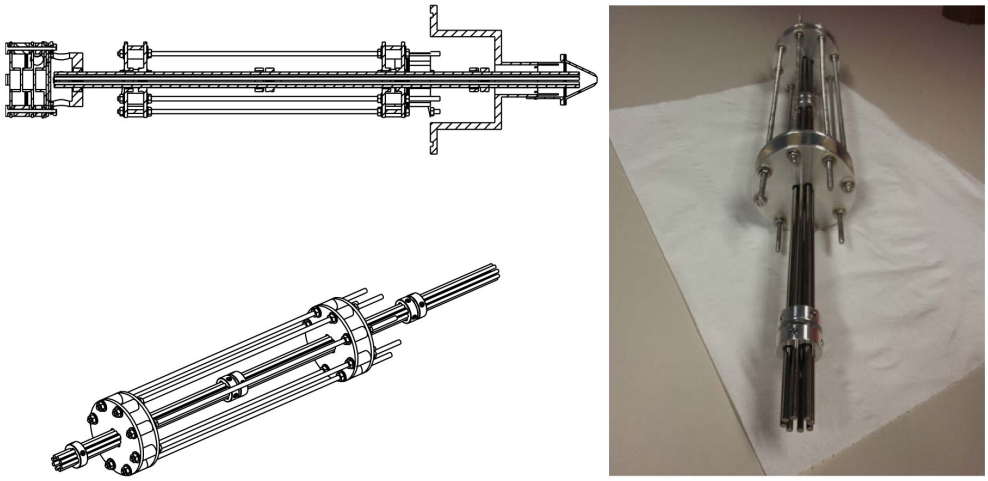

Figure 7.7: The 500 mm transport octupole. The technical drawing in the top left of the image shows its placement right behind the skimmer, and right before a conventional 3-element Einzel lens used for beam refocusing after the octupole.

source both of these solutions are implemented.

In the second chamber of the SSL source a radiofrequency octupole is installed to transport the mass dispersed clusters, with a large acceptance in terms of charge and mass of the particles. The octupole is operated applying a radio-frequency (RF) voltage to alternating bars, so that four bars are always oscillating out-of-phase with the other four. It can be demonstrated that for sufficiently high frequencies, particles inside the octupole experience an effective potential of the form [22]

$$V^* = 4\frac{q^2V_0^2}{m\omega^2 r_0^2}r^6$$

where r_0 is the characteristic radius of the octupole, defined as the radius of the cylinder inscribed in the octupole bars. This centrosymmetric potential is an approximation valid for particles that oscillate within a cylinder of a radius $r_m < 0.8\ r_0$. This condition limits the validity of the effective potential to a maximum transverse energy value. Moreover, to achieve the maximum transport efficiency, the motion of the particles has to be separable into a fast RF driven motion and a secular motion, so to satisfy the adiabaticity condition that ensures the stability of the particles trajectories. It is possible to define, for an octupole, an adiabaticity parameter

$$\eta = 24\frac{qV_0}{m\omega^2 r_0^2}r_m^2 \quad .$$

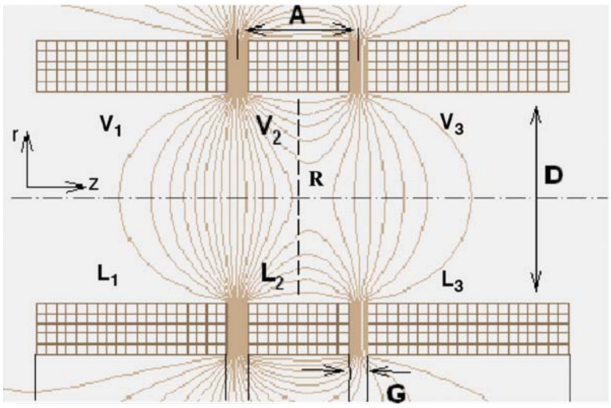

Figure 7.8: Numerical simulation performed by SIMION software of an asymmetric Einzel lens where the potential relative values are defined as V_1=1, V_2=6 and V_3=3 [24].

It can be demonstrated that the stability of the trajectories can be achieved for $\eta < 0.3$. This condition defines a relation between the mass of the particles, the geometry of the octupole and the RF frequency.

The octupole installed in our machine consists of 500 mm length 3 mm diameter bars, with $r_0 = 11$ mm, and is driven by a 2 MHz RF signal, oscillating around an independently controlled DC bias. These specifics allow the transport of NCs with masses from 10 to 16000 a.m.u.

After the octupole, clusters are collected by an Einzel lens that focuses them through the aperture of a third differential pumping stage. Einzel lenses are widely used electrostatic optics, composed of three cylindrical elements disposed in series, coaxially with the transport direction [23]. In the original design, the first and the last elements are set to the same potential, while the ratio between this one and the potential of the central element defines the focal length of the optics. A more complex configuration can be obtained using three different potentials for the three elements; in this way is possible to obtain an asymmetric system with two focal points and a higher degree of manipulation on the particle beam size and divergence. A modified version of the Einzel lens can be produced adding an even number of elements to the initial three. In our system 7-element lenses are installed before and after the electrostatic bender.

Charge selection. In the case of our cluster source the mass selection is done on the basis of the charge/mass ratio of single polarized NCs. For this reason, is necessary to discriminate the clusters by charge sign. One of the most efficient devices for this application is the electrostatic quadrupole bender [25].

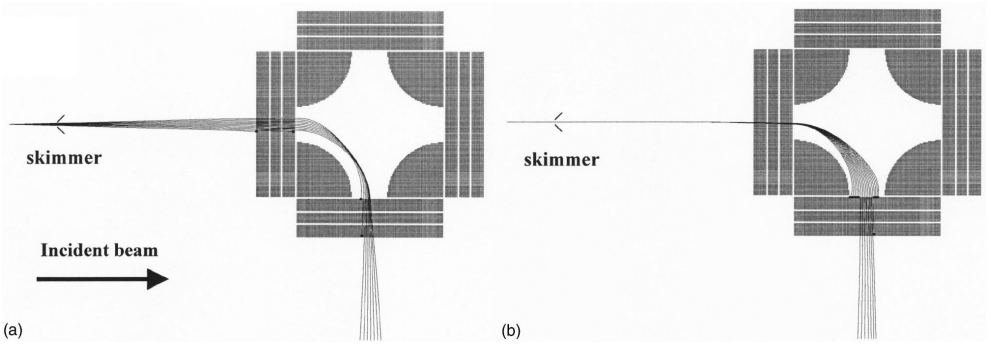

Figure 7.9: Simulated trajectories (in scale) of charged clusters in the deviation plane (x − y). The incoming cluster beam comes from the left (x axis). The trajectories start from the center of the nozzle orifice. a) The incoming clusters have kinetic energy fixed at $E_k = eU = 140\,eV$. Several incidences about the geometric x axis have been considered. b) The incoming clusters are assumed to form a sharp parallel beam. Their kinetic energy E_k varies from 100 eV up to 180 eV by 5 eV steps. Image reproduced from [26].

This system can be described as a quadrupole whose axis is oriented perpendicularly to the particles direction (see figure 7.9). Opposite bars are set to a common potential, generating symmetrical constant potential surfaces across which clusters are driven. The difference between the two potentials determines the gradient of the electric field, that has to be tuned on the basis of the kinetic energy of the particles. The average value of the two potentials has to be set in accordance with the potential of the optical elements placed before and after the bender, to avoid discontinuities in the electrostatic field along the particles path.

As a result, neutral particles passing through the bender will not be affected by the presence of the electric field, and they will continue along their initial direction. Charged particles instead, with the correct voltage values, can be deviated by 90° in opposite directions. As illustrated in the numerical simulation reported in figure 7.9, angle and energy dispersion of the particle entering the bender determine a dispersion of the trajectories. Divergent monochromatic beams are focalized within the quadrupole, while collimated but energetically dispersed beams are spread in angle. In our apparatus, the initial angular divergence of the beam is minimized by an Einzel lens, while the energy dispersion is directly related to the supersonic expansion and is generally narrow enough to allow an efficient transmission. An angular dispersion is also produced as a consequence of the mass dispersion of the particles. Nevertheless, with a suffi-

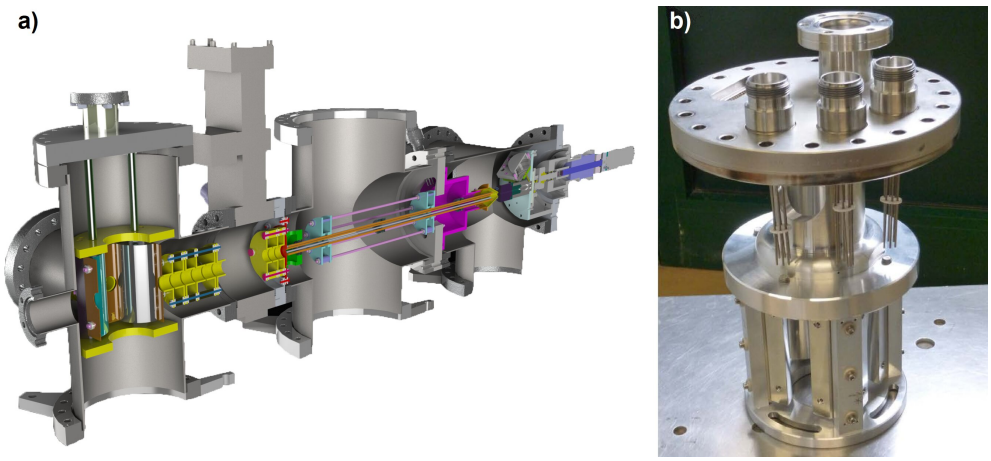

Figure 7.10: a) Section of the first three differential pumping stages of the SSL clustersource b) picture of the bender installed in the third vacuum stage.

ciently high gradient of the electric field is possible to confine the clusters path, reducing their angular dispersion, and to recollect ideally the whole cluster population after the bender by means of an additional Einzel lens.

Mass selection. The size selection stage stands as the final part of the production process. During the years several techniques were applied to characterize the NCs mass distribution and to filter clusters in order to deposit significant amounts of identical clusters on a solid surface. In most cases the mass selection method is based on the electric charge of the clusters. Neutral NCs are indeed particularly difficult to discriminate in mass, and few attempts were made exploiting the mass-dependent velocity distribution of the particles in the supersonic expansion [27]. Anyway, the resolution and mass range achievable with this method proved to be significantly lower than the ones provided by the charged particles selection methods. A review of the most common families

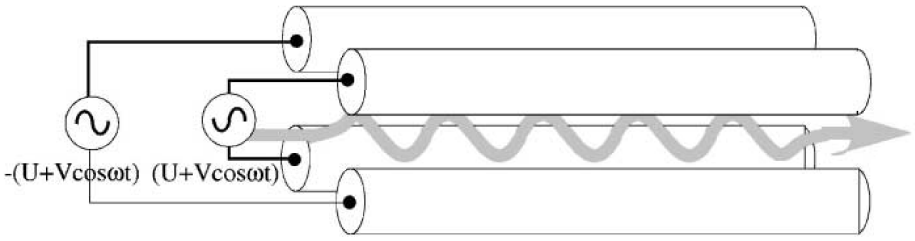

Figure 7.11: Connection diagram of a cylindrical quadrupole mass filter.

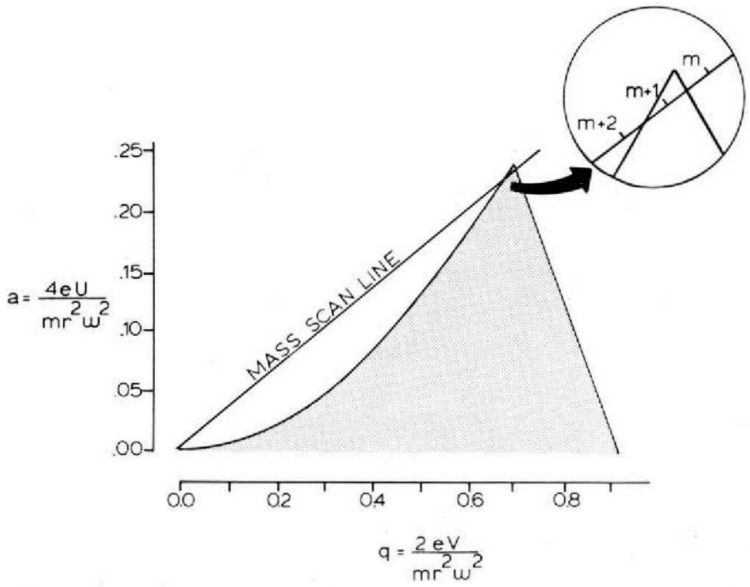

Figure 7.12: The a–q stability diagram [28]. The shaded area represents the a–q conditions that correspond to the stable solutions of the Mathieu's differential equation. Considering the mass of the particle as the parameter of the mass scan line (whose equation is $a = 2\frac{U}{V}q$), we can observe that only some values for m admit a stable solution.

of mass selection setups was given by Binns [9]. The one we are going to discuss for the sake of our machine description is the radiofrequency quadrupole or Quadrupole Mass Spectrometer (QMS). This instrument, constituted by four cylindrical poles, as depicted in figure 7.11, can act as an efficient filter that requires the control of a limited number of parameters and provides high mass resolution in a wide mass range, with the possibility to easily balance between NCs flux and mass resolution.

An ideal quadrupole is formed by four hyperbolic electrodes. The machining of hyperbolic surfaces is particularly complex, so quadrupoles are usually built on the basis of four cylindrical rods with a radius $r = 1.148r_0$ where r_0 is the radius of the cylinder inscribed in the four bars. With this design it is possible to apply the electric field equation for the ideal geometry with a good approximation.

Opposite bars of the QMS are connected to the same oscillating voltage signal. The potential distribution Φ generated inside an hyperbolic QMS has the form

$$\Phi = [U + V\cos(\omega t)]\frac{x^2 - y^2}{2r_0^2}$$

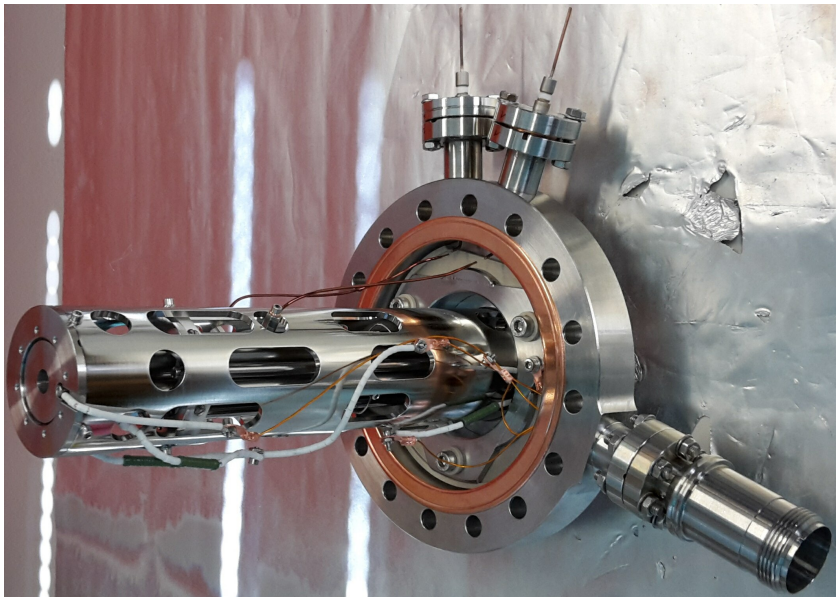

Figure 7.13: The quadrupole mass spectrometer mounted on a custom made support flange. The bars are mounted inside an outer conductive shield to screen the external electromagnetic noise and envelop the quadrupole in a controllable electrostatic field.

where x and y are the transverse space coordinates respect to the QMS axis, U is the magnitude of the applied DC voltage, V and ω are the intensity and the angular frequency of the applied RF signal, respectively. Defining the parameters a and q as

$$a = \frac{4eU}{\omega^2 r_0^2 m} \qquad \text{and} \qquad q = \frac{2eV}{\omega^2 r_0^2 m}$$

it is possible to write the equation of motion of a particle of mass m in the form of the Mathieu's equation

$$\frac{d^2u}{d\xi^2} + [a_u + 2q_u \cos(2\xi)]u = 0$$

where $\xi = t/2$ and u represents x or y. It can be demonstrated that the solution of this kind of differential equation may be classified as bounded and unbounded with the physical meaning that in the first case the coordinates x and y of the particle do not diverge. This condition, for a quadrupole mass filter corresponds to the so called stability condition. It is possible to plot in a a-q diagram the region of stability (see figure 7.12). If we consider a fixed value for the $\frac{U}{V}$ ratio, we can use m as a parameter for the line defined by the equation $a = 2\frac{U}{V}q$. The values of the masses that lie within the stability regions are the masses of the particles that are transmitted by the QMS. Heavier particles, whose masses

values are closer to the origin of the diagram, undergo to a defocusing effect due to the high intensity of the DC component of the field, while lighter particles are subjected to oscillation that causes them to collide on the quadrupole bars, due to the high RF intensity. An effective method to scan the mass values operating the QMS as a mass selector is to change the values of U and V simultaneously, maintaining the ratio fixed. In this manner, on the diagram, the slope of the mass scan line remains unchanged, while the parametrization of the line gets modified, changing the mass values within the stability region. In this operational mode the quadrupole acts as a bandpass filter, but it is possible to operate in a high pass mode by decreasing the $\frac{U}{V}$ ratio so to bring the mass scan line inside the stability region for all the masses above a certain value. Moreover, the possibility to operate the QMS setting to zero the DC potential can be exploited to totally transmit unselected nanoclusters.

Cluster deposition. After the quadrupole mass filter, the SSL source is equipped with a conventional Einzel lens whose duty is to collect the particles transmitted by the QMS, decelerating and defocusing the beam, in order to deposit them on the desired substrate as homogeneously as possible and with a low kinetic energy. The homogeneity of the clusters spacial distribution on the substrate surface is useful for the analysis of a sample. The low kinetic energy requirement is instead a fundamental requirement for the study of the NCs itselves. The energy of the impact can indeed cause the breaking of the clusters. It has been calculated and experimentally measured that these energies can vary from few eV to few tens of meV [29–31], while the energy of the clusters passing through the QMS is usually between 10 and 100 eV.

Being the clusters electrically charged, it is finally possible to directly count them by measuring the electric current on the deposition sample. On our cluster source this method is implemented by means of a picoammeter. We wrote a customized software in order to continuously read the current value and control the QMS, to allow the acquisition of the mass spectra of the clusters produced. By controlling the electrostatic potential applied to the sample, it is also possible to investigate the kinetic energy distribution of the upcoming clusters.

7.2 Functional tests and first results

At the beginning of my PhD, the first three vacuum stages of the SSL cluster source were operating together with the laser system. Therefore, the first tests

we performed involved mass dispersed nanoclusters. The first operations on the newly installed cluster source were related to the ablation process. Laser power test and alignment were firstly executed, being basic requirements for the machine working. Laser alignment was performed by acting on an adjustable dielectric mirror installed in the laser head and on the mirror placed in front of the viewport. Fringes around the circular light spot were removed by pinholes placed along the beam path to minimize reflections inside the vacuum chambers. The fine adjustment of the optical elements, including the focusing lens, were executed verifying the absence of reflections on the nozzle.

The piezoelectric valve was calibrated before shining the laser beam on the target. Laser pulses indeed produce an amount of vapour and plasma that can remain inside the thermalization chamber and on the ablation target, if a sufficient amount of carrier gas is not provided. The flux of helium delivered through the piezo-valve can be indirectly quantified by measuring the pressure in the first vacuum chamber, which in normal operation conditions is of the order of 10^{-1} mbar.

A pure metal target was installed to perform the first operational tests on the machine. Nickel has been chosen to this purpose due to the possibility to produce NCs in a broad mass range [32], which makes easier the research for the correct production parameters. The procedure was carried out step by step, starting from the tuning of the generation parameters: laser power, He pressure, He pulse duration and laser–He pulse delay.

The effective production of Ni ions and charged clusters was initially assessed. To this goal, the skimmer was connected to a picoammeter and biased with a negative voltage of -10 eV to collect positively charged particles. The parameters were modified in order to maximise the current measured on the skimmer. This operation had to be performed in a short time (a few minutes) to minimize the amount of metal deposited on the electrostatic element. A current of the order of few hundreds nA was measured before moving to the cluster transport optimization.

The regulation of the transport system was executed for all the optical elements mounted in the first three stages, up to the electrostatic lenses placed after the bender. A sketch of the electrostatic and RF components is reported in figure 7.14. Since the RF octupole frequency and voltage had been previously calculated for the specific setup, little work was necessary to verify the functioning of this element. To this goal we applied a strategy similar to that used to assess the cluster production: we measured the cluster current at the exit of the octupole by connecting the picoammeter to the electrostatic lens at its end

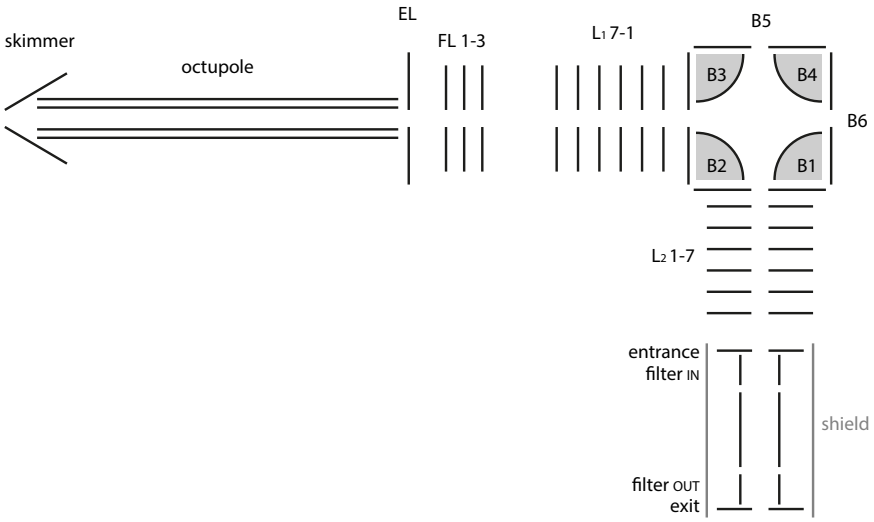

Figure 7.14: Schematic representation of the cluster transport system of the SSL cluster source.

(EL in figure). For this measurement, EL was kept at ground potential while a high positive voltage was applied on the following electrostatic element to repulse positive particles and recollect them on EL. The octupole DC voltage was tuned in order to achieve the highest current. This lenses configuration allowed also to estimate the kinetic energy of the particles, that results to be of the order of the electrostatic potential applied to repulse the particles, multiplied by the elementary charge. We measured a kinetic energy value of about 10 eV. This optimization procedure was applied for the subsequent electrostatic elements including the bender. The charge selected cluster current was finally measured after the L_2 lensing group. A current of about 10 nA was measured on a 20 mm diameter sample connected to ground and placed at 10 mm from the last electrostatic element. The difference between the current measured on the skimmer and on the sample was mainly due to cluster losses along the transport system. Further optimization were carried out until a current of few tens of nA was measured. It can be easily calculated that with this current value it is possible to deposit 0.1 ML of unselected NCs on a 1 cm^2 surface in a few minutes.

The cluster source was subsequently implemented with the installation of the QMS in the fourth differential pumping stage. A silver target was mounted to characterize the last part of the apparatus and optimize the machine for the first experiments. Production and transport parameters were modified to

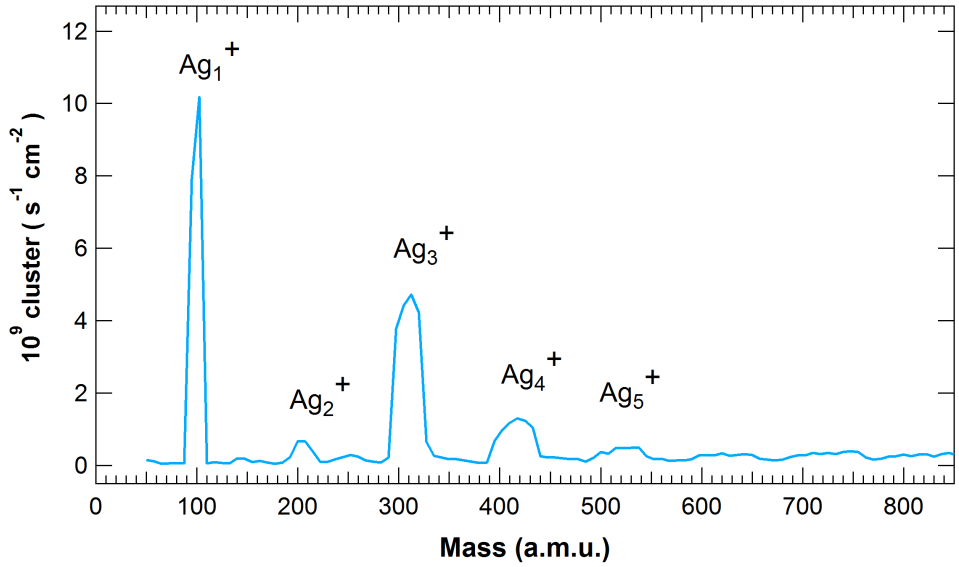

Figure 7.15: Mass spectrum of positively charged Ag clusters (He pressure = 5 bar, He pulse duration = 480 μs, He–laser pulse delay 6.6 ms, pressure in the first vacuum chamber = 1.0 mbar, laser power = 10 W).

maximize the unselected Ag cluster production. Different elements requires in fact slightly different settings, whose determination is empirical.

Unselected nanoclusters were delivered to the sample through the QMS operating in high pass mode, in order to yield particles with masses equal to and higher than the mass of Ag atoms. The unselected cluster current resulted to be about 2 nA, lower than that of Ni, but still suitable for the execution of experiments.

After this accomplishment, mass spectra of the produced Ag cluster were acquired by switching the QMS to band pass mode. In figure 7.15 an example is reported. The mass spectrum was acquired performing a mass scan between 50 and 850 a.m.u. The cluster production is maximum for Ag monomers and decreases for larger masses. Modulation of the cluster current is detected up to mass values equivalent to Ag_7^+. Interestingly, the intensity of Ag_2^+ is less than Ag_1^+ and Ag_3^+ and it could be explained considering the formation energy of Ag clusters, which results to be higher for clusters with an odd number of electrons [33, 34]. The FWHM of the peaks increases for larger masses for two main reasons. The first is an intrinsic effect due to the natural occurrence of Ag isotopes, whose possible combination increases with the number of atoms per cluster. The second reason for the broadening is that the mass scan was

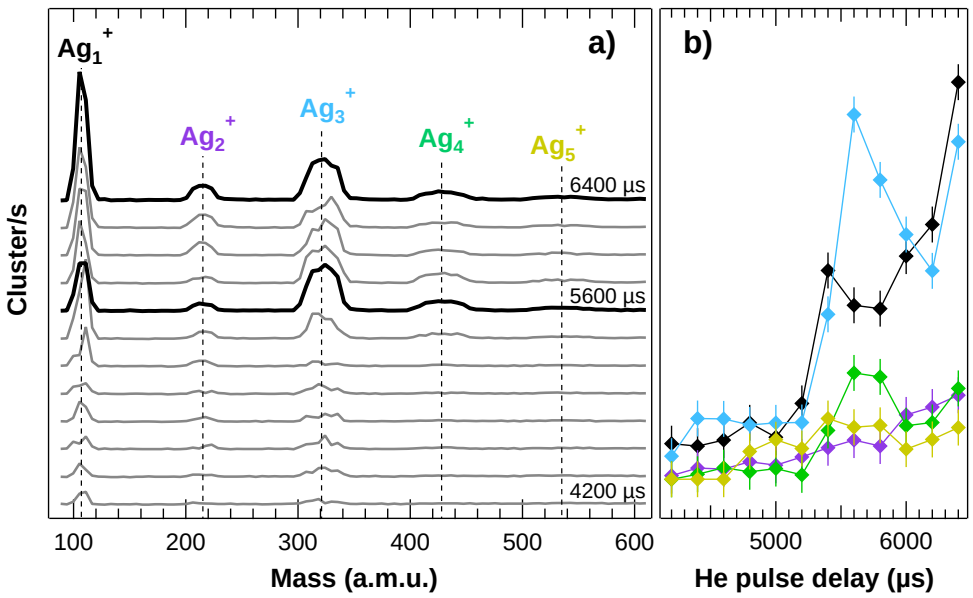

Figure 7.16: Ag cluster mass spectra acquired at different values of the time delay between laser and He pulse, for positively charged particles (He pressure = 5 bar, He pulse duration = 480 μs, pressure in the first vacuum chamber = 1.0 mbar, laser power = 10 W).

performed at fixed resolution, i.e. fixing the ratio $\Delta m/m$ through the voltages applied to the QMS. This operational mode was selected because it provides an enhancement of the signal for high mass values.

With the aim of exploring the dependence of the NCs mass spectrum on the aggregation parameters, we acquired series of spectra as a function of them. One of the series of spectra we acquired during these tests is reported in figure 7.16a. Spectra were acquired in the low mass range from 80 to 600 a.m.u. as a function of the He–laser pulse delay. We observed that for time delay smaller than 5 ms the cluster production is strongly hindered. A general increase in the cluster current is observed up to 6.4 ms, followed by a sudden drop (not reported in figure) around 6.5 ms. It is known that the timing in the helium pulse is one of the most important variables in the cluster generation. Our aim was to understand the effect of this parameter on the cluster size distribution. To this end we fitted each mass peak with a Gaussian distribution for each spectrum and we observed the evolution of their intensity as a function of the delay. A single Gaussian was used for each mass peak irrespective of the isotopic combination, due to the low mass resolution. The intensity values of each spectral component are shown in figure 7.16b. Within the general signal

enhancing for higher delay values, we detected a maximum in the production of Ag_3^+ and Ag_4^+ for a delay of 5.6 ms. This is an evidence of the effectiveness of this parameter in the determination of the mass spectral distribution.

Similar tests were carried on for He pressure and other will be performed considering the laser power and the time duration of the He pulse. Along with the generation parameters, the transport ones will be optimized on the basis of the mass range under investigation. At the end of these series of tests we expect to achieve a comprehensive characterization of the cluster source functioning for positive Ag cluster production, that will provide the possibility to perform the first experimental measurements on mono-dispersed nanoclusters.

7.3 Perspectives

The final goal concerning the SSL cluster source is its interfacing with the SuperESCA beamline. After a period of clusters production optimization at SSL, in particular for Ag in the high mass range, the last vacuum chamber of the source will be upgraded with the elements needed for its connection with the SuperESCA end station. A second radio-frequency octupole (which we designed and assembled) will be installed in order to deposit selected nanoclusters directly on the sample mounted on the SuperESCA manipulator. Modification of the laser setup will be implemented for logistic reasons and functional tests will be performed before moving the source from the SSL laboratory to the Elettra's experimental hall.

This complex experimental facility, that will be open to users, will allow in-situ characterization of mass selected NCs by synchrotron radiation-based techniques. The direct soft-landing of clusters on a substrate in UHV and at low temperature will ensure the high quality of the samples to investigate.

Among the experiments that could be performed using this experimental apparatus, one of the most interesting in the context of this thesis would be the characterization of nanoarchitectures containing mono-dispersed clusters. Nano-designed interfaces similar to those discussed in the previous chapter could be grown depositing identical NCs, smaller, in average, than the NPs discussed in the previous chapters. Synchrotron radiation techniques could be used to investigate, for example, the electronic structure of size-controlled metal particles and their oxidation mechanisms. Concerning our titania nanoarchitectures, significant results could be obtained from the size control on the TiO_2 NCs that could be prepared by oxidation of size selected Ti NCs deposited on a solid surface. Alternatively, TiO_2 NCs could be directly grown by

aggregation of Ti and O atoms using a gas mixture made of O_2 seeded in He. It would be also possible to oxidize Ti clusters immediately after their creation by implementing on the SSL source a technical upgrade recently designed by Masubuchi *et al.* [35].

It has been demonstrated that titania clusters with different size and shapes can show different electronic structures, band gap values and defect states [36]. Core and valence electronic levels could be investigated by synchrotron radiation techniques as a function of the precise mass of the NCs. In addition, detailed structural information about such systems could be retrieved by means of XAS and X-ray Photoelectron Diffraction measurements. In this way it would be possible, in principle, to make a direct comparison between experimental results and DFT calculations performed on the basis of the experimental observation. Moreover, the use of a solid support for nanoclusters would stabilize them, reducing the sintering phenomena that generally affect this kind of assembly. At a later stage, the charge transfer between graphene and supported clusters could be accurately investigated as a function of the clusters dimension. Also in this case, thanks to the high degree of control in the growth of the nanostructures, the comparison with the numerical simulation would be particularly meaningful.

References

[1] Grandjean, D.; Coutiño-Gonzalez, E.; Cuong, N. T.; Fron, E.; Baekelant, W.; Aghakhani, S.; Schlexer, P.; D'Acapito, F.; Banerjee, D.; Roeffaers, j. v. n. p. y. p., Maarten BJ Origin of the bright photoluminescence of few-atom silver clusters confined in LTA zeolites.

[2] Alonso, J. A. *Structure and properties of atomic nanoclusters*; World Scientific, 2012.

[3] Misra, P. *Physics of condensed matter*; Academic Press, 2011.

[4] Liu, L.; Corma, A. Metal catalysts for heterogeneous catalysis: From single atoms to nanoclusters and nanoparticles. *Chemical Reviews* **118**, 4981 (2018).

[5] Nishioka, H.; Hansen, K.; Mottelson, B. Supershells in metal clusters. *Physical Review B* **42**, 9377 (1990).

[6] Inoshita, T.; Ohnishi, S.; Oshiyama, A. Electronic structure of the superatom: a quasiatomic system based on a semiconductor heterostructure. *Physical Review Letters* **57**, 2560 (1986).

[7] Kroto, H. W.; Heath, J. R.; O'Brien, S. C.; Curl, R. F.; Smalley, R. E. C_{60}: Buckminsterfullerene. *Nature* **318**, 162 (1985).

[8] Heiz, U.; Vanolli, F.; Trento, L.; Schneider, W.-D. Chemical reactivity of size-selected supported clusters: An experimental setup. *Review of Scientific Instruments* **68**, 1986 (1997).

[9] Binns, C. Nanoclusters deposited on surfaces. *Surface Science Reports* **44**, 1 (2001).

[10] Hall, S.; Nielsen, M.; Robinson, A.; Palmer, R. Compact sputter source for deposition of small size-selected clusters. *Review of Scientific Instruments* **68**, 3335 (1997).

[11] Pratontep, S.; Carroll, S.; Xirouchaki, C.; Streun, M.; Palmer, R. Size-selected cluster beam source based on radio frequency magnetron plasma sputtering and gas condensation. *Review of Scientific Instruments* **76**, 045103 (2005).

[12] Duncan, M. A. Invited review article: Laser vaporization cluster sources. *Review of Scientific Instruments* **83**, 041101 (2012).

[13] Dietz, T. G.; Duncan, M. A.; Powers, D. E.; Smalley, R. E. Laser production of supersonic metal cluster beams. *The Journal of Chemical Physics* **74**, 6511 (1981).

[14] Leitz, K.-H.; Redlingshöfer, B.; Reg, Y.; Otto, A.; Schmidt, M. Metal ablation with short and ultrashort laser pulses. *Physics Procedia* **12**, 230 (2011).

[15] Chichkov, B. N.; Momma, C.; Nolte, S.; Von Alvensleben, F.; Tünnermann, A. Femtosecond, picosecond and nanosecond laser ablation of solids. *Applied Physics A* **63**, 109 (1996).

[16] Stein, G. D. Cluster beam sources: Predictions and limitations of the nucleation theory. *Surface Science* **156**, 44 (1985).

[17] Milani, P.; deHeer, W. A. Improved pulsed laser vaporization source for production of intense beams of neutral and ionized clusters. *Review of Scientific Instruments* **61**, 1835 (1990).

[18] Scoles, G. *Atomic and molecular beam methods*; Oxford university press, 1988.

[19] Soler, J.; Garcia, N.; Echt, O.; Sattler, K.; Recknagel, E. Microcluster growth: transition from successive monomer addition to coagulation. *Physical Review Letters* **49**, 1857 (1982).

[20] Christen, W.; Rademann, K.; Even, U. Supersonic beams at high particle densities: Model description beyond the ideal gas approximation. *The Journal of Physical Chemistry A* **114**, 11189 (2010).

[21] Klíma, M.; Kolafa, J. Direct Molecular Dynamics Simulation of Nucleation during Supersonic Expansion of Gas to a Vacuum. *Journal of chemical theory and computation* **14**, 2332 (2018).

[22] Gerlich, D. Inhomogeneous, RF fields: a versatile tool for the study of processes with slow ions. *Advances in Chemical Physics* **82**, 1 (1992).

[23] Adams, A.; Read, F. Electrostatic cylinder lenses II: Three element einzel lenses. *Journal of Physics E: Scientific Instruments* **5**, 150 (1972).

[24] Sise, O.; Ulu, M.; Dogan, M. Multi-element cylindrical electrostatic lens systems for focusing and controlling charged particles. *Nuclear Instruments and Methods in Physics Research Section A: Accelerators, Spectrometers, Detectors and Associated Equipment* **554**, 114 (2005).

[25] Mahaffy, P.; Lai, K. An electrostatic quadrupole deflector for mass spectrometer applications. *Journal of Vacuum Science & Technology A: Vacuum, Surfaces, and Films* **8**, 3244 (1990).

[26] Alayan, R.; Arnaud, L.; Bourgey, A.; Broyer, M.; Cottancin, E.; Huntzinger, J.; Lermé, J.; Vialle, J.; Pellarin, M.; Guiraud, G. Application of a static quadrupole deviator to the deposition of size-selected cluster ions from a laser vaporization source. *Review of Scientific Instruments* **75**, 2461 (2004).

[27] Broyer, M.; Cabaud, B.; Hoareau, A.; Melinon, P.; Rayane, D.; Tribollet, B. Velocity slip measurements of bismuth clusters produced by the inert gas condensation technique. *Molecular Physics* **62**, 559 (1987).

[28] Miller, P. E.; Denton, M. B. The quadrupole mass filter: basic operating concepts. *Journal of Chemical Education* **63**, 617 (1986).

[29] Cheng, H.-P.; Landman, U. Controlled deposition, soft landing, and glass formation in nanocluster-surface collisions. *Science* **260**, 1304 (1993).

[30] Fedrigo, S.; Harbich, W.; Buttet, J. Soft landing and fragmentation of small clusters deposited in noble-gas films. *Physical Review B* **58**, 7428 (1998).

[31] Popok, V. N.; Barke, I.; Campbell, E. E.; Meiwes-Broer, K.-H. Cluster-surface interaction: From soft landing to implantation. *Surface Science Reports* **66**, 347 (2011).

[32] Heiz, U. Size-selected, supported clusters: the interaction of carbon monoxide with nickel clusters. *Applied Physics A* **67**, 621 (1998).

[33] Zhao, J.; Luo, Y.; Wang, G. Tight-binding study of structural and electronic properties of silver clusters. *The European Physical Journal D-Atomic, Molecular, Optical and Plasma Physics* **14**, 309 (2001).

[34] Gamboa, G. U.; Reber, A. C.; Khanna, S. N. Electronic subshell splitting controls the atomic structure of charged and neutral silver clusters. *New Journal of Chemistry* **37**, 3928 (2013).

[35] Masubuchi, T.; Eckhard, J. F.; Lange, K.; Visser, B.; Tschurl, M.; Heiz, U. An efficient laser vaporization source for chemically modified metal clusters characterized by thermodynamics and kinetics. *Review of Scientific Instruments* **89**, 023104 (2018).

[36] De Angelis, F.; Di Valentin, C.; Fantacci, S.; Vittadini, A.; Selloni, A. Theoretical studies on anatase and less common TiO_2 phases: bulk, surfaces, and nanomaterials. *Chemical Reviews* **114**, 9708 (2014).

Chapter 8

Conclusions

The experimental results discussed in this thesis provide evidence of the effectiveness of graphene as primary building block for customizable interfaces.

The iterated preparation of nanostructures having similar design but different chemical constituents has proven to be a good strategy in the exploration of NPs–Gr interaction. We observed that the growth and characterization of the nanostructures by applying the same experimental techniques can represent a good strategy to highlight peculiar aspects, particularly concerning the electronic and chemical properties of the systems under investigation.

In this respect, the electric charge transfer and redistribution between graphene and NPs had a central role in our experimental work. Photoelectron spectroscopy measurements remarked substantial differences among the three transition metals we considered, witnessing the subtle complexity of this phenomenon. In particular we observed a strong interaction between Ti and Ti-oxide NPs with graphene, with and without the oxide interfacial layer. In particular, a negative charge transfer from TiO_2 to Gr was observed in both cases. Fe and Fe-oxide NPs instead proved to be almost non-interacting with Gr/Ir (111) but weakly with Gr when Fe-oxide was intercalated. Finally Co showed a further different behaviour. Metallic Co was found to weakly interact with graphene unless the intercalated oxide layer was present. Cobalt oxide NPs demonstrated instead to interact with graphene both with and without the interfacial oxide. The mechanisms that drive these variation in the NPs/Gr interaction are still to be understood in details. Anyway, in all cases the intercalated oxide layer was found to induce an electron charge transfer from graphene to the oxide itself.

Among the most significant results we achieved I want to underline the en-

hancement of the photocatalytic activity of TiO_2 NPs obtained by supporting them on epitaxial graphene and the further activity increase obtained by doping graphene using oxide intercalation. Moreover, by a broad multi-technique characterization of the TiO_2 architectures, we identified a relation between the electronic structure of TiO_2 and the photocatalytic activity of the NPs. We demonstrated, in this way, that the doping condition of graphene can actually affect the chemical properties of the supported nanoparticles. Theoretical calculations performed on the titania architectures pointed out the effective modification of the electronic structure of the Gr-supported TiO_2 due to the presence of the intercalated oxide and provided a possible explanation for the measured enhancement in the photocatalytic activity of this material.

Interesting results could arise from the future measurements of the photocatalytic activity of the Fe-based structures, while the preliminary results on the Co-based structures were instead not positive. In this context, both the composition and the morphology of nanoparticles are essential, but a fine control on these parameters cannot be achieved easily by standard CVD procedures. This growth method demonstrated in fact its limitation, for example, in the growth of Co NPs in which the interaction between Co atoms and the substrate determined the particular flat shape of the islands. In this regard, the size selected nanocluster source could be efficiently used to overcome these CVD issues and it would provide a series of outstanding advantages in the fabrication of nanoassembly. In the last part of the thesis the proof of the machine functioning was shown through the discussion of the first mass distribution curves measured in the Surface Science Laboratory. We believe that in a short time our cluster source will be optimized for the production of relatively large clusters and could be employed to recreate new versions of the graphene architectures described here, using identical particles of virtually any element of the periodic table, with the final aim of improving our understanding of atomic processes at the nanoscale which are at the basis of the macroscopic behaviour of the materials.